A Model of the Temporal and Spatial Distribution of Carbon Monoxide in the Mixed Layer

by

Anthony James Kettle

B.Sc. Physics and Chemistry, Memorial University of Newfoundland, 1991

Submitted to the Massachusetts Institute of Technology/ Woods Hole Oceanographic Institution Joint Program in Oceanography in Partial Fulfillment of the Requirements of the Degree of

MASTER OF SCIENCE

at the

MASSACHUSETTS INSTITUTE OF TECHNOLOGY

and the

WOODS HOLE OCEANOGRAPHIC INSTITUTION

June 1994

Author .....
Joint Program in Oceanography
Massachusetts Institute of Technology/Woods Hole Oceanographic Institution

Certified by .....
James F. Price
Thesis Supervisor

Accepted by .....
Lawrence J. Pratt
Chair, Joint Committee on Physical Oceanography

A Model of the Temporal and Spatial Distribution of Carbon Monoxide in the Mixed Layer

by
Anthony James Kettle

Submitted to the Massachusetts Institute of Technology/Woods Hole Oceanographic Institution Joint Program in Oceanography in Partial Fulfillment of the Requirements of the Degree of
Master of Science in Oceanography

A field experiment demonstrated the presence of a diurnal cycle in the concentration of carbon monoxide ([CO]) in the upper ocean at the BATS site. A series of laboratory experiments and numerical simulations were carried out to assess the diurnal variation in [CO] both at the sea surface and in the upper layers of the water column down to 200 m. Published studies of this cycle have suggested that the dominant controlling processes are light-induced production, microbial CO consumption, surface degassing, and dilution due to entrainment of deeper CO-depleted water into the mixed layer. Laboratory experiments focussed on finding the production rate coefficient and the destruction rate. The numerical studies were conducted to simulate the diurnal cycle in [CO] at the sea surface and at depth, and the results confirmed the values of the production rate coefficient and destruction rate obtained by the laboratory experiments. The field measurements indicate that [CO] does not vanish below the euphotic zone as expected. This may be due to a possible blank correction to the measurements, low destruction rate at depth, or a small dark production rate. The CO consumption e-folding was optimized by numeric experiment and calculated to be about 52 ± 9 h on the basis of a minimized sea surface [CO] deviation and 73 ± 10 h on the basis of minimized CO inventory deviation. Laboratory determinations of apparent quantum yield and numeric experiment lead to an optimized sea surface production of CO $0.40 \pm 0.05 \mathrm{nMh}^{-1}$. Finally, deviations between the [CO] measurements and numeric experiments suggest that factors controlling the CO budget may be subject to spatial and temporal patchiness.

Acknowledgements

I appreciate the scientific assistance given to me in this project by William Martin, Jim Price, and Oliver Zafiriou. Mary Scranton provided the CO analyzer which facilitated the series of experiments to determine the apparent quantum yield of seawater. William Martin and Steve Andrews carried out the bulk of the scientific program at the BATS site on March 14-24, 1993. Meteorological data was provided by the United States Naval Air Station at Bermuda and by Susan Tarbell for the Altimoor buoy at the BATS site. I also appreciate the financial support made available by agencies which funded this project. In this regard, personal support came from NASA grant NAGW-2431 and ONR grant N00014-89-J-1258. The ship time and BATS CO investigation was funded through NSF grant NSF OCE 9115608.

Contents

List of Figures

List of Tables

Chapter 1

Introduction

Carbon monoxide (CO) has been observed to undergo a diurnal cycle in concentration in the surface layer of the ocean with a peak in surface concentration up to six hours past local solar noon and minimum near dawn (Conrad et al (1982), Conrad and Seiler (1986)). The variation in the concentration of CO (denoted by [CO]) during the daily solar heating cycle results from the interplay between various production and destruction mechanisms present in the upper ocean. The production is suspected to be primarily due to a photochemical reaction initiated by solar energy. Destruction is thought to be due mainly to consumption by bacteria, although there is degassing through the ocean surface and [CO] decreases due to dilution within the mixed layer as well. The goal of this investigation is first to understand the individual destruction and production processes measured during a cruise to the Sargasso Sea on March 15–24, 1993 and then use this data to simulate a time series of [CO] for this site. The model simulation in this analysis is still somewhat rudimentary in that temperature fronts are ignored in the model, and the quantum yields and destruction e-folding times are assumed to be constant in space and time. Nevertheless, comparison of this numerical result with a measured time series of [CO] collected during the investigation shows good agreement in several important respects.

In constructing the model from its component parts, the production and loss mechanisms are analyzed individually. The photochemical reaction leading to the formation of CO is not well characterized but is thought to proceed through the

incomplete photodegradation of dissolved organic matter. In general, photodegradation processes depend on the amount of starting material, on the amount of incident radiation at depth z, $E(z,\lambda)$, on the efficiency with which this radiation is absorbed by the starting material, $\epsilon(\lambda)$, on the quantum yield, $\Phi(\lambda)$, and on the directional cosine of the incident light in water, $\bar{\mu}_d$. For a given species P, the photodegradation proceeds according to the following relationship given by Zafiriou et al (1984):

$$\left(\frac{\mathrm{d[P]}}{\mathrm{d}t}\right)_{z,\lambda} = -\frac{\Phi(\lambda)\epsilon(\lambda)E(z,\lambda)[\mathrm{P}]_z}{\bar{\mu}_d} \tag{1.1}$$

This equation assumes first order reaction kinetics for the degradation of species P, though for the specific case of dissolved organic carbon (DOC) the kinetics of the reaction are not clear. Kieber et al (1990) demonstrate that the photochemical production of formaldehyde from coloured dissolved organic matter (CDOM) follows first order reaction kinetics and present convincing data to support their argument (DOC produces many carbonyl compounds on exposure of light; CO and formaldehyde are the most abundant).

If this is true, then it may be assumed that during the photodegradation a certain fraction α of DOC is converted to CO according to

$$\left(\frac{\mathrm{d[CO]}}{\mathrm{d}t}\right)_{z,\lambda} = -\alpha\left(\frac{\mathrm{d[P]}}{\mathrm{d}t}\right)_{z,\lambda}$$

Production of CO thus leads to a depletion of the source material, and laboratory studies have shown that it is possible to deplete the source material to the point where little additional CO is produced (Mopper et al (1991)).

Absorbance studies of seawater show that CDOM absorbs energy in the wavelength range 200–900 nm and that the absorbance increases exponentially with decreasing wavelength (Green and Blough (1994)). This suggests that DOM possesses many functional groups with different absorption properties that give the impression of a continuum of absorbance. Prolonged exposure of CDOM to ultraviolet light causes the destruction of functional groups responsible for absorbance, and this ultimately leads to a decrease in the rate of CO generation. The water sample is then said

to be photobleached. For the purpose of this modelling study, however, the amount of starting material or CDOM is assumed to be constant, and there is an implicit assumption that the CO photoproduction process is not a significant sink for DOC.

The absorption characteristics of DOM are reflected in the wavelength dependence of CO production, known as apparent quantum yield and defined as the ratio of number of moles of CO produced to the number of moles of light of wavelength, λ, absorbed by CDOM. Valentine and Zepp (1993) have been the only workers to date to publish the spectral dependence of quantum yield for CO. Their results indicate an approximately exponential increase in CO production efficiency with decreasing wavelength. Close examination of their data suggests a bi-log-linear distribution of points intersecting very approximately at 360 nm, which may be due to the action of two different production mechanisms with wavelength dependent efficiencies. The results of Valentine and Zepp (1993) and the apparent quantum yield obtained in this investigation are similar to each other, although it is unlikely that DOC derived from different sources should give rise to identical quantum yield spectra. Like DOC and CDOM absorbance, quantum yield is subject to alteration by exposure to ultra-violet light, but this modelling study assumes a constant value.

In addition to the photoproduction process, [CO] in the upper ocean is effected by two important sinks. One of these is an oxidative destruction. The mechanism of the destruction of CO was uncertain until Conrad et al (1982) published a series of dark incubation experiments on filtered and poisoned water samples. Incubation experiments involved unfiltered seawater, 3.0 μm filtered seawater (to remove algae but not bacteria), and 0.2 μm filtered seawater (to remove algae and bacteria). There were significant decreases in [CO] in the unfiltered and the 3.0 μm filtered samples but no decrease in the 0.2 μm filtered samples. No decrease in [CO] was observed when the water samples were poisoned, and with the results of the other work, this suggested that bacteria may have been responsible for CO destruction. Research by Jones et al (1984) suggests that ammonium oxidizing bacteria may be responsible for CO destruction.

Bacterial density would probably vary temporally and spatially in the ocean de-

pending on temperature, nutrient availability, predators, etc. However, this investigation assumes a consumption rate proportional only to the [CO] present.

Conrad et al (1982) also recognized that gas exchange across the surface of the ocean could act as a significant sink for CO. They examined the relationship between daily average sea surface [CO] (normalized to daily mean insolation) and daily averaged wind speed. They found that the degree of supersaturation decreased approximately as the square of wind speed up to 12 ms^{-1} above which it approached equilibrium with the atmosphere. Their results suggest that CO loss through the surface of the ocean may have an important effect on the inventory of CO in the water column.

In constructing the numerical model for [CO], the production, destruction, and degassing mechanisms were coupled with a model that simulated the deepening of the mixed layer in response to solar heating, surface heat loss, and wind stress. This mixing model was developed by Price et al (1986) and assumes that mixing takes place on a time scale faster than production, destruction, and degassing. Thus, the modelled mixed layer cannot support localized vertical property gradients arising from inhomogeneity in the production, destruction, or degassing mechanisms.

The numerical model simulates [CO] by taking account of the production, destruction, and degassing rates controlling the CO budget in the upper ocean while at the same time including a mixing term to account for the dilution effect of entrainment of deep CO-depleted water into the mixed layer. The CO mass balance is summarized by the following equation proposed by Musgrave et al (1988) to describe the seasonal cycling of oxygen concentration in the mixed layer.

$$\frac{\partial [\mathrm{CO}]_m}{\partial t} = \frac{1}{h}\Big[-(\Delta[\mathrm{CO}])w_e + V_p\left([\mathrm{CO}]_{eq.atm} - [\mathrm{CO}]_{z=0}\right) + \kappa_{\mathrm{CO}}\frac{\partial [\mathrm{CO}]}{\partial z}|_h + \int_{z=0}^{z=h} J_{\mathrm{CO}}\,dz\Big]$$

where [CO] is the concentration of carbon monoxide, h is the depth of the mixed layer, w_e is the entrainment velocity ($\frac{\partial h}{\partial t}$), V_P is the piston velocity, J_{CO} is the net production rate (i.e., production minus consumption) of CO, κ_{CO} is the coefficient of

eddy diffusion for CO, $[CO]_{eq.atm}$ is the concentration of carbon monoxide in equilibrium with the atmosphere, $(\ )_m$ is the value in the mixed layer, $(\ )_h$ is the value just below the mixed layer, and $\Delta(\ )$ is $(\ )_m - (\ )_h$. $[CO]_{eq.atm}$ is assumed to be zero for the purpose of calculating CO flux through the surface in the model. (z is positive downward.)

Piston velocity is presented by Liss and Merlivat (1986) according to the following equations:

For $|U_{10}| < 3.6 ms^{-1}$

$$V_p = 0.17 \left(\frac{600}{Sc}\right)^{2/3} |U_{10}| \tag{1.2}$$

For $3.6 ms^{-1} \leq |U_{10}| < 13 ms^{-1}$

$$V_p = 2.85 \left(\frac{600}{Sc}\right)^{1/2} (|U_{10}| - 3.6) + 0.612 \left(\frac{600}{Sc}\right)^{2/3} \tag{1.3}$$

For $|U_{10}| \geq 13 ms^{-1}$

$$V_p = 5.9 (|U_{10}| - 13) \left(\frac{600}{Sc}\right)^{1/2} + 26.79 \left(\frac{600}{Sc}\right)^{1/2} + 0.612 \left(\frac{600}{Sc}\right)^{2/3} \tag{1.4}$$

where $Sc = \nu/D$ is the Schmidt number, ν is the viscosity of water, and D is the molecular diffusivity of carbon monoxide (all functions of temperature). The normalization constant, 600, is the Schmidt number for CO_2 at 20° C, tabulated by Liss and Merlivat (1986).

This equation for the mass balance for [CO] in the mixed layer shows that the time dependent [CO] is a function of the four controlling terms on the right hand side. The first term represents the rate of dilution of mixed layer [CO] due to entrainment of low [CO] water below the base of the mixed layer. The second term represents a decrease in the mixed layer [CO] due to degassing from the surface of the ocean. The third term parameterizes loss of CO through the base of the mixed layer by eddy diffusion effects. The fourth term is the net production, integrated over the depth of the mixed layer.

The third term in this equation, representing eddy diffusion through the base of

the mixed layer, was neglected as being insignificant. Explicit calculation of the depth scale of diffusion may be taken as the square root of the product of the coefficient of eddy diffusion of CO (taken to be on the same order as that for O_2 1.0×10^{-4} m^2 s^{-1}, published by Musgrave et al (1988)) and the characteristic time scale of the model. For a characteristic time scale of one day, the corresponding depth scale of diffusion is 3 m, insignificant compared with averaged mixed layer depth of 60 m.

Numerical simulations conducted with our model showed a good qualitative agreement with measurements of [CO] at the surface and at depth. The assumptions used in constructing the model were thus justified at least to a first approximation. The agreement between the model and observations was thought to be good enough to form the basis of an inverse study which attempts to find the optimized values of certain independent variables controlling the CO budget.

Chapter 2

Field Observations

The CO field experiment study was conducted from the R.V. Oceanus at the BATS site at 31°44'N, 64°11'W and lasted from March 15–24, 1993.

2.1 Methods and Data Set

The investigation included both biogeochemical and physical studies. The chemical study focussed on measurements of [CO] at the surface and at depth and also on the estimation of the destruction and production rates. A summary of the data is given in Table 2.1. Data used for the modelling study described below has been underlined.

The time series of sea surface [CO] is presented in Figure 2-2, and the series of [CO] profiles is given in Figure 2-3. Sea surface [CO] was measured from samples collected in a stainless steel bucket at a frequency that averaged 14 samples per day for the nine day investigation. Subsurface water samples were collected in polyvinylchloride Niskin bottles making up a 12 element CTD rosette. Bucket samples were collected mostly when the ship was stationary (the vessel has to motor back to station about once per day) by lowering the bucket on the rope and letting it roll onto its side so that it filled without a lot of turbulence. Because the mixed layer on almost all days was greater than the draught of the ship, it is suspected that the flow field around the ship would not have influenced the results of the surface [CO] analysis.

There was some ambiguity as to whether the bucket sampling procedure gave

Table 2.1: Database summary. The data used in the modelling described later in this document has been underlined.

Type	Sampling Range	Sampling Interval	Precision	Other Info.
Profiling	March 15–24	$\Delta t \approx 8$h	$T \pm 0.002°$C	26 casts
CTD; T, S, P	2 m$\leq z \leq$ 200 m	$\Delta z = 2$ m	$C \pm$ 0.2 Sm^{-1}	
Profiling	March 15–24	$\Delta t \approx 8$h	$T \pm 0.01°$C	18 casts
XBT; T	2 m$\leq z \leq$ 200 m or 460 m	$\Delta z = 1$m		
Profiling; CO	March 15–24	$\Delta t \approx 8$ h	$\pm 3\%$	CTD
	0 m$\leq z \leq$ 200 m	$\Delta z \approx 40$ m		rosette
Sea surface	March 15–24	$\Delta t \approx 1.5$ h	$\pm 3\%$	bucket
[CO]; see text	$z = 0$ m			samples
Wind speed	March 10–25	$\Delta t =$	± 0.1 ms^{-1}	IMET
	$z = 13$ m above sea level	1 min		[44]
Wind dir.	"	"	$\pm 0.7°$	"
Eppley pyran -ometer I	"	"	$\pm 3\%$ (max)	"
Precip.	"	"	$\pm$ 0.1 mm	"
Air temp.	"	"	$\pm 0.001°$C	"
Sea temp.	"	"	$\pm 0.001°$C	"
Pressure	"	"	± 0.1 mb	"
Wind speed	March 16–25	$\Delta t = 1$ h	± 0.1 ms^{-1}	Alti-
	$z = 3$ m above sea level			moor buoy
Wind dir.	"	"	$\pm 0.7°$	"
Wind speed	March 10–25	$\Delta t = 4$ h	± 0.3–5 ms^{-1}	deck log
Wind dir.	"	"	$\pm 15°$	"
Sea state	"	"	$\pm$ 0.5–1 m	"
Wave swell	"	"	$\pm$ 50 m	"
Wave dir.	"	"	$\pm 15°$	"
Air temp.	"	"	$\pm 0.3°$C	"
Sea temp.	"	"	$\pm 0.3°$C	"
Pressure	"	"	$\pm$ 0.5 mb	"
Wind speed	March 15–25	$\Delta t = 1$ h	± 0.26 ms^{-1}	Nav. Air
	$z =$9.1 m			Station
Wind dir.	"	"	$\pm 5°$	"
Air temp.	$z = 1.8$ m	"	$\pm 0.3°$C	"
Pressure	$z =$2.7 m	"	± 0.2 mb	"
Rel. humidity	$z = 1.8$ m	"	$\pm 1\%$	"
Cloud cover	octas	"		"

results that were representative of the [CO] of the mixed layer as determined by Niskin bottle samples. In this regard, it was not certain if the bucket samples were biased by degassing during the sampling procedure or if positive or negative gradients of [CO] could exist within the mixed layer due to production or degassing (both strongly surface-trapped phenomena). To test the hypothesis, the difference in [CO] between the bucket sample and the shallowest Niskin bottle sample was plotted versus time of day for all 21 of the [CO] profiles recorded. These results are shown in Figure 2-1 and show mostly a negative difference (i.e. [CO] for surface bucket is lower that of the first Niskin bottle) in morning and evening and mostly a positive difference about midday. Keeping only those data where the bucket measurement and the first Niskin bottle are both within the mixed layer (i.e. determined from the measured temperature profiles using the criterion established in Section 5.3.1), then almost all positive deviations are excluded. This suggests that positive gradients cannot exist within the mixed due to light-induced production. It also implies that either negative gradients can exist within the mixed layer due to degassing or that there might be some degassing-associated bias in the bucket sampling procedure or that both possibilities might be true. With respect to the first possibility, some of the negative discrepancy might be due to a skin effect, but it is difficult to believe that this could account for the magnitude observed. It seems clear that these results are not sufficient to resolve the difficulty, and subsequent studies might repeat this kind of analysis with the mixed layer defined in terms of density and not temperature.

Subsamples were collected from the bucket and Niskin bottles using glass syringes with plastic valve fixtures at the tips. Although it is true that the rosette bottles and syringe valve fixtures were made of organic materials, seawater samples were not kept in contact with these elements for a long enough period of time for CO contamination to be a problem.

During the CO measurement procedure, a 50 mL syringe was rinsed at least three times with the samples of the seawater to be measured. A 40.0 mL sample was drawn taking extreme care not to introduce air bubbles into the sample. A 5.0 mL sample of CO free air was introduced to the syringe, and the CO in the seawater/air mixture was

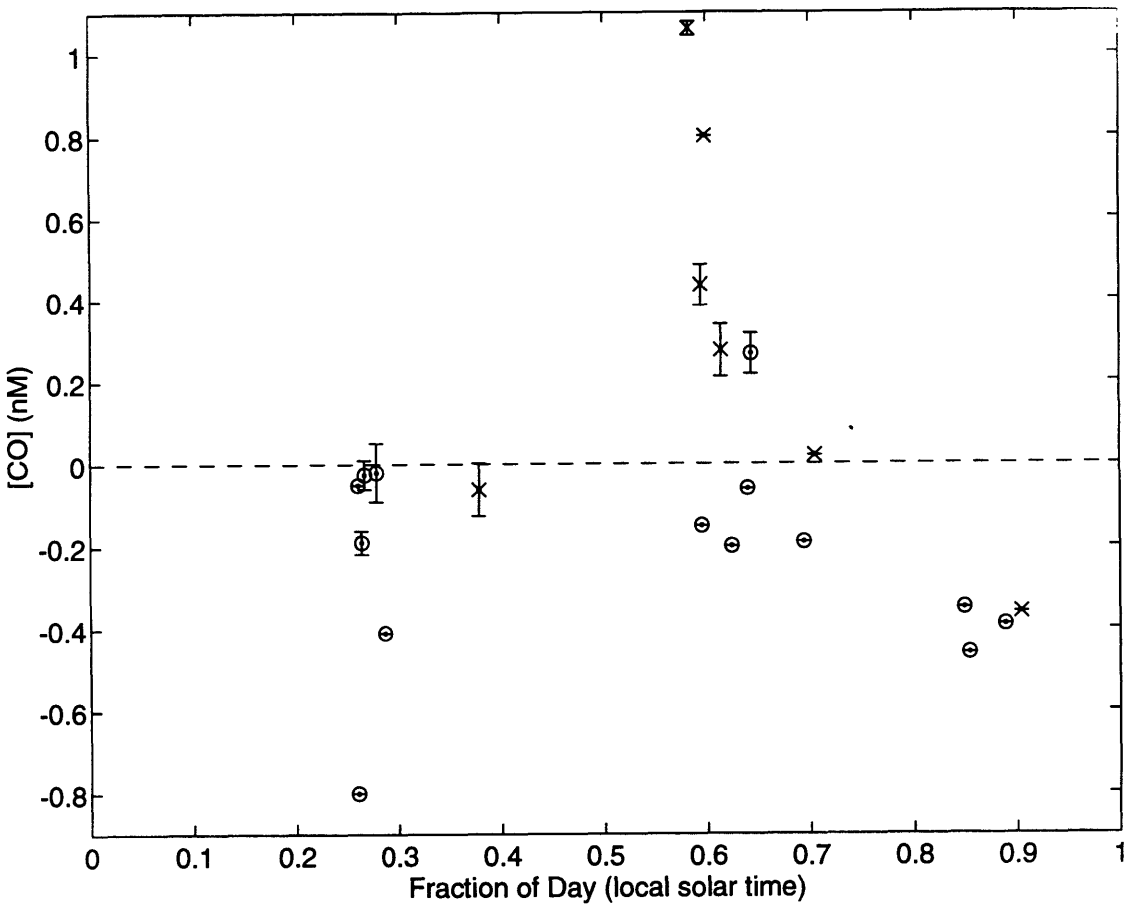

Figure 2-1: Deviation between sea surface concentration of CO and that of shallowest Niskin bottle sample plotted against fraction of day. The centered circles indicate stations where the depth of the mixed layer was deeper than the shallowest Niskin sample (the depth of the mixed layer being obtained from the measured CTD temperature profiles using the criterion given in Section 5.3.1). The crosses indicate those stations where the shallowest Niskin bottle sample was deeper than the mixed layer depth. Excluding the data marked by crosses suggests that positive gradients in [CO] due to photo-production can not exist within the mixed layer. At the same time, this exclusion does suggest that either negative gradients can exist within the upper mixed layer due to surface degassing or that there might be a bias in the bucket sampling procedure or that or that both possibilities might be true.

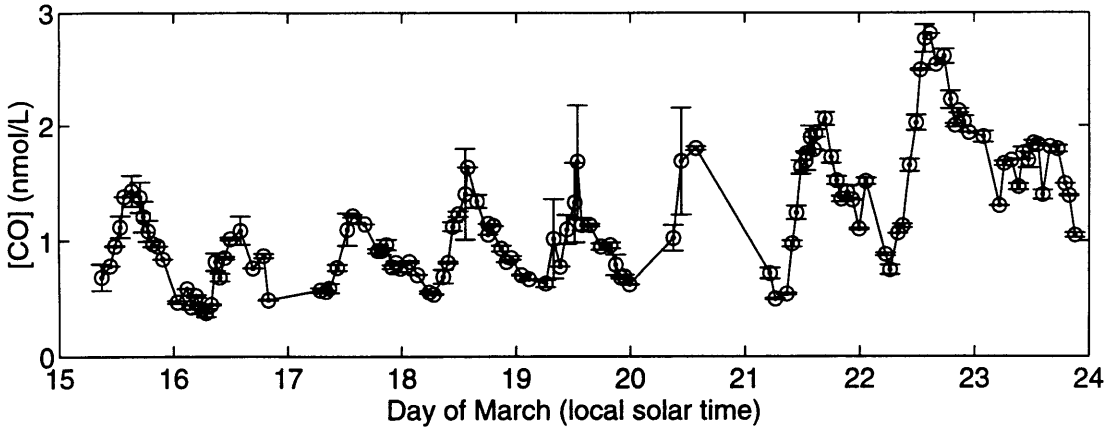

Figure 2-2: Time series of sea surface [CO]. Uncertainties in the measurements are indicated by error bars which represent a standard deviation of two or three measurements if these were available at a given time.

equilibrated by shaking 5 minutes in a wrist action shaker. Next, the air sample was drawn off and injected into a gas chromatograph (RGA-3 Reduction Gas Analyzer) with a modified inlet system (Figure 2-4) and a HgO-Hg detector. Output from the detector was recorded as a peak in the line trace of a Hewlett-Packard integrator. The area of the peak was converted to a gas concentration by comparison with the interpolated results of a 1 ppmv CO in air standard which was analyzed periodically. The detector/integrator was assumed to have a linear response in the range 0-1 ppmv, although this was not tested with a second standard.

The equilibrium aqueous [CO] was calculated by assuming a mass conservation condition and using:

$$[\mathrm{CO}]_{eq.atm} = \mathrm{Bm}P \tag{2.1}$$

where $[\mathrm{CO}]_{eq.atm}$ is equilibrium concentration of gas (mL gas/mL H_2O), B is the Bunsen solubility coefficient (mL gas/(atm mL H_2O)), P is the atmospheric pressure at sea level (atm), and m is the volume mixing ratio of the gas in surface air. The Bunsen coefficient, B, varies as a function of temperature and salinity (Weisenburg and Guinasso (1979)).

Figure 2-3: Record of [CO] profiles measured during March 15–24, 1993

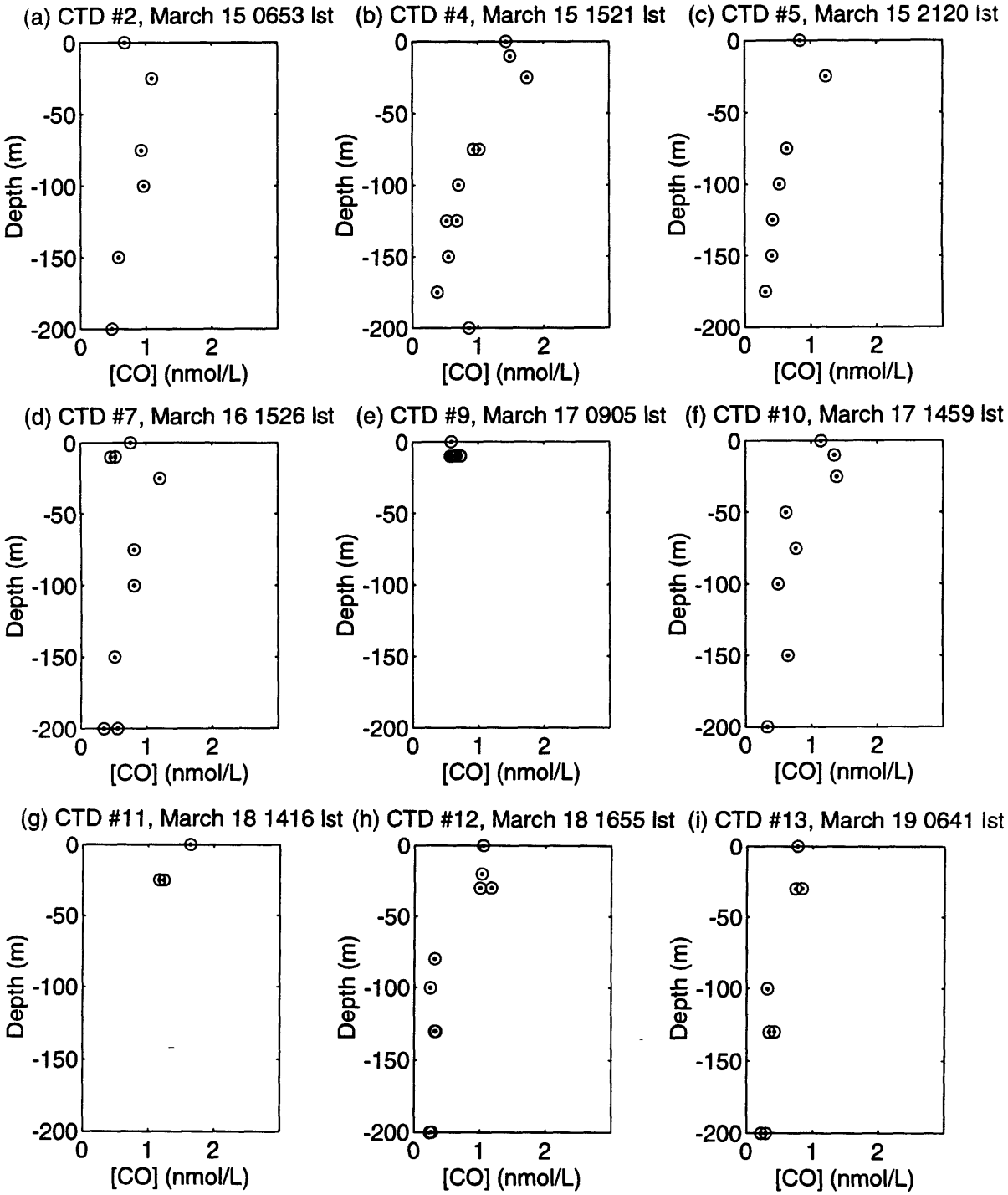

(j) CTD #14, March 19 1400 lst (k) CTD #15, March 19 1640 lst (l) CTD #16, March 20 0624 lst

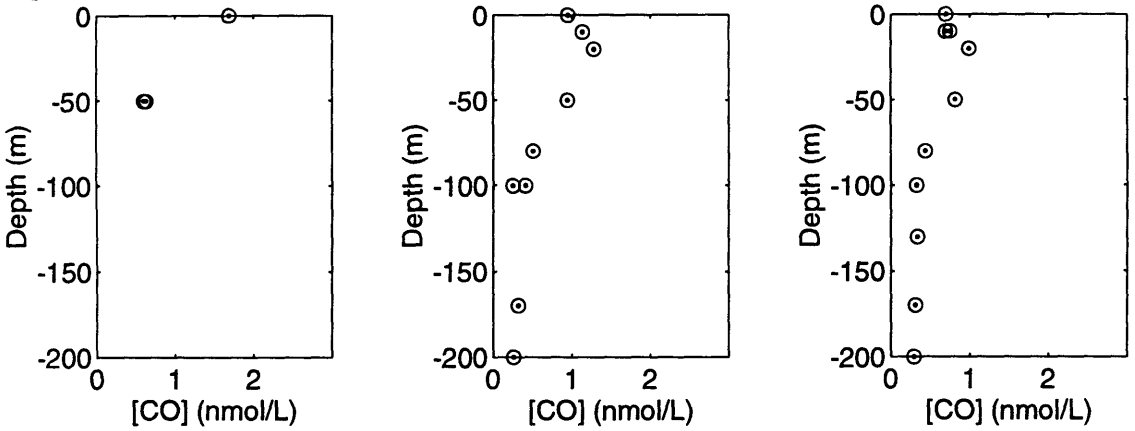

(m) CTD #18, March 21 0620 lst (n) CTD #20, March 21 1444 lst (o) CTD #22, March 21 2030 lst

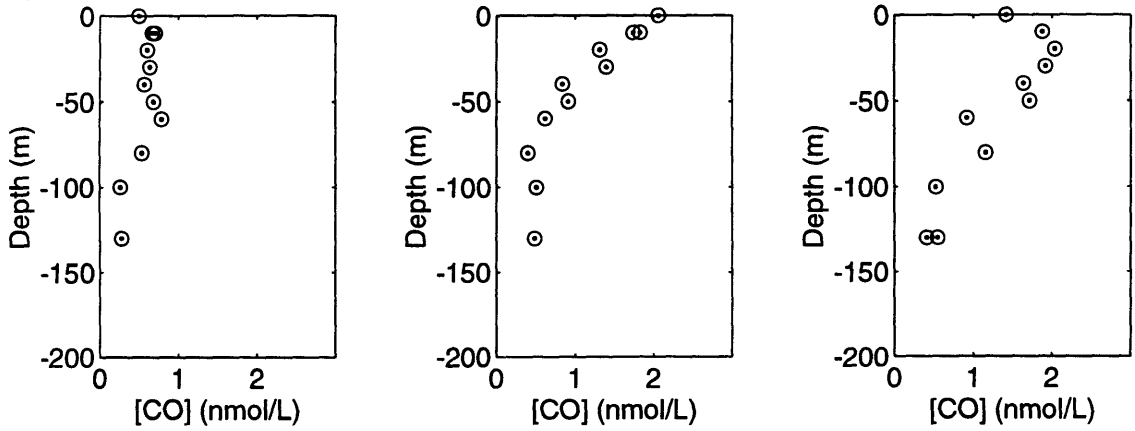

(p) CTD #23, March 22 0615 lst (q) CTD #24, March 22 1422 lst (r) CTD #26, March 22 2143 lst

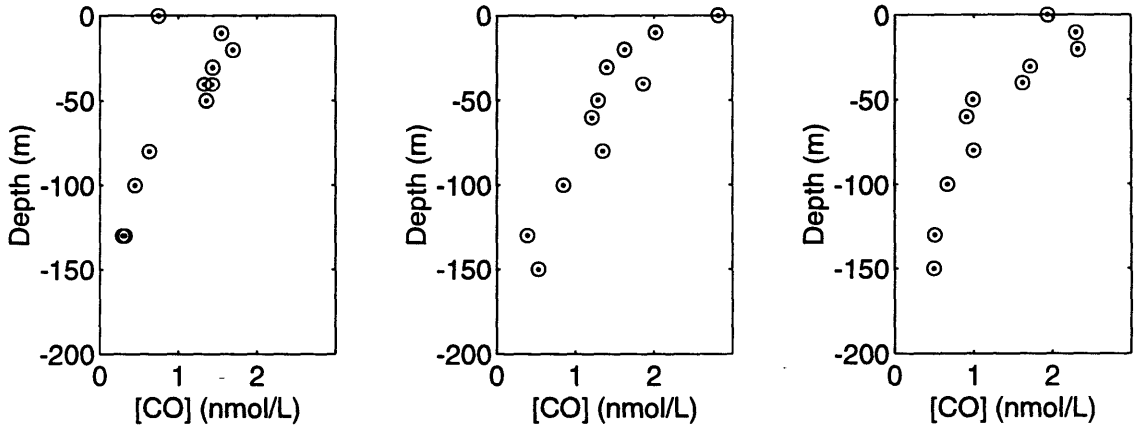

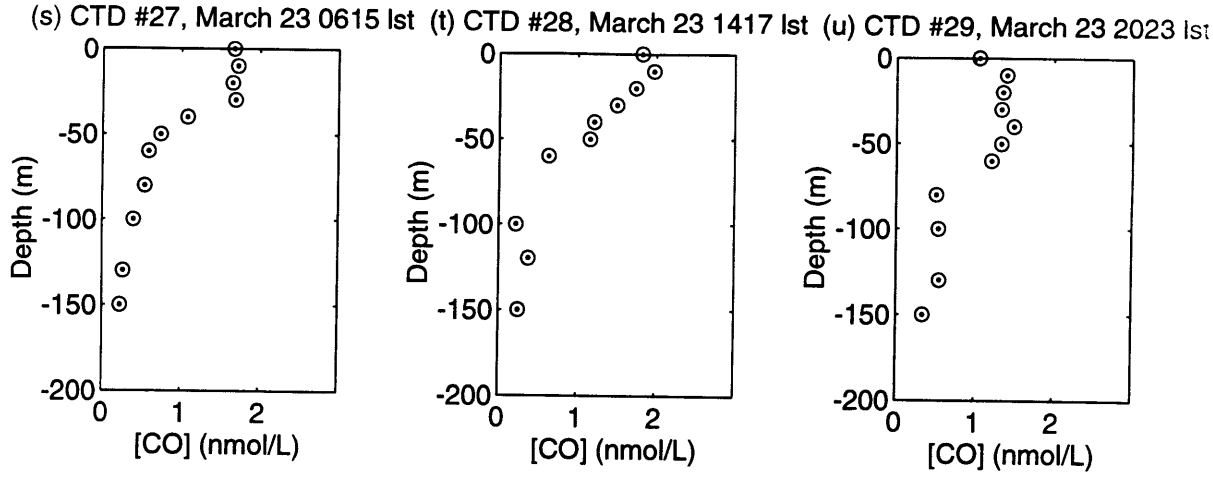

A total of 26 useful CTD casts were were obtained during the 9 day investigation period giving temperature and salinity measurements mostly to 200 m or less. Some casts were characterized by anomalous temperatures near the surface, and in these cases bad data (identified as density inversions of 0.02 kg m^{-3}) near the surface were discarded.

An additional 18 temperature profiles were obtained with expendable bathythermographs (XBT) to 200 and 460 m. Many of these 18 casts had surface temperature values which spiked 1–2°C higher or lower than the ambient mixed layer temperatures. This anomaly arose from an electrical transient associated with the sudden completion of a circuit when the instrument contacted the water. Because of this, the uppermost 5 data points were discarded from all casts, so that the XBT records effectively start at 3.88 m. A summary of the XBT and CTD data are shown in the series of 44 temperature profiles given in Figure 2-5.

Also, underwater spectra were recorded using a LICOR 1800UV instrument near solar noon on March 21–23, 1993. These measurements involved first recording a sky spectrum on the deck and then lowering the upward-looking instrument into the water column on a steel cable. Underwater spectra were recorded at a series of depths ranging from from 5–80 m, below which the light levels at most wavelengths in the measurement range (300-850 nm) fell below the detection limits of the instrument.

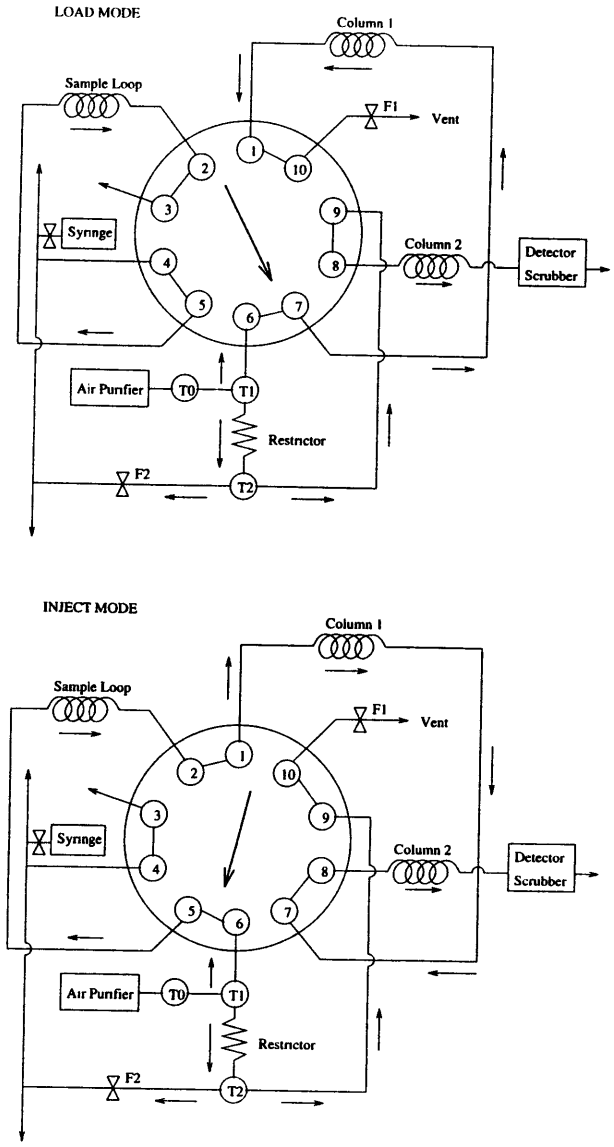

Figure 2-4: Valve inlet system for RGA-3 Reduction Gas Analyzer. The instrument had two operational modes: a load mode shown in the upper diagram and an inject mode shown in the lower. The plumbing layout is almost the same as that for the original instrument. The details of the sample injection system were altered for this experiment to accommodate a syringe that could be flushed with CO-free air from valve F2. A 0.2 μm in-line filter was placed between the syringe and the gas chromatograph to avoid unintentional injection of seawater into the instrument. As well, a series of three way valves in the tubing around the syringe permitted the syringe to be flushed with CO-free air generated by the instrument.

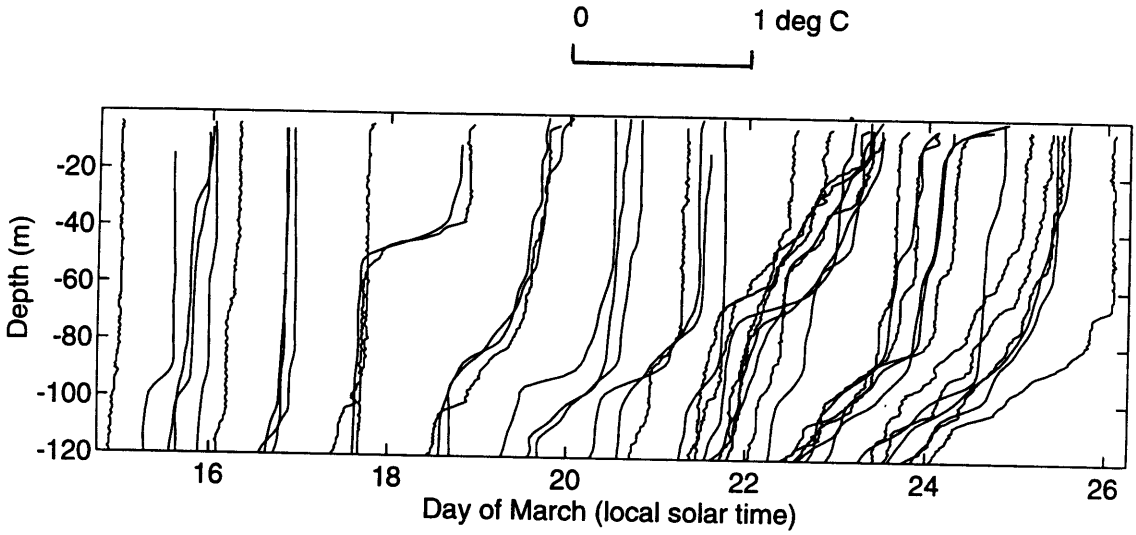

Figure 2-5: Time series of recorded temperature profiles to 120 m. The times of the profiles are indicated by their intersection with the bottom axis. The jump in temperature at 40 m on March 17 is probably due to the advection of a temperature front and is consistent with the discontinuity in the sea surface temperature profile. The near surface structure in the profiles on March 21-22 indicates the heating cycle leading to the formation of a diurnal thermocline.

Table 2.2: Depths at which underwater spectra were recorded. The numbers in parentheses denote the number of spectra that were recorded at that depth for a particular day; no parentheses mean that one spectrum was recorded.

Date	Depths at which Underwater Spectra Recorded (m)
March 21	deck(2), 5(2), 10, 20, 40
March 22	deck, 5(2), 10, 20, 40, 60(2)
March 23	deck(2), 10(2), 15(2), 25(2), 40(2), 60(2), 80

Specifications for the depths at which spectra were recorded is given in Table 2.2. These spectra allowed a parameterization of the transparency of the water in the range 320–600 nm. Calculation of the diffuse attenuation coefficient, $K_d(\lambda)$, was made according the Beer-Lambert law assuming no depth dependence. The procedure used for this calculation is described in Section 4.5.

Finally, shipboard measurements of wind speed, wind direction, barometric pressure, precipitation, air temperature, sea temperature, and insolation were made when the ship was on station between March 14–24. Because of some inadequacies in this data set, it was supplemented with data collected at the naval air station approximately 45 km northward. Meteorology data were also available from the deck log recorded by bridge personnel during the investigation period and from a meteorology buoy (part of the Altimoor experiment) which was also at BATS and transmitted data from 2300 GMT on March 16, 1993.

A meteorology file was constructed for the BATS site for the period, March 14–25, 1993, by using the all of the data from the ship's automatic meteorology recording system (IMET) for the period March 14–25 except for the wind direction. The wind direction was interpolated from data obtained from the naval air station at Bermuda for the period March 15–25 and from the deck log report for March 14. Relative humidities were obtained from the naval air station. The momentum and heat fluxes were calculated at one minute intervals over the investigation period (the recording frequency of the ship's IMET system), and then were binned into ten minute averages. This smoothed small spikes remaining in the data record and created a data file with a more manageable size.

The sea surface temperature time series is especially significant for this study because it should reflect any diurnal temperature cycles at the BATS site. The sea surface temperature, recorded by a thermistor mounted at 3.5 m depth in a cooling water intake in the ship's hull, is given in Figure 2-6 for the March, 1993 investigation. The uppermost temperature taken from the 44 profiles recorded by the XBT and CTD instruments has been superimposed on this trace as a means of corroborating the original data set. The record is characterized by significant temperature jumps exceeding 0.2°C on March 15, 17, 18, and 21. These are probably due to horizontal advection; such thermal fronts have been recorded by other investigators for the Sargasso Sea (eg. Colton et al (1975) and Cornillon et al (1986)). On March 21 and 22 the sea surface temperature increases by about 0.2°C in a characteristic diurnal temperature cycle which has been explained by Price et al (1986). The high mean insolation and low wind stress on these days inhibited deep mixing and caused the formation of a warm shallow mixed layer most easily observed in the sea surface temperature record. On other days, the sea surface temperature signal either was very small due to deep mixing by high wind events or else was obscured by the passage of thermal fronts.

2.2 Meteorology and Air-Sea Fluxes

The BATS site had just emerged from a period of gale force winds and some precipitation when the station was occupied late on March 14, 1993. The high wind stress continued into the beginning of the investigation. This not only caused enhanced wind mixing but also served to increase the amount of heat lost from the surface of the ocean. Clouds covered most of the sky during the investigation period and caused a decrease in the rate of heat input by insolation. Except for the precipitation event, conditions at the beginning of the investigation favoured deep mixing and the suppression of the formation a diurnal thermocline.

The wind speed was highest near the beginning of the investigation with values between 12–18 ms^{-1} on March 14 and decreased gradually to a minimum of about 4

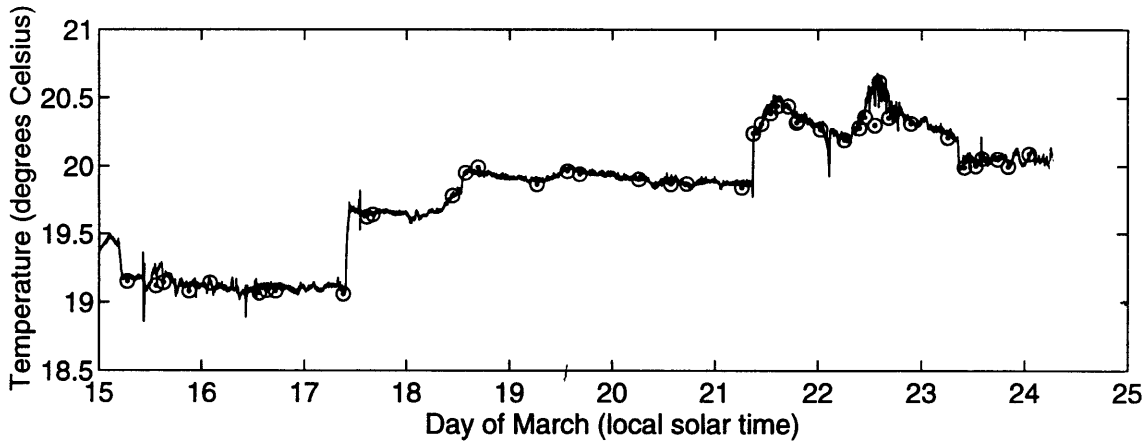

Figure 2-6: Sea surface temperatures measured during the March 14–25, 1993, investigation period. The record is characterized by discontinuities up to 1°C on March 15, 17, 18, and 21 indicative of the passage fronts through the BATS site. This is not the result of instrument failure and was verified against the CTD and XBT records whose uppermost temperatures are indicated by centered circles on this plot. This times series suggests that there may have been two days (March 21 and 22, 1993) when a significant diurnal temperature cycle was present. March 18 and 19 may also show evidence of a smaller temperature increase consistent with higher wind speeds on these days.

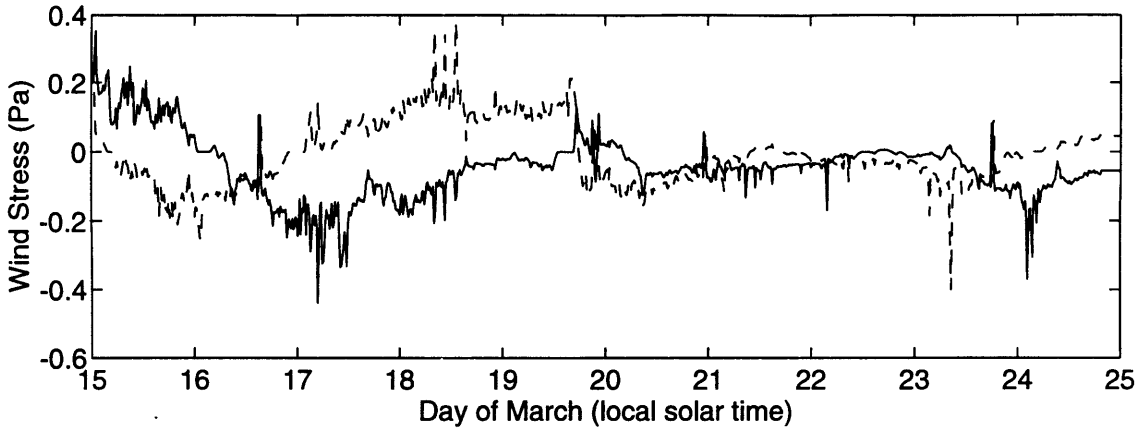

Figure 2-7: The north component of wind stress is given by the dashed line, and the east component is given by the solid line. The directions are positive when the wind is blowing toward the east and north (i.e. oceanographic convention)

ms^{-1} on March 22. Wind direction was also variable during the investigation with a clockwise rotation two and a half times around the compass.

Wind stress was calculated according to:

$$\tau = \rho_a C_D U \mathbf{U} \tag{2.2}$$

where $\rho_a = 1.23 kgm^{-3}$ is the density of air, and C_D is the drag coefficient computed by Large and Pond (1981). The estimated wind stress varied by over an order of magnitude from about 0.2 Pa on March 15–18 to 0.02 Pa on March 22. Time series of the east and north components of wind stress is shown in Figure 2-7, and the magnitude of wind stress is shown in Figure 2-8.

The net heat flux, Q, is the sum of insolation I, which was directly measured, and surface heat loss, L, which is itself comprised of the sum of latent, sensible, and long-wave radiative heat fluxes;

$$Q = I + L \tag{2.3}$$

These latter fluxes were calculated from air-sea observations following the formulation of Large and Pond (1982). The mean values of latent, sensible, and long-wave

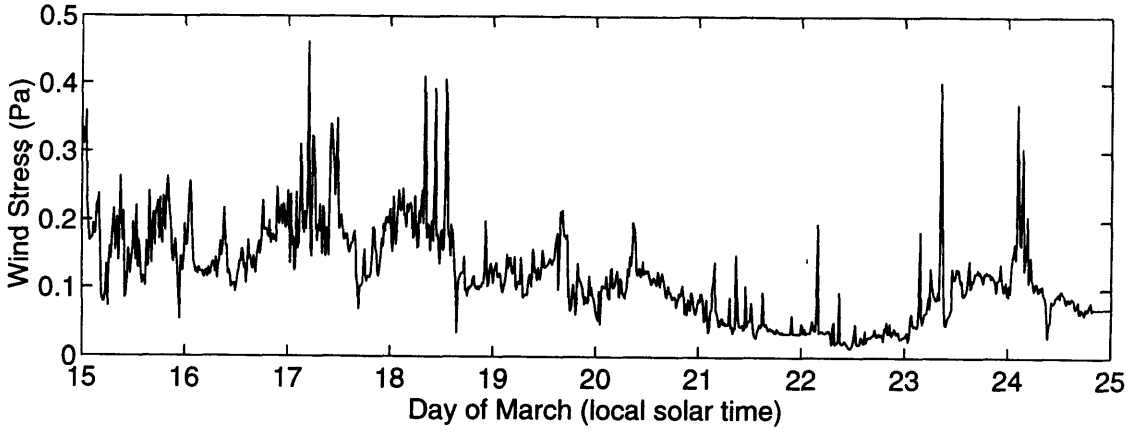

Figure 2-8: Time series of the magnitude of wind stress. The anomalous spikes in this data record probably represent anomalies in the automatic data recorder that fell below threshold levels for bad data in the processing routine. These anomalous spikes only last for the 10 minute time step and probably do not influence model results significantly

radiative heat fluxes and their sum are shown in Table 2.3 along with the corresponding mean values for this region in March as estimated from "The Bunker Climate Atlas of the North Atlantic Ocean". The Bunker Atlas values are subject to an uncertainty of about 10 Wm^{-2} and the calculated heat fluxes are also subject to about the same level of uncertainty. The table indicates that the heat fluxes during the period of investigation were typical of what has been compiled in the database. A time series of the insolation and net heat loss are shown in Figure 2-9. Figure 2-10 shows integrals in time of the measured and theoretical clear sky insolation reset for each of the days of the investigation. The theoretical clear sky insolation was calculated using List (1984) according to the procedure described in Section 4.3.

Finally, the integrated precipitation record is shown in Figure 2-11. The record shows a single rain event on the night of March 19–20.

Table 2.3: Comparison of heat fluxes computed in this study and given in the Bunker Climate Atlas

Heat Flux Term	10 Day Mean from this Investigation Wm^{-2}	March Mean from Bunker Atlas [14] Wm^{-2}
Latent Heat	-120	-79
Sensible Heat	-20	-18
Long-wave Radiative Heat	-45	-67
Sum of Heat Fluxes	-185	-164

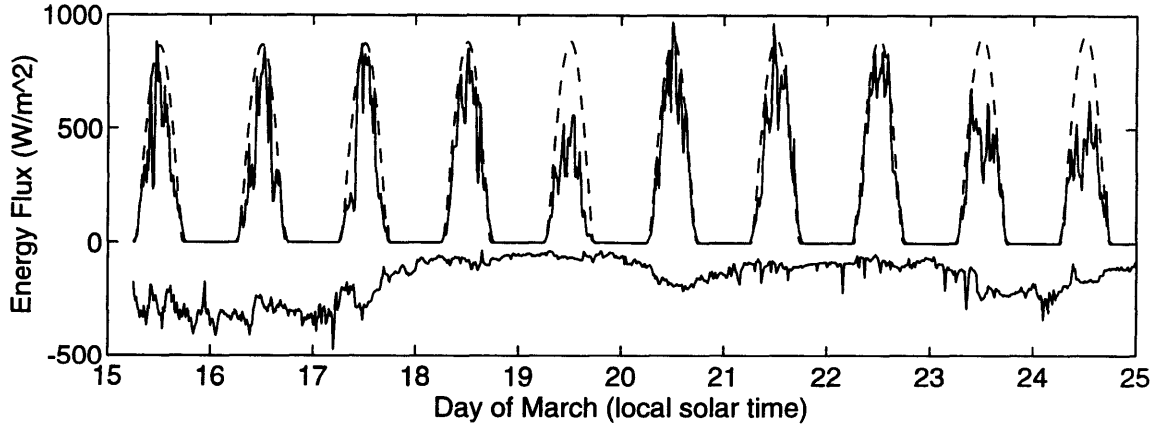

Figure 2-9: Time series of insolation (solid line above) and heat loss (solid line below) for the investigation period March 14–25, 1993. Maximum theoretical insolation is given by the dashed line above the solid measured insolation trace. The site was cloudy to some extent for the entire period as is indicated by the irregular spikes in the insolation record. Low insolation on March 23 leads to a suppresion of the sea surface [CO] on this day. High sensible and latent heat losses at the beginning of the investigation are caused by high surface winds.

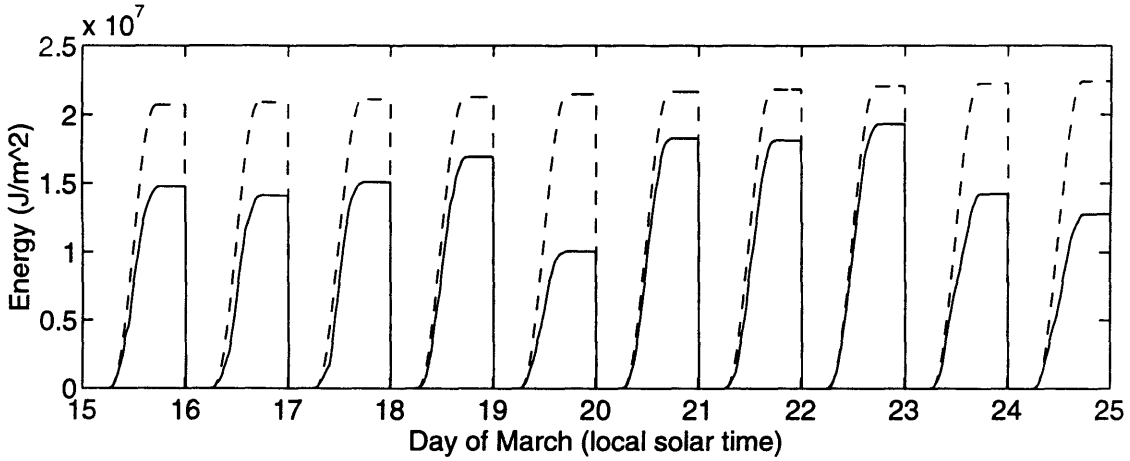

Figure 2-10: Time-integrated measured and theoretical clear sky insolation. The theoretical clear sky insolation was calculated from List (1984) according to the procedure described in Section 4.3. The record shows that there was lower relative net input of insolation energy on March 19 and 23. For March 23 this helped to contribute to an ambiguous increase in sea surface [CO] during the day.

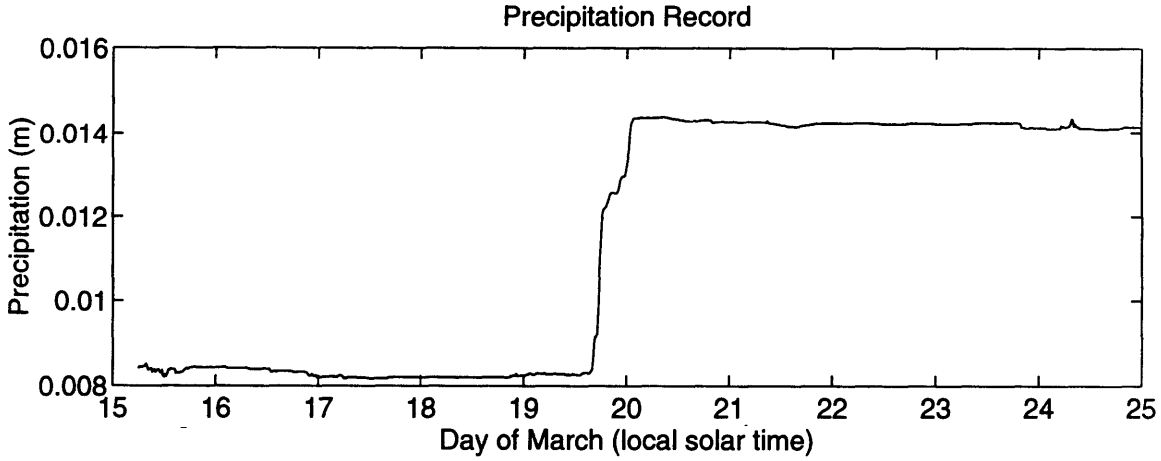

Figure 2-11: Integrated precipitation record

Chapter 3

Laboratory Experiments

Shipboard and laboratory experiments performed as part of this investigation established values for the rate constant of CO destruction and the wavelength dependence of CO production. Dark incubation experiments were used to determine the rate constant for CO disappearance during the period of the March, 1993 investigation. The wavelength dependence of CO production was performed in a series of seawater irradiation experiments with a light source whose power output had been accurately determined. The light-production and destruction mechanisms were thought to be the most important terms in the CO budget of the mixed layer, and laboratory experiments provided one means of assessing their values.

3.1 Dark Incubation Experiments

CO consumption rate was determined by performing dark incubations of unfiltered sea water samples during the time of the March, 1993 investigation. Published studies suggest that bacteria are responsible for CO consumption and that the CO depletion follows quasi-first order reaction kinetics at ambient CO concentrations.

The dark incubation experiments were carried out on March 15, 16, 17, 18, and 20, 1993. Water samples were collected at five or six different depths down to 200 m with the CTD rosette. Three to five samples were drawn (in the manner of dissolved O_2 samples to minimize changes in dissolved gas concentrations) from each of the five

or six rosette containers of interest and were placed in 200 mL glass bottles that had been covered with electrical tape to make them opaque to light.

These bottles were stored at room temperature $21 \pm 2°C$ for various times up to 30 h. After an accurately known incubation period, the dark incubation bottles were unsealed and the water was analyzed for [CO] using the gas chromatograph. Care had to be taken in unsealing the bottles because seawater tended to accumulate in a lip around the stopper where water was forced out when the bottles were sealed. Before the analysis this stagnant water sitting in the lip was removed to avoid contamination of the sample. 23 dark incubation experiments were conducted during the investigation period but 9 have been excluded from this analysis either because the initial [CO] was unknown or because one or more points showed significant contamination effects.

The results of the dark incubation analyses are shown in Figure 3-1 (the data are tabulated in Appendix B) showing plots of $\ln(\frac{[CO](t)}{[CO](t=0)})$ versus incubation period arranged by CTD station number and depth. In general, the results conform to expectations in that there is a (linear) monotonic decreasing trend with incubation time. The data were fitted with lines of best fit according to a model of exponential decay given by the following equation:

$$\frac{d[CO]}{dt} = -\frac{1}{\tau_c}[CO] \tag{3.1}$$

where τ_c is the e-folding time constant for the reaction.

The exponential decay model used to fit the data implicitly assumes that the [CO] of water kept in darkness should vanish at long times. However, measurements in the deep ocean show that [CO] never vanishes but instead attains a small, nearly constant level of about 0.25 nmol L^{-1} below the euphotic zone. This departure from quasi-first order rate kinetics may be explained in terms of a blank correction that may be necessary for the concentration measurements, the absence of CO-consuming bacteria below the euphotic zone, the requirement of a threshold [CO] for microbial consumption, or the presence of a small amount of dark production of CO at depth.

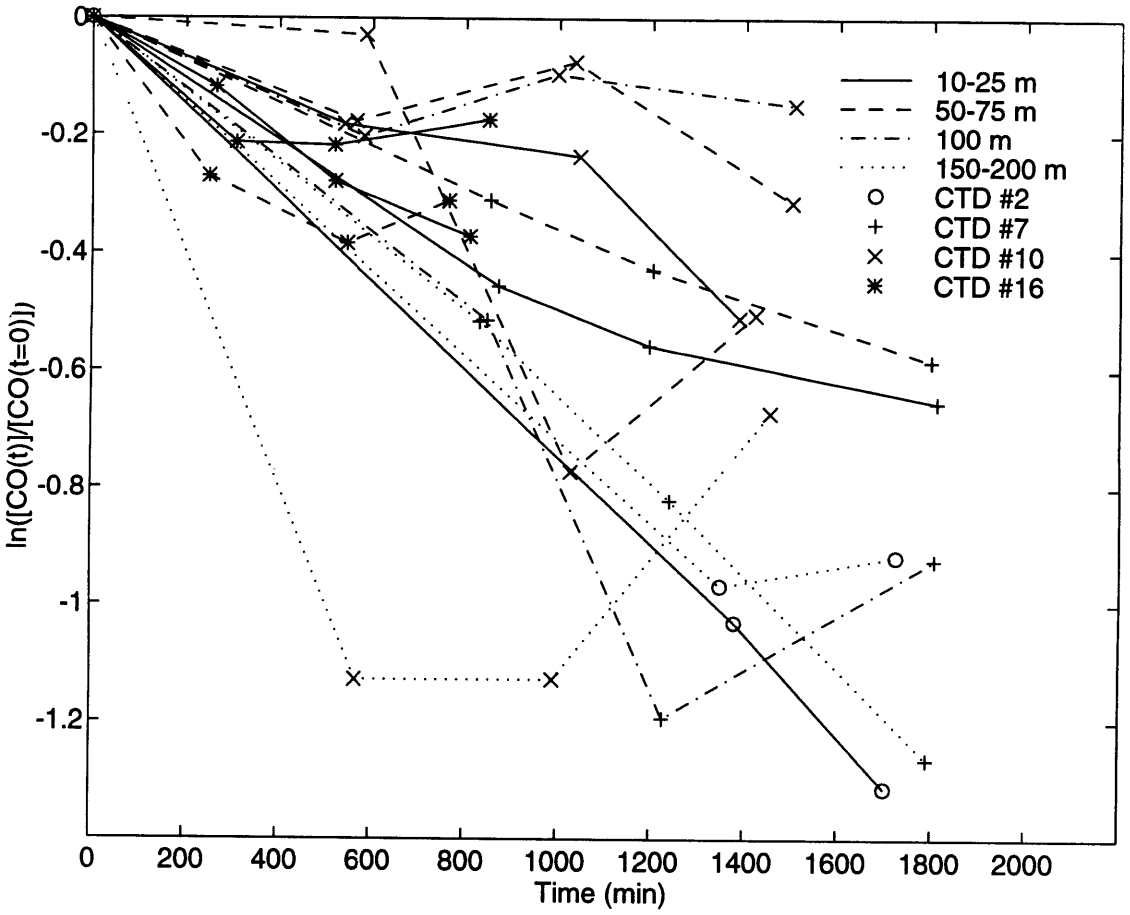

Figure 3-1: Results of the dark incubation experiments plotted as $\ln(\frac{[CO](t)}{[CO](t=0)})$ versus incubation period. The results for 14 dark incubation experiments are shown; 9 others were excluded on the basis of significant contamination effects or the absence of an initial measured [CO].

However, the first order decay model does describe the main trend of the data, especially at high [CO]. The reciprocal of the slopes of the lines of best fit to the $\ln(\frac{[CO](t)}{[CO](t=0)})$ versus incubation period data describes e-folding time of CO consumption, and the scatter of data away from the line of best fit parameterizes an error. Figure 3-2 shows the e-folding CO consumption times plotted against the depths of the water samples along with the uncertainties in the e-folding times. There is considerable scatter in the measured e-folding consumption times as they are presented in this plot. The significant uncertainty associated with individual points makes it difficult to assess if e-folding consumption time has a depth dependence. For the purpose of the modelling study, it was decided to assume no depth dependence and calculate an average for all depths and times. The mean e-folding consumption time (determined by shipboard incubation) for all 14 points was 57 ± 52 h while the mean for the depths at 75 m or shallower was 52 ± 25 h. This latter average was used for the baseline value in the modelling study.

Published measurements of this time constant by other researchers is presented in Table 3.1. These published data show that the e-folding time of CO consumption has been measured in the range 1–500 h depending on the time of year, the location, and possibly the measurement technique. The value obtained in this investigation was typical compared to the other results, although a detailed comparison is not possible given the large uncertainty of experimental result.

The scatter in the values for the e-folding consumption times of CO in both this experiment and published studies indicates that this parameter may be subject to considerable uncertainty (of possibly up to 70%) or that it is subject to great temporal and spatial variation. For this study, the most likely cause of the scatter is the uncertainty introduced by contamination of incubation samples during the measurement technique. Given this large uncertainty in the experimental quantities, a numerical modelling study could help to constrain the value of the e-folding consumption time for CO.

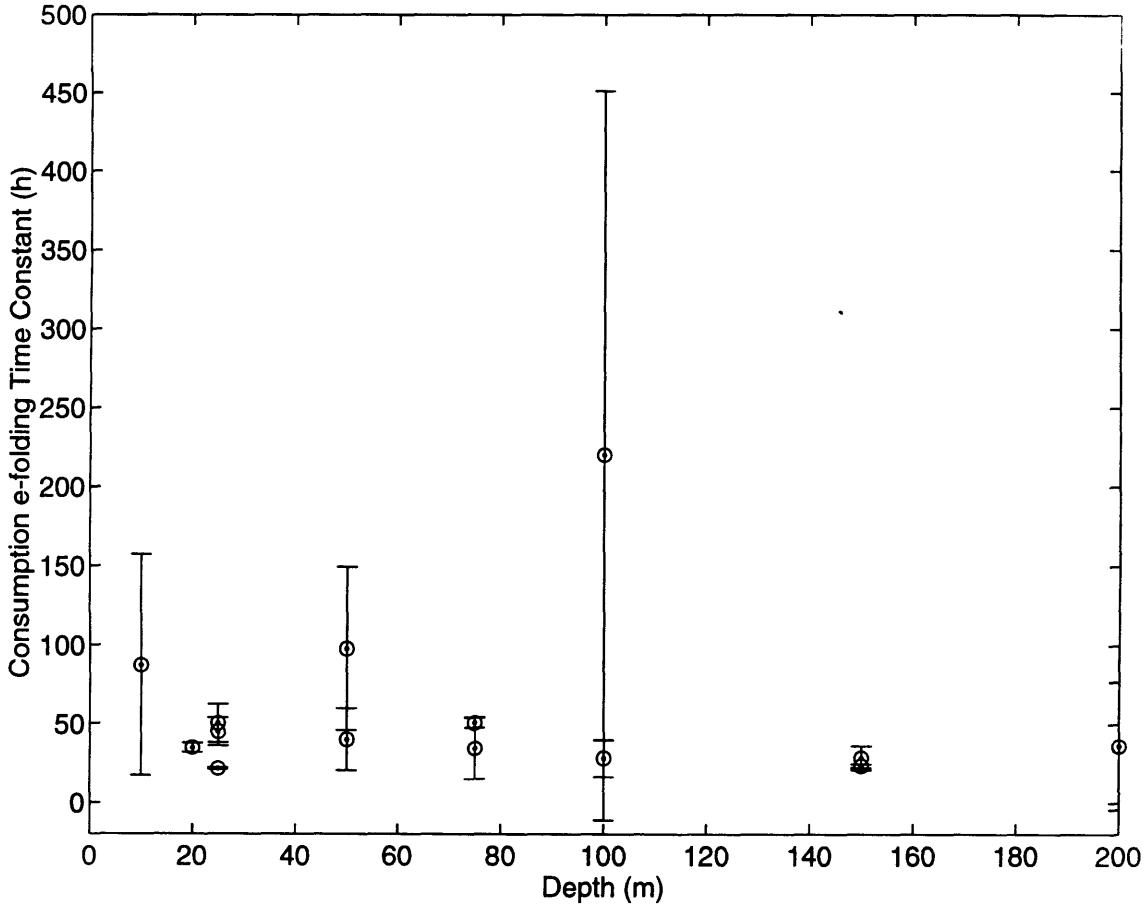

Figure 3-2: Depth dependence of the e-folding consumption time of CO in the mixed layer. The uncertainty in the data is given by the vertical bars representing one standard deviation.

Table 3.1: Assembled literature values of e-folding CO consumption times

Location	Source	Time Constant τ_c (h)
Atlantic Ocean, 3.0 μm filter	[4]	4.8
Atlantic Ocean, no filter	[4]	3.4
lake water	[5]	0.85
Atlantic Ocean, no filter	[5]	20.8
Sargasso Sea, no filter	[16]	44.6–446
Sargasso Sea, no filter	[16]	40
Station B, Spring, south Caribbean Sea	[17]	88
Station F, Spring, south Caribbean Sea	[17]	39
Station P5, Spring, Gulf of Paria	[17]	34
Station P3, Spring, Gulf of Paria	[17]	53
Station P1, Spring, Gulf of Paria	[17]	70
Station R9, Spring, Orinoco outflow	[17]	16
Station R7, Spring, Orinoco outflow	[17]	16
Station R6, Spring, Orinoco outflow	[17]	19
Station R5, Spring, Orinoco outflow	[17]	9
Station R4, Spring, Orinoco outflow	[17]	14
Station R3, Spring, Orinoco outflow	[17]	15
Station R2, Spring, Orinoco outflow	[17]	2
Station R1, Spring, Orinoco outflow	[17]	7
Station R4, Spring, Orinoco outflow	[17]	108
Station A, Fall, south Caribbean Sea	[17]	98
Station D, Fall, south Caribbean Sea	[17]	25
Station G, Fall, south Caribbean Sea	[17]	14
Station L, Fall, south Caribbean Sea	[17]	8
Station M, Fall, south Caribbean Sea	[17]	8
Station O, Fall, south Caribbean Sea	[17]	6
Station P5, Fall, Gulf of Paria	[17]	3
Station P4, Fall, Gulf of Paria	[17]	4
Station P3, Fall, Gulf of Paria	[17]	5
Station P1, Fall, Gulf of Paria	[17]	7
Station R7, Fall, Orinoco outflow	[17]	6
Station R6, Fall, Orinoco outflow	[17]	4
Station R5, Fall, Orinoco outflow	[17]	4
Station R4, Fall, Orinoco outflow	[17]	3
Station R3, Fall, Orinoco outflow	[17]	4
Station R2, Fall, Orinoco outflow	[17]	7
Station R1, Fall, Orinoco outflow	[17]	6

3.2 Irradiation Experiments

A series of experiments were performed after the end of the cruise to assess the CO production capacity of seawater upon exposure to different wavelengths of light. The purpose of these experiments was to find the apparent quantum yield characteristic ($\Phi(\lambda)$) of the seawater. Measurements in the laboratory of seawater samples recovered from the site produced good results which were consistent with published data.

3.2.1 Experimental Determination of Quantum Yields

A series of irradiation experiments was done after the March, 1993 investigation period to assess the wavelength dependence of the photoproduction of CO by DOC in seawater. Samples were collected from the sea surface at BATS on September 24, 1993 in 750 mL glass bottles that had previously been acid-washed. This water was stored in the dark at room temperature for about 3 months before the analyses. Water samples were also collected at the sea surface near Cape Henlopen (38°48.76'N, 75°05.93' W) on November 11, 1993, and stored for a shorter period before analysis.

The analysis procedure consisted of measuring the [CO] of seawater samples that had been exposed to an artificial light source for a precisely measured interval of time. For the case of the Cape Henlopen samples, the water samples were first filtered with a 0.2 μm filter. A 2 L sample of either the Cape Henlopen or BATS seawater was placed in an Erlenmeyer flask that had previously been rinsed with small amounts of the sample to be measured. The sample was stirred with a teflon coated magnetic stir bar and bubbled with CO-free air for about 14 hours to ensure that the [CO] in the sample was at a minimum value (The stirring and bubbling were such that the e-folding time to flush the 2 L sample of its CO was about one hour). Then a quartz irradiation cell (31.05 cm long, 2.54 cm diameter, and 116.1 mL interval volume) was filled with a subsample of the water. This was irradiated with a 1 kW Hg-Xe lamp at a specific ultraviolet wavelength (5 nm bandpass) for a precisely measured interval of time. After homogenizing the water sample, a 40.0 mL sample was collected in a glass syringe, and a CO determination was performed following the same procedure

outlined for the sea surface [CO] measurements above. The data are presented in Appendix C.

For a given wavelength, the rate of CO generation had to be normalized to the light absorbed in the cell to obtain a measure of the quantum yield. The amount of energy entering the irradiation cell was determined by ferrioxalate actinometry (Hatchard and Parker (1956)). The fraction of incident power absorbed by the water sample in the irradiation tube was calculated using the attenuation coefficient of the sample. This was calculated as the sum of the CDOM absorption coefficient of the 0.2μm filtered seawater sample (from Cape Henlopen or BATS) and the attenuation/backscattering coefficients of the clearest natural waters from Smith and Baker (1981). The CDOM absorbance was measured with a laboratory spectrophotometer using distilled milli-Q water as a reference. Following the suggestion of Green and Blough (1994), the mean optical density of the samples between 700–800 nm was subtracted from the optical densities across the measured wavelength range. This provided a means of removing the scattering effects of small particles that passed through the filters.

Knowing the actual attenuation coefficient, the amount of light absorbed by the seawater sample could be deduced using a Beer-Lambert calculation. The fraction of this light absorbed by CDOM was calculated as the ratio of CDOM absorption to total absorption for that wavelength. Next, the amount of power of a given wavelength absorbed by the CDOM of the sample was converted to the rate of photon absorption using the Planck relation. Finally the rate of CO generation of the water was normalized by the rate of photon absorption by CDOM to find the apparent quantum yield spectra shown in Figure 3-3. The results show that the efficiency of CO production increases logarithmically as wavelength decreases. Lines have been fitted to data sets on the implicit assumption that the log-linear relationship between apparent quantum yield and wavelength may be extrapolated to wavelengths where CO production can not be effectively measured in irradiation experiments (280–405 nm for Cape Henlopen seawater and 297–365 for BATS seawater) and where CDOM absorbance can not be effectively measured (280–525 nm for Cape Henlopen seawater

and 280–326 for BATS seawater).

For open ocean seawater samples such as at BATS, there was difficulty in calculating apparent quantum yields because the CDOM absorption was lower than the detection limits of the spectrophotometer except at the shortest wavelengths. The CDOM absorption of filtered seawater samples from BATS and Cape Henlopen are shown in Figure 3-4 for comparison. (These have been corrected for scattering effects following Green and Blough (1994)). The horizontal dashed line across the diagram corresponds to 0.002 optical depths, the detection limit of the laboratory spectrophotometer. The CDOM absorption for BATS water falls below the instrument detection limit above 326 nm, while that for Cape Henlopen water falls below the detection limit above about 525 nm. Measured absorbances can thus be effectively used to calculate apparent quantum yields only for the Cape Henlopen water.

For BATS water, the modelled CDOM absorption coefficient was calculated from the observation that the logarithm of the measured absorption coefficient varies approximately linearly with wavelength between 280 nm and the instrument detection limit. This log-linear relationship may expressed by:

$$a_{CDOM}(\lambda) = a_{CDOM}(\mathrm{r}) \exp(\mathrm{S_{CDOM}}(\lambda - \mathrm{r})) \tag{3.2}$$

where r is the reference wavelength, and $\mathrm{S_{CDOM}}$ is slope of the natural logarithm of CDOM absorbance versus wavelength between 280 nm and the wavelength of the detection limit of the instrument (Green and Blough (1994)). Calculating $\mathrm{S_{CDOM}}$ for the wavelength range 280–326 nm, CDOM absorptions were estimated by extrapolation for BATS seawater in the irradiation range 285–365 nm (the wavelength range for the irradiation experiments). Apparent quantum yields were calculated using these modelled CDOM absorptions, and these are shown in Figure 3-3 (labelled "modelled absorption") and may be subject to some error given the tenuous nature of the assumptions made. The calculation was repeated for BATS seawater for values of measured absorption (which do not vanish at wavelengths greater than 326 nm), and these are also shown in this figure (labelled as "measured absorption").

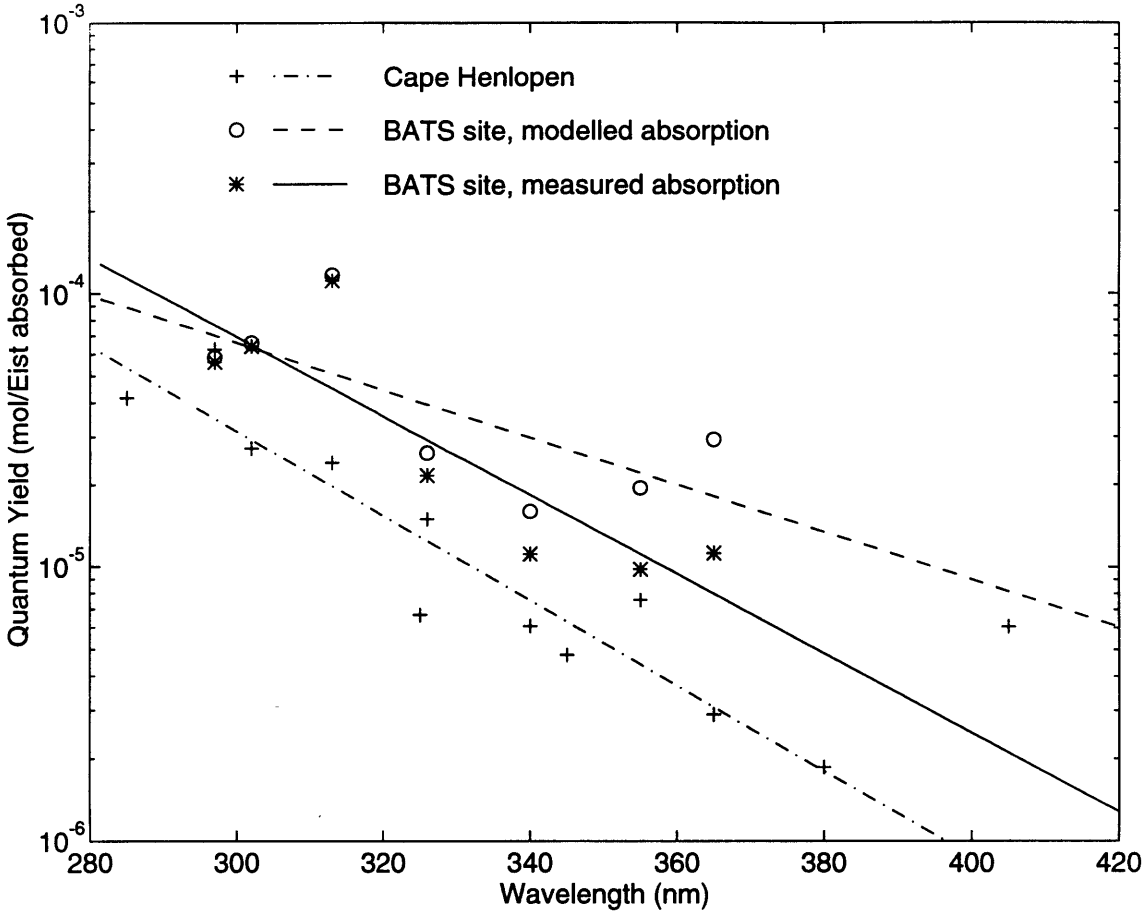

Figure 3-3: Apparent quantum yield for the water samples from the two locations analyzed in this investigation. The apparent quantum yield for the Cape Henlopen water sample was based on the laboratory measurement of CDOM absorption. Two apparent quantum yield results were calculated for BATS seawater; one based on a laboratory measurement of CDOM absorption (while the measured CDOM absorbance falls below the instrument detection limit at wavelengths greater than 326 nm the absorbance itself does not vanish but only deviates from log-linearity; it can be used to calculate apparent quantum yields at wavelengths up to 380 nm) and one based on a linear extrapolation of the logarithm of the absorption results in the wavelength range 280–326 nm. (These absorbances are given in Figure 3-4 below.) Lines of best fit to the data are also shown with the dot-dashed line fitting the Cape Henlopen data, the solid line fitting the BATS data calculated using the measured absorption, and the dashed line fitting the BATS data calculated using modelled absorption. These three lines represent models where the apparent quantum yield is assumed to decrease log-linearly with increasing wavelength across all wavelength ranges. The trend in apparent quantum yields is assumed to exist beyond both the wavelengths at which CO could be effectively measured in the irradiation experiments and the wavelengths where CDOM absorbance could be effectively measured.

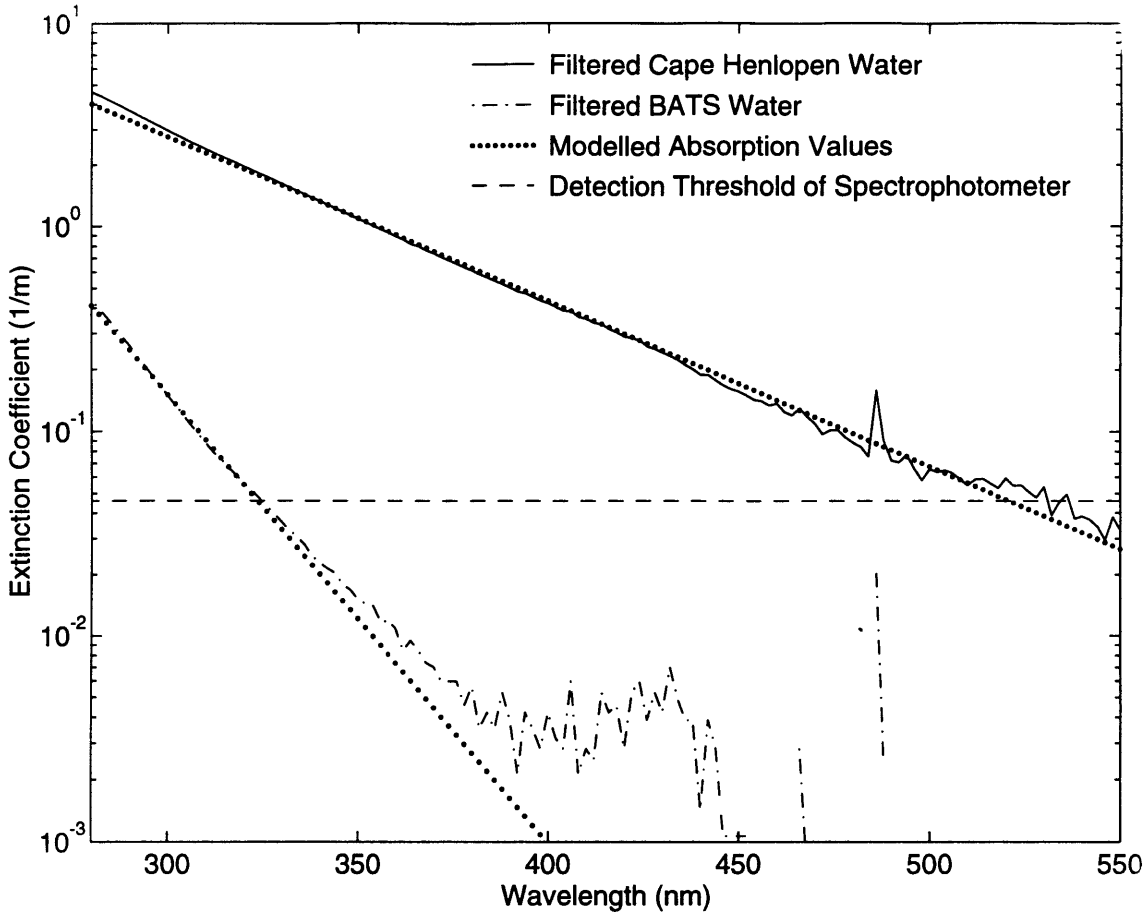

Figure 3-4: CDOM aborption for BATS and Cape Henlopen water. Measured absorption for the Cape Henlopen and BATS water is given by the solid line ans dot-dashed line, respectively. The detection limit of the laboratory spectrophotometer is given by the horizontal dashed line at 0.04 m^{-1} (the instrument detection limit of 0.002 optical depths (Green and Blough (1994)) divided by the 5 cm length of the sample cell). Dotted lines denote the lines of best fit to the data between 280 nm and the wavelength at which the data falls below the detection limit of the instrument. For the Cape Henlopen sample there was good agreement between the measured absorption and the line of best fit in the wavelength range 285–405 nm where the water samples were irradiated (the apparent quantum yield was calculated using measured absorption of the water). For the BATS sample there is good agreement between the measured absorption and the line of best in the range 280–325 nm, fair agreement in the range 325–380 nm, and poor agreement from 380–550 nm where the measured absorption is far below the detection limit of the instrument. BATS seawater samples were irradiated in the wavelength range 297–365 nm so that the extreme deviations between measured and modelled absorption above 380 nm were not significant in the calculation of apparent quantum yield. Both the measured and modelled absorptions were used in calculating the apparent quantum yield of BATS seawater. The deviation between the modelled and measured absorptions at wavelengths greater than 325 nm leads to a deviation in the apparent quantum yields, and these may be seen in Figure 3-3.

Table 3.2: Effect of uncertainty in optical density detection threshold on the line of best fit to the measured absorbance data. The lines of best fit in Figure 3-4 were based on data that were in the range 280 nm and the wavelength where optical density of the sample fell below 0.002 optical depths, the assumed detection threshold of the laboratory spectrophotometer. This table varies the assumed detection limit of the instrument from 0.007 to 0.0007 optical depths and tabulates the calculated the slope and y-intercept of the lines of best fit based on the increased number of data over a greater of wavelength range. The results show that the slopes do not vary much and that the assumption that the CDOM absorption varies exponentially at wavelengths greater than 280 nm is valid for assumed instrument detection limits as low as 0.0007 optical depths.

Seawater Sample	Optical Density Threshold for Spectro-photometer	Slope S_{CDOM} (nm^{-1})	Error in Slope S_{CDOM} (nm^{-1})	y-inter-cept	Error y-inter-cept
Cape Henlopen	0.007	-0.01930	0.00005	6.87	0.02
Cape Henlopen	0.002	-0.0186	0.0001	6.59	0.05
Cape Henlopen	0.0007	-0.0182	0.0001	6.45	0.05
BATS	0.007	-0.0566	0.0002	15.07	0.05
BATS	0.002	-0.0504	0.0007	13.2	0.2
BATS	0.0007	-0.0467	0.0005	12.1	0.2

This calculated value of S_{CDOM} is robust with respect to the assumed detection limits of the instrument. This is illustrated in Table 3.2 which presents different calculated values of S_{CDOM} for both BATS and Cape Henlopen seawater for different assumed instrument detection limits.

3.2.2 Comparison of Quantum Yield Results with Published Data

The only set of quantum yield spectra that have been generated before this study were published by Valentine and Zepp (1993) for a set of swamp, river, and estuarine water samples. In general, their results are within a factor of 2–3 of values obtained in this experiment and lead to similar values for wavelength-integrated CO production when applied to modelled light fields (described in Chapter 4). On the basis of only

three determinations of apparent quantum yield for natural waters, it is not possible to state that the quantum yields for all waters should be the same. However, it seems reasonable that the quantum yields determined in this experiment should agree with each other and with the published result to within an order of magnitude. With respect to surface production, values inferred from this study are roughly two orders of magnitude lower than what has been measured by Mopper et al (1991).

The apparent quantum yields of Valentine and Zepp (1993) are shown in Figure 3-5 for four different natural water samples. They span the wavelength range 250–650 nm and are subject to considerable scatter at wavelengths longer than 500 nm. To calculate the associated wavelength-integrated CO production rate, the quantum yield data were fitted with two models describing the dominant trend of the data. (The two models are arbitrary but do allow an analysis of the sensitivity of spectral distribution of CO generation to subtleties in the quantum yield parameterization.) These two models were two straight lines fitting the data above and below a calculated intersection point of 362 nm, model 1, and a parabola of best fit, model 2.

The experimentally determined quantum yields of this investigation have also been modelled with straight lines of best fit. The ultimate purpose of these different line parameterizations is to explore the effect that different quantum yield parameterizations have on the spectral distribution of CO production and on wavelength-integrated CO production. For this purpose, the line representing the apparent quantum yields of the Cape Henlopen water in the range 285–405 nm was identified as model (3). The line representing the apparent quantum yield of BATS seawater calculated using the measured absorbance of the Sargasso seawater sample was identified as model (4). The line representing the apparent quantum yield of BATS seawater calculated using the modelled absorbance described above has been identified as model (5). The slopes and y-intercepts of these last three models correspond to the equations for the lines of best fit given in Figure 3-3. A summary of the mean square deviations (σ^2) associated with fitting the various data sets with different line parameterizations is given in Table 3.3.

The five models are compared in terms of the spectral distribution of surface CO

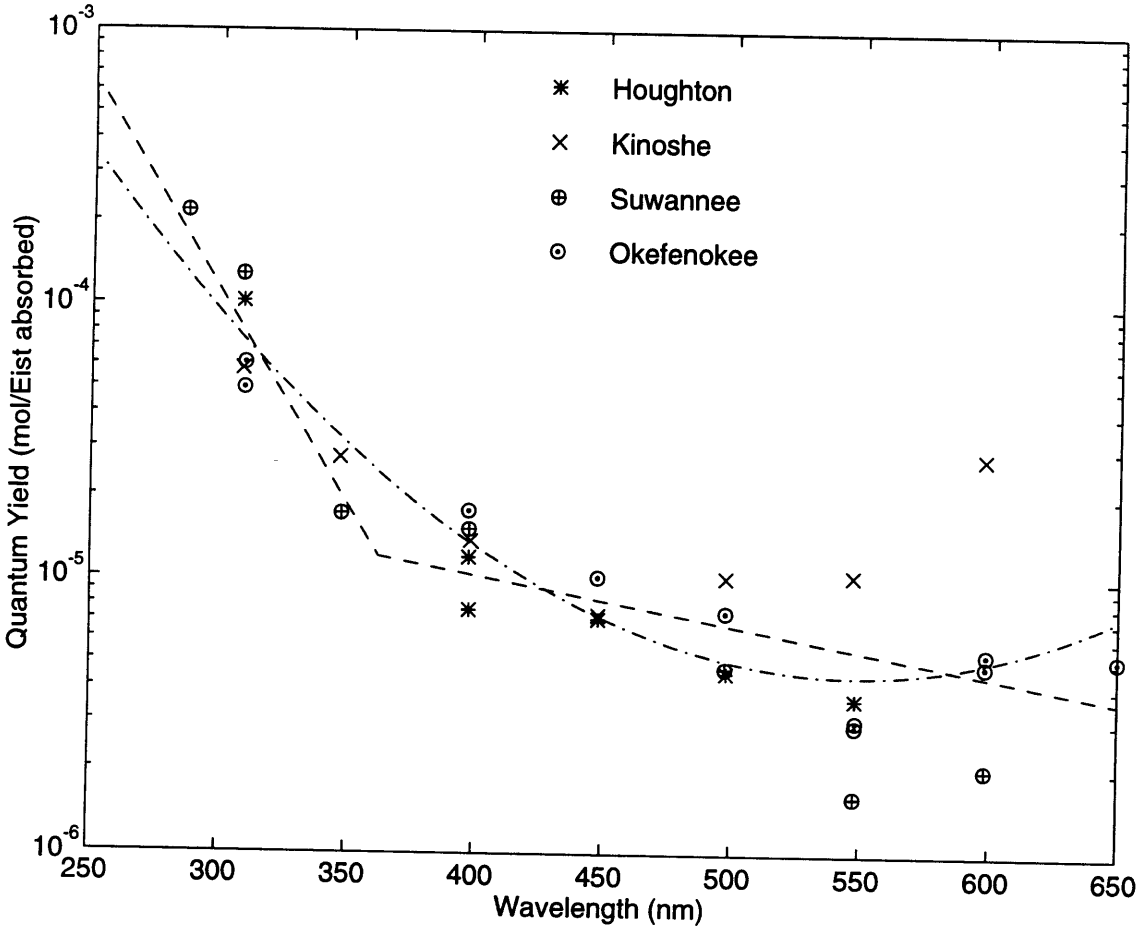

Figure 3-5: Apparent quantum yields from Valentine and Zepp (1993) with lines of best fit. The dot-dashed line is the parabola of best fit to the data set. The two dashed lines represent lines of best fit to the data in the range 285–350 nm and from 350–650 nm. The different point symbols represent the sources of the the water on which Valentine and Zepp (1993) conducted their quantum yield analysis.

Table 3.3: Models used to fit the different apparent quantum yield data sets with estimated uncertainties. The coefficients for the lines of best fit have been calculated for the natural logarithm of the apparent quantum yield versus wavelength. Similarly, the mean square deviation between modelled and computed values, σ^2, has been calculated for the natural logarithm of the apparent quantum yields. Model 1 corresponds to the Valentine and Zepp (1993) data fitted to two straight lines intersecting at 362 nm. Model 2 represents the the same data fitted to a parabola. Model 3 represents the apparent quantum yield for the Cape Henlopen water fitted with a straight line. Model 4 represents the apparent quantum yield for Sargasso Sea water calculated using measured absorbance. Model 5 represents the apparent quantum yield for Sargasso Sea water calculated using modelled absorbance. (see Figure 3-3 for the apparent quantum yield data along with the lines of best fit)

Model	Coeff of λ^2 (nm^{-1})	Coeff of λ (nm^{-1})	Error in Coeff of λ (nm^{-1})	Const	Error in Const	σ^2
1 (< 350 nm)	-	-0.036	0.007	1.6	2.1	125.1
1 (> 350 nm)	-	-0.0042	0.0018	-9.8	0.9	
2	$4.91 * 10^{-5}$	-0.0539	-	2.45	-	129.7
3	-	-0.036	0.004	0.3	1.4	133.3
4	-	-0.033	0.008	0.4	2.7	111.5
5	-	-0.020	0.009	-3.6	2.8	104.2

production at solar noon on Julian day 79 (March 21) (see Figure 3-6). This was done using light fields generated by the model of Baker et al (1980) described in Section 4.2. This model produced a theoretical spectral distribution of solar irradiance at sea level for 31° 50′ N latitude assuming no cloud cover. Interestingly, the spectral shapes of the five CO production curves are approximately the same for the different quantum yield models considered and differ mainly in amplitude.

One important difference between the five models is the depth and wavelength integrated CO production as a function of time. The parameterization of the quantum yield does make a significant difference in the depth-integrated amount of CO produced at any given hour during the day because light penetration in the water column is a strong function of wavelength especially in the ultraviolet region where CO production occurs. The peak integrated production at solar noon for each of the models is given in Table 3.4 and varies from 955 nmol h^{-1} m^{-2} for the Cape Henlopen quantum yield results to 4511 nmol h^{-1} m^{-2} for the data of Valentine and Zepp (1993) fit with a parabola.

For comparison, a table of CO surface production values published in the literature has been assembled and is given in Table 3.5. The published production values in this table show wide variation depending on the site from which the samples are drawn, and the lowest production differs from the highest production by two orders of magnitude. The calculated production rates obtained in this study are about the same as those calculated in an unpublished study of quantum yields for the Pacific Ocean by Oliver Zafiriou but are two orders of magnitude lower than production values for the Sargasso Sea given in Table 3.5 (none of these numbers has been normalized to insolation). This large discrepancy is not resolved in terms of the methods used to deduce the production rate. In this regard, Mopper et al (1991) expose quartz tubes of seawater to sunlight over a 4 h period near solar noon at 24°N (unspecified time of year) and measure [CO] at the beginning and end of this irradiation. The method of our investigation exposes a slab of water 0.5 m thick to a theoretical solar spectrum at noon for 31° N on March 21 (not corrected for cloud cover or measured insolation). There are differences in irradiation geometry and the amount of insolation, but it

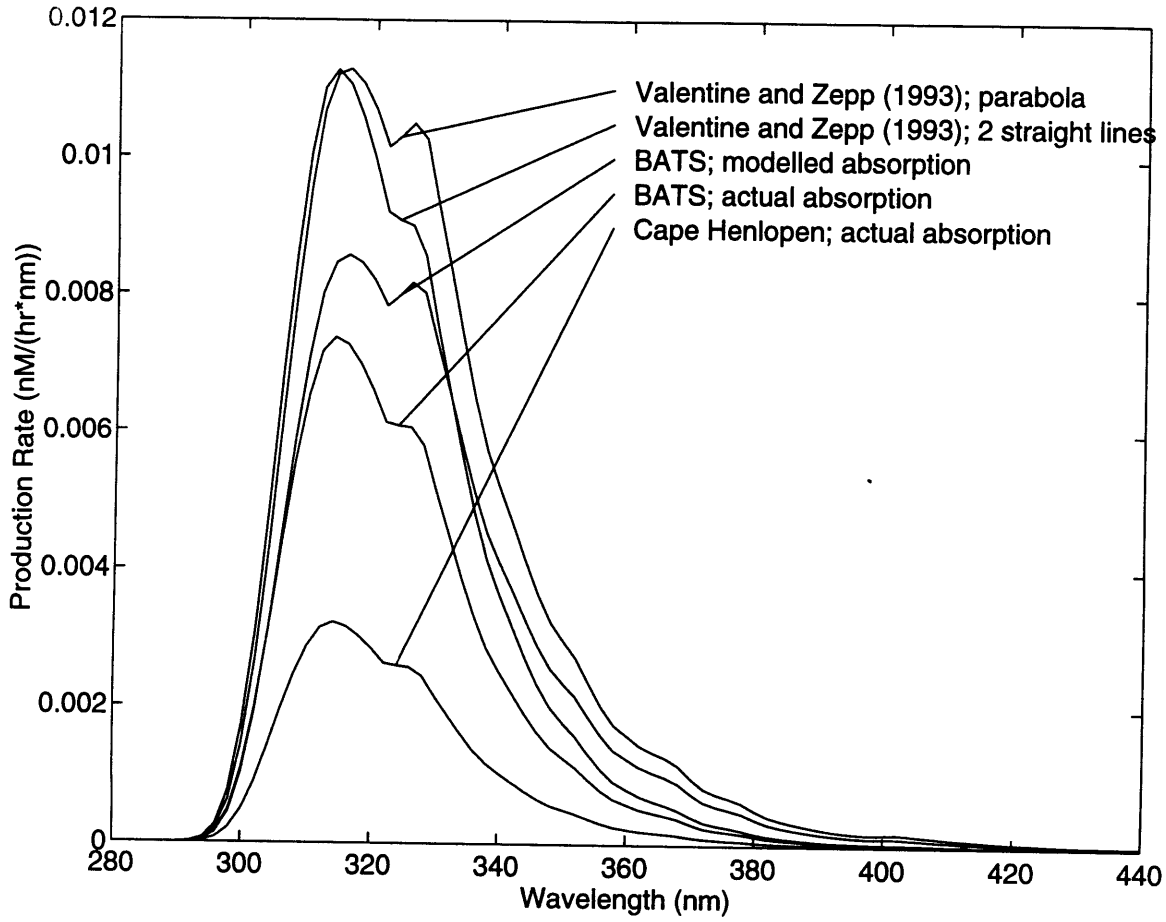

Figure 3-6: Spectral shape of CO surface (i.e. in the 0–0.5 m depth interval) production curves at solar noon on March 21 for the five cases of apparent quantum yield described in the text (identified as five models but consisting of three independent data sets). The quantum yields have been identified in Table 3.3. The light field has been generated using the light model of Baker et al (1980) (described below) for 31° 50′ N latitude, and it assumes clear skies with no measured insolation correction. Because the light field is the same in each case, the differences in spectral shape of the production curves are due specifically to the different quantum yield models. For instance, the quantum yield of the Cape Henlopen samples was about half that of the BATS samples calculated using the actual CDOM absorption of the water. Hence, the production rate calculated using Cape Henlopen quantum yields with CDOM absorption for the Sargasso Sea is predicted to be half that using BATS quantum yields (based upon modelled absorption) with the same Sargasso Sea CDOM absorption. For the purpose of the numerical modelling study performed below, the quantum yield used was that for BATS using the modelled absorption (model 5).

Table 3.4: Comparison of depth-integrated production and surface production of CO at solar noon for the five parameterizations of quantum yield. The surface production is the mean production in the uppermost 0.5 m of the water column, and the depth integrated production has been calculated to 50 m. Note that over 99% of the production for all 5 models occurs in the first 50 m of the water column. Model 5 was used for the calculation of light production in the numerical simulations described in Section 5.

Model	Description	Surface Production ($\triangle z = 0.5$m) (nMh^{-1})	Depth Integrated Production (0–50m) ($nmolh^{-1}m^{-2}$)
1	Valentine and Zepp (1993) 2 straight lines	0.364	3398
2	Valentine and Zepp (1993) parabola	0.429	4511
3	Cape Henlopen water	0.104	955
4	Sargasso Sea water measured CDOM absorption	0.243	2279
5	Sargasso Sea water modelled CDOM absorption	0.330	3470

seems difficult to believe that these could explain a deviation of more than one order of magnitude. The results of this experiment are also supported by the results of the numerical simulation described in Section 5 (where the quantum yields determined by laboratory experiment are sufficient to generate a modelled sea surface [CO] similar to what is actually observed). Further work is needed to resolve the discrepancy with Mopper et al (1991).

Table 3.5: Assembled literature values for CO production in natural waters and prepared solutions. These values have been taken from the original references without correction for the different intensities of light used to generate CO. It varies between 650–1000 W m^{-2} between references

Location	Source	Production ($nM\ h^{-1}$)
Kinoshe Lake	[41]	260
Houghton Marsh	[41]	1330
Okefenokee Swamp	[41]	1200
Suwannee River	[41]	1500
Intracoastal Waterway	[41]	110
Live Oak	[41]	90
Oyster River fulvic	[41]	3200
Houghton Marsh	[41]	480
Houghton Marsh	[41]	120
Suwannee River	[41]	490
Suwannee River	[41]	41
soil fulvic	[41]	3330
Contech fulvic	[41]	1600
Fluka humic	[41]	1500
Sargasso Sea, 1-20 m	[25]	18.6 ± 2.7
Sargasso Sea, 20-150 m	[25]	9.6 ± 0.8
Sargasso Sea, 500-4000 m	[25]	16.1 ± 2.2
Station B, Spring, Caribbean Sea	[17]	18.5
Station F, Spring, Caribbean Sea	[17]	18.5
Station P5, Spring, Gulf of Paria	[17]	32.5
Station P3, Spring, Gulf of Paria	[17]	36.6
Station R9, Spring, Gulf of Paria	[17]	29.0
Station R5, Spring, Orinoco Delta	[17]	19.1
Station R3, Spring, Orinoco Delta	[17]	23.7
Station R1, Spring, Orinoco Delta	[17]	43.5
Station A, Fall, Caribbean Sea	[17]	22.8
Station G, Fall, Caribbean Sea	[17]	25.5
Station R5, Fall, Orinoco Delta	[17]	63.6
Station R4, Fall, Orinoco Delta	[17]	76.8
Station R3, Fall, Orinoco Delta	[17]	88.3
Station R2, Fall, Orinoco Delta	[17]	28.1
Station R1, Fall, Orinoco Delta	[17]	22.9

Chapter 4

CO Production Model

4.1 Introduction

One of the primary purposes of this investigation is to parameterize the depth dependent production of CO in the water column. CO is produced in response to the light absorbed by CDOM in seawater, and during this investigation measurements were made of insolation at one minute intervals and underwater irradiance at three times on March 20, 21, and 22. These measurements permit the calculation of surface irradiance and the light attenuation properties of seawater as a function of wavelength. Also, laboratory measurements were made of CDOM absorbance and the apparent quantum yield of CO production. These permit a calculation of the light absorption by CDOM in the water column and the rate at which CO is produced at depth. The only parameters missing from this scheme are a method to deduce the spectral distribution of irradiance from the pyranometer measurements of insolation and a method to find the amount of solar energy lost by reflection from the sea surface. This chapter links together a series of models that integrate theoretical predictions of these unknowns with the measured quantities. This gives insight into the light fields and CO production rates at various depths in the euphotic zone during the experimental investigation.

There is no existing model that predicts CO production in the water column as a function of depth, wavelength, time of day, etc. Part of the reason for this is that

the problem is that previous studies have focussed only on specific aspects of the problem, the marine photochemistry, the marine light field, the albedo, atmospheric ozone attenuation, etc. somewhat independently of each other.

In creating a CO production model for this study, one of the more important objectives has been to link together the different light models to predict the light field in the ocean ultimately as a function of the solar spectrum outside the atmosphere. Fortunately, the models can all be linked in sequence, so that the output from one model can be put into the next model and so on. Two previous studies have attemped this type of linkage to investigate marine chemistry: Musgrave et al (1988), who were in interested in the O_2 photoproduction cycle, and Sikorski and Zika (1993a) who were interested in the H_2O_2 production cycle.

For this investigation, four submodels are used. The first takes the solar irradiance outside the atmosphere and predicts the solar irradiance at the ocean surface. This model is essentially the same as that of Baker et al (1980) except that published spectral irradiance outside the atmosphere was used in place of a modified blackbody model. The second model corrects this irradiance for the effect of cloud cover by comparison with measured insolation from the ship. The next model predicts the albedo and predicts the irradiance just below the sea surface from the irradiance just above. This uses partly the data presented by Preisendorfer and Mobley (1986) and partly the parameterization developed by Sikorski and Zika (1993a). The fourth model attempts to predict the diffuse attenuation coefficient of the water and thus predict the irradiance field in the water column as a function of depth, of solar zenith angle, and of the inherent absorption properties of the water. This model is built on work by Vodacek et al (1994) but ignores absorption by chlorophyll and suspended mineral matter. Each of these four models will be outlined in the sections presented below.

4.2 Attenuation by the Atmosphere

This section presents a model which starts from an irradiance field outside the atmosphere and describes the atmospheric attenuation effects leading to the spectral distribution of irradiance at the sea surface. The motivation for this is to predict the theoretical spectral irradiance at sea level as a function of time. This is normalized by the measured insolation, integrated over the wavelength range, 300–3000 nm, and propagated into the water column to find the underwater light field as a function of time, depth, and wavelength. The wavelength dependence is important because CO production depends on the intensity of radiation in the UV-B region below 350 nm. This varies according to the apparent thickness of ozone through which direct sunlight has to pass and thus depends on zenith angle which itself varies as a function of time of day and time of year. There are several empirical models which can predict ozone absorption effects. The one which this investigation uses was published by Baker et al (1980). The actual parameterization for the model was performed by Green et al (1980), and Baker et al (1980) recalculated the equations of the model based on irradiance data collected during a research cruise across the Pacific Ocean. The equations and constants are tabulated in Appendix D. The main reason for using such a complicated light model is that it predicts the changing proportion of CO-producing radiation in the course of a day. Additionally, it creates a general result that can be applied anywhere in the world with an estimated loss of accuracy of only 5% of what could be obtained by intensive spectral measurements (Green et al (1980)).

The Green et al (1980) model essentially takes the light field outside the atmosphere and applies a series of attenuation effects using the Beer-Lambert law with corrections for the earth's curvature and the zenith angle.

The light field outside the atmosphere used in this investigation was published by Kondratyev (1969). His tabulated data gives irradiance in 5 nm intervals for the wavelength range 225–600 nm, in 10 nm intervals for 600–1100 nm and in 100 nm intervals for the wavelength range 1100–4500 nm. When integrated across the entire wavelength range, the solar constant is calculated to be $1390 \mathrm{Wm}^{-2}$. In using this

data for a light field to estimate CO production, this published data was linearly interpolated to 2 nm intervals for the CO production range 260–550 nm.

The light model of Green et al (1980) first divides the net irradiance into a diffuse portion that can be ascribed to all portions of the sky and a direct or specular portion that can be ascribed directly to the sun. This is described by the following equation:

$$G(\lambda,\theta) = D(\lambda,\theta) + S(\lambda,\theta) \tag{4.1}$$

where θ is the zenith angle, $G(\lambda,\theta)$ is the theoretical irradiance at the sea surface, $D(\lambda,\theta)$ is the direct solar part of the spectrum, and $S(\lambda,\theta)$ is the diffuse skylight part of the spectrum.

Each of these components is attenuated in the atmosphere by four absorbers or scatterers. These are Rayleigh scatter, particulate scatter, ozone absorption, and particulate absorption. Each of these elements attenuates light according to the Beer-Lambert law, and each has a characteristic attenuation coefficient. For the case of particulate scatter and absorption, the attenuation coefficient is a constant. For Rayleigh scatter and ozone absorption, the attenuation coefficient has a wavelength dependence. For ozone absorption, in particular, absorption increases exponentially with decreasing wavelength leading to a sharp cutoff in irradiance below 300 nm.

The direct solar portion of irradiance has a zenith angle dependence; the magnitude of the atmospheric attenuation coefficient is approximately inversely proportional to the cosine of the zenith angle (the angle between the zenith and the sun's disk). There is a small correction to this directional cosine for the curvature of the earth's atmosphere. The directional cosine allows for more attenuation of light to occur when the sun is shining obliquely through the atmosphere near sunrise or sunset.

The diffuse skylight portion of the spectrum is not characterized by a strongly directional light source and consequently does not have a zenith angle dependence.

For this study, the net result of this theory is an estimation of the wavelength and time dependence of solar irradiance at sea level at BATS for clear sky conditions. This result is shown in Figure 4-1 for the specific case of Julian day 79 (March 21) for

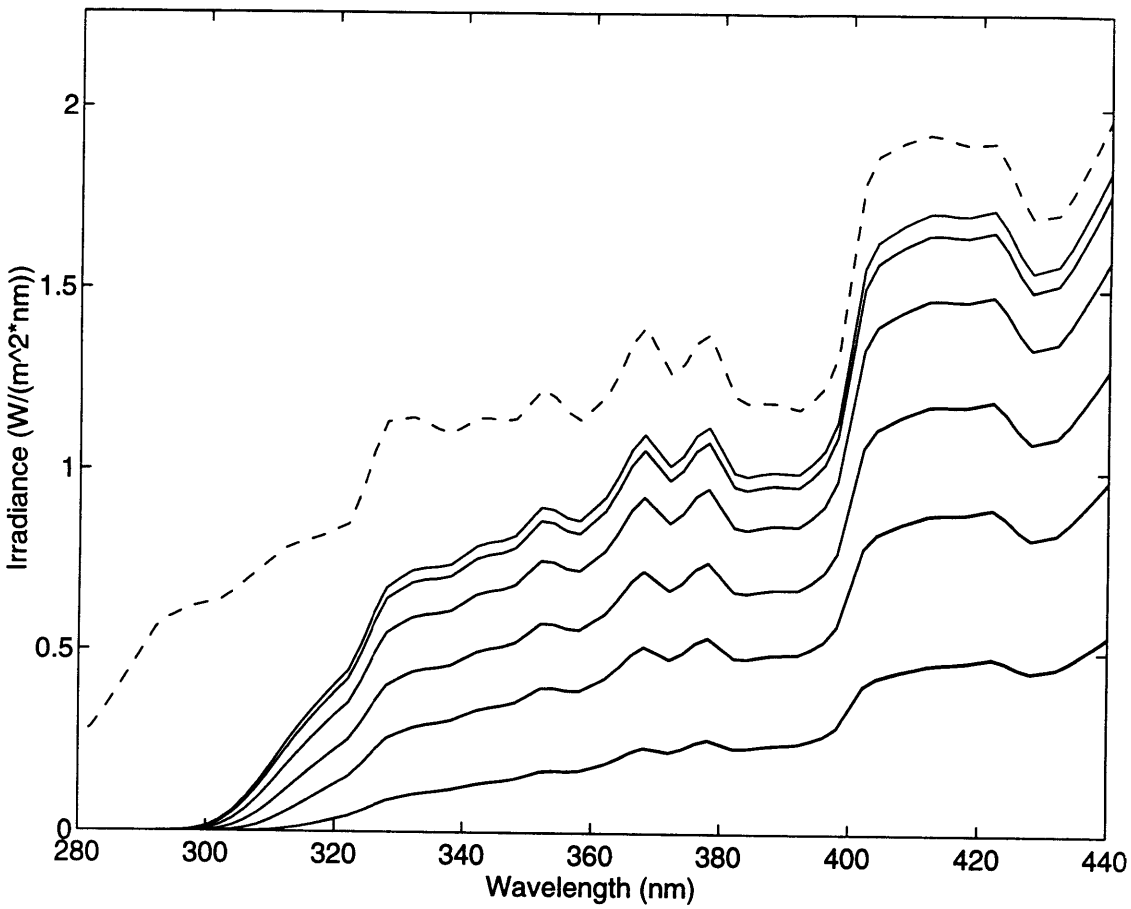

Figure 4-1: Modelled wavelength distribution of irradiance for different times of day. The uppermost dashed curve represents the irradiance outside of the atmosphere as reported by Kondratyev(1969). The first solid curve below this is the calculated irradiance at sea level at 31°N latitude at solar noon on March 21 assuming a cloudless sky and no measured insolation correction. Successive curves below this represent sea level irradiance at one, two, three, etc. hours past local solar noon.

the wavelength range 280–450 nm at successively longer times after solar noon. The irradiance outside of the atmosphere is shown as the uppermost curve to illustrate the attenuation effects of the atmosphere.

4.3 Attenuation by Clouds

Having obtained a theoretical light field at the sea surface the next step is to predict the effect of clouds. With respect to CO production, cloud cover acts as a reflector for shortwave light (in the range 280–3000 nm) so that the total insolation reaching the

earth's surface is decreased. For the current investigation, cloud cover approached 75% during March 15–25, and CO production would have been significantly affected.

Clouds form a complicated area of research, and there are few models which can parameterize the effect of clouds on sky irradiance. The issue has been addressed by ground and satellite based studies, but the basic problem seems to be how to parameterize a cloud. There are no light models which can translate cloud cover into a certain attenuation of energy with great accuracy. In this respect, Sikorski and Zika (1993a) did not have to address the issue and modelled only cloud-free or nearly cloud-free days.

A solution to the problem was found by comparing the theoretical clear sky insolation as determined from List (1984) with the insolation record measured by the pyranometer during the investigation. (The theoretical insolation value could not be generated by integrating the theoretical spectral irradiance model of Baker et al (1980) because this model was calibrated only for the wavelength range 280-380 nm, much shorter than the 280-3000 nm range of the solar spectrum.) The normalization of spectral irradiance at the sea surface by measured insolation is expressed by the following equation:

$$\mathrm{D}(\theta,\lambda,\mathrm{o}+) = \frac{I}{I_{theor}}\mathrm{D}(\theta,\lambda) \tag{4.2}$$

$$\mathrm{S}(\theta,\lambda,\mathrm{o}+) = \frac{I}{I_{theor}}\mathrm{S}(\theta,\lambda) \tag{4.3}$$

$$I_{theor} = \frac{I_{space}}{0.9955^2}\alpha_{sky}^{\sec(\theta)}\cos(\theta) \tag{4.4}$$

where $\mathrm{S}(\theta,\lambda,\mathrm{o}+)$ is the direct solar spectral irradiance just above the sea surface, $\mathrm{D}(\theta,\lambda,\mathrm{o}+)$ is the diffuse irradiance just above the sea surface, I is measured insolation, I_{theor} is theoretical insolation just above the earth's surface in the absence of cloud cover, I_{space} is the solar constant outside the atmosphere (1390 W m^{-2}), α_{sky} is the clear sky transmittance. The clear sky transmittance was chosen to be 0.8, the same as that chosen by Price et al (1987).

This solution took into account the attenuating effects of the clouds but not the change in ratio between the diffuse skylight and direct solar parts of the irradiance spectrum or the spectral distribution of energy. There are implications for this in determining the energy responsible for CO production and also in determining the amount of light penetration into the water; these have been ignored.

The five LICOR spectra collected during the March 21-23, 1993 investigation period provided an opportunity to assess the effectiveness of the light model in predicting the spectral irradiance at the sea surface. Figure 4-2 shows the five LICOR spectra along with the corresponding predictions made by the model. This model is essentially that of Baker et al (1980) with corrections made for cloud attenuation effects based on the theoretical insolation predicted by List (1984). There is good qualitative agreement between the modelled and measured values except for case (d) where the model underpredicts the LICOR measurements. This may have been due to a rapid fluctuation in the cloud cover during the time of the LICOR measurement which created a bias in the measured insolation record (whose 10 minute average value was used to calibrate the model predictions for cloud attenuation effects).

4.4 Albedo of the Sea Surface

The amount of light actually entering the water must next be corrected for reflection losses from the sea surface (the albedo). The current investigation uses the parameterization of Sikorski and Zika (1993a) who calculate surface reflection losses for the diffuse skylight and direct solar components separately:

$$E(\theta,\lambda,o-) = S(\theta,\lambda,o+)(1.03 - \text{albedo}_{\text{diffuse}}) + D(\theta,\lambda,o+)(1.03 - \text{albedo}_{\text{Fresnel}}) \quad (4.5)$$

where $E(\theta,\lambda,o-)$ is the actual irradiance at the top of the water column just below the surface, $\text{albedo}_{\text{Fresnel}}$ is the albedo of the sea surface for direct sunlight, and $\text{albedo}_{\text{diffuse}}$ is the albedo of the sea surface for diffuse skylight. The factor of 1.03

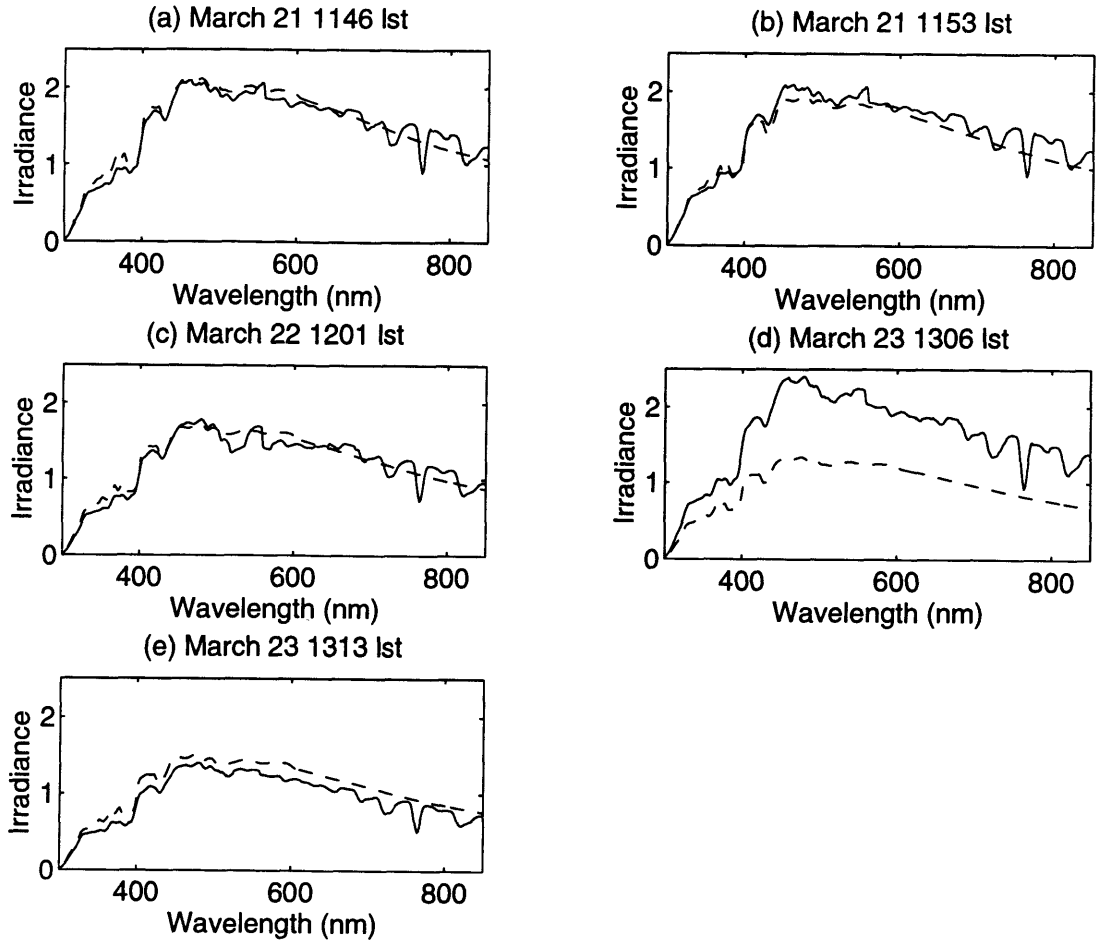

Figure 4-2: Comparison of LICOR measurements of surface spectra with model predictions corrected for cloud attenuation effects. There is good qualitative agreement between the modelled and measured values except for case (d) where the model underpredicts the LICOR measurements. This may have been due to a rapid fluctuation in the cloud cover during the time of the LICOR measurement which created a bias in the measured insolation record (whose 10 minute average value was used to calibrate the model predictions for cloud attenuation effects). The model predictions for spectral irradiance tend to be much smoother than LICOR measurements mainly because the LICOR measurements were recorded at a wavelength interval of 2 nm whereas the model predictions are based on irradiance data given for wavelength ranges of between 5 nm and 100 nm.

is meant to take into account the 3% downward reflection from the sea surface of upwelling irradiance into the water column.

Estimates of albedo or surface reflection are difficult to make with great accuracy. Qualitatively, it is known that albedo is a function of the zenith angle and the surface roughness. It is a minimum when the sun is directly overhead and reaches its maximum value when the sun is close to the horizon. Albedos tend to be lowered on a wind roughened sea surface where the mean sea surface slopes are increased. The current investigation estimates the Fresnel albedo by interpolating the data of Preisendorfer and Mobley (1986) recorded at zenith angle intervals of 5° and at wind speeds of 0, 1, 3, 5, 10, and 20 ms^{-1} (see Figure 4-3). This treatment assumes that the direction of propagation of the waves on the ocean surface is the same as the direction of a projection of the sun to the horizon. (This angle has a small effect and is ignored for this study.)

The $albedo_{diffuse}$ has been estimated from Sikorski and Zika (1993a) who make their own parameterization of based on glitter pattern data on the sea surface presented by Preisendorfer and Mobley (1986):
For diffuse irradiance,

$$albedo_{diffuse} = 0.050 + 0.018\left[(20 - U_{10})/20\right]^{1.5} \tag{4.6}$$

There is an implicit assumption in this treatment that there is no wavelength dependence.

4.5 Attenuation of Light in the Water Column

The last stage in the development of the optical model is to estimate the attenuating properties of the water column and thereby predict the light field at depth. One expects the intensity of the light field in water to be influenced by the thickness of overlying water, by the absorbing and scattering nature of the water, and by the directional nature of the light field itself.

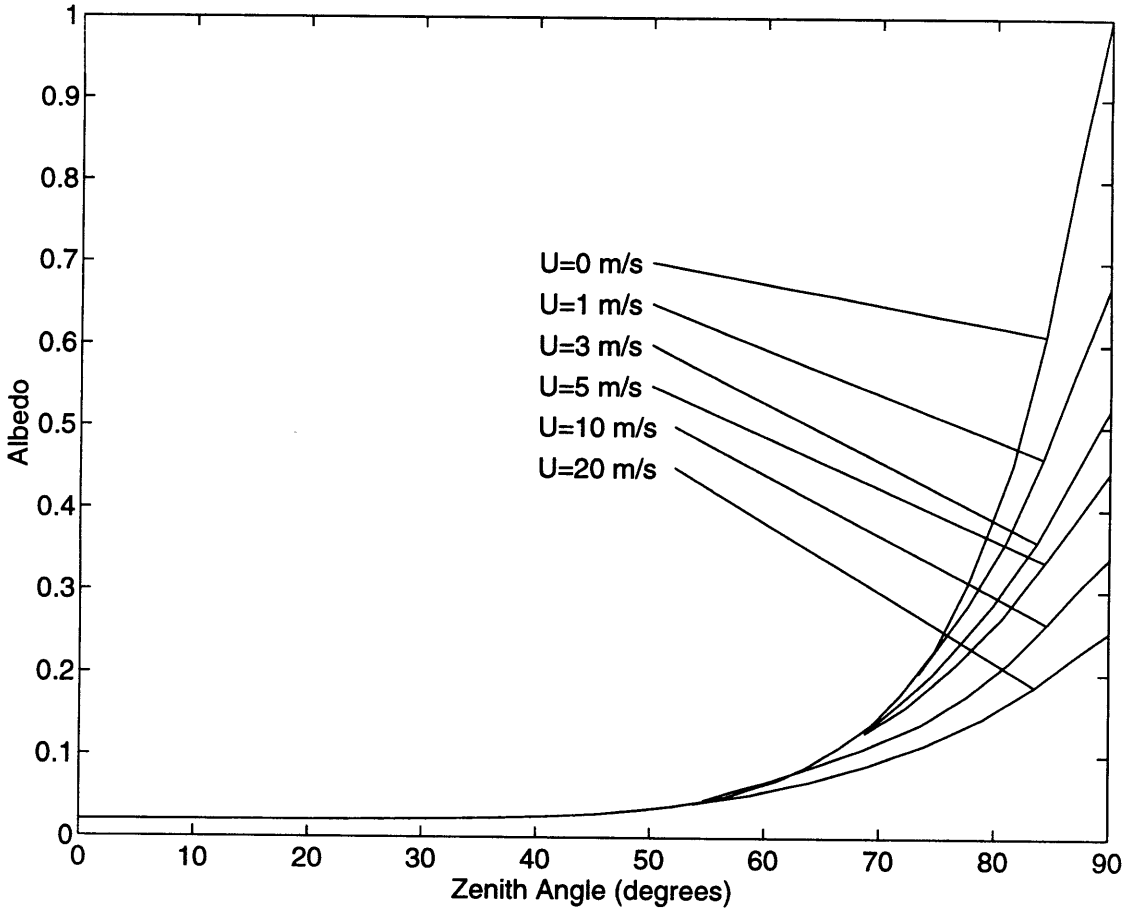

Figure 4-3: Fresnel albedo as a function of zenith angle and wind speed. This data has been recorded at 5° intervals from data presented by Preisendorfer and Mobley (1986).

A general theory for the attenuation of light is developed by Prieur and Sathyendranath (1986). Through a series of assumptions, these researchers conclude that the presence of the upwelling light field may be neglected and that light attenuation in the water column may be described by the Beer-Lambert law. This states that the decrease in irradiance across a thin layer of water of depth Δz for a given wavelength is proportional the irradiance at the top of the layer and to the attenuating properties of the water, i.e.

$$\frac{\mathrm{d}E_d(\lambda, z)}{\mathrm{d}z} = -K_d E_d(\lambda, z) \tag{4.7}$$

$$E_d(\lambda, 0\mathrm{m}) = \mathrm{E}(\theta, \lambda, \mathrm{o}-) \tag{4.8}$$

where K_d is the diffuse attenuation coefficient (assumed to have no depth dependence for this investigation) and E_d is the downwelling irradiance field. The diffuse attenuation coefficient, K_d, is given by the following equation:

$$K_d(\lambda) = \frac{c(\lambda)}{\bar{\mu}_d} \tag{4.9}$$

where $c(\lambda)$ is the inherent attenuation property of the water and $\bar{\mu}_d$ is the mean directional cosine of the light field in the water. This latter takes account of the fact that the mean penetration of light into the upper ocean will be less when the sun is close to the horizon than when it is overhead. As well, the value of the mean directional cosine will vary according to the ratio of diffuse skylight to direct solar irradiance; the directional cosine of diffuse irradiance is a constant value whereas that for direct solar irradiance depends on the zenith angle of refracted sunlight. The specific relation is given by Sikorski and Zika (1993a).

$$\frac{1}{\bar{\mu}_d} = \frac{\mathrm{D}(\lambda, \theta)}{\mathrm{G}(\lambda, \theta)}[\cos(\theta_w)]^{-1} + \frac{\mathrm{S}(\lambda, \theta)}{\mathrm{G}(\lambda, \theta)}[0.859]^{-1} \tag{4.10}$$

where θ_w is the zenith angle in the water (i.e. corrected for refraction of light into water) and G has already been defined in equation 4.1.

The problem of determining the light field at depth thus simplifies to one of finding a parameterization of the inherent attenuation coefficient of the water, $c(\lambda)$. Research in this subject has focussed on two possible solutions. The first of these has sought to find K_d by solution of equation 4.7 knowing the measured irradiance fields at depth. This approach was not taken for this investigation. Even though irradiance fields at depth were measured by the LICOR instrument on three of the ten days of the March study, there was poor agreement in the calculated K_d values between the three days. As well, limitations in the detection limits of the underwater spectrophotometer prevented calculation of K_d in the wavelength range 300–320 nm where the greatest CO production was taking place. The LICOR data sets were thus rejected for the model on the basis of low precision and inadequate wavelength range.

The second approach has been to reconstruct the observed diffuse attenuation of ocean water from the measured absorbance and scattering properties of its individual components. Vodacek et al (1994) have made a study of these individual attenuating components and have assessed that for a given wavelength $c(\lambda)$ can be expressed as the following sum:

$$c(\lambda) = a_w + a_{SM} + a_{ph} + a_{CDOM} + \frac{1}{2}b_w + b_{SM} + b_{ph} \tag{4.11}$$

where a and b denote the absorption and backscatter (respectively) coefficients of water (w), suspended mineral matter (SM), phytoplankton (ph), and coloured dissolved organic matter ($CDOM$). The coefficients for phytoplankton and suspended mineral matter are functions of the concentration of these materials and of the specific absorption or backscattering coefficients.

For this investigation, a simplified version of this equation was used:

$$c(\lambda) = a_w + a_{CDOM} + \frac{1}{2}b_w \tag{4.12}$$

Here, the absorption and backscattering coefficients of seawater were taken from values reported by Smith and Baker (1981). The absorption coefficient for CDOM was obtained by measurement of a 0.2μm filtered Sargasso seawater sample (collected

on September 24, 1993) on a laboratory spectrophotometer using filtered, distilled milli-Q water as a reference.

The other terms in equation 4.11 were not used because they were not measured. Fortunately, the study by Vodacek et al (1994) indicates that all the neglected attenuation terms were smaller than the absorption of water and CDOM over most of the wavelength range for station 25 km from the coast of Georgia. In this regard, Figures 4-4 and 4-5 show that the backscattering coefficients are about an order of magnitude lower than the absorption coefficients. As well, Figure 4-5 shows that water and CDOM are more important absorbers than phytoplankton or suspended mineral matter in the wavelength range 300–360 nm and 500–600 nm.

These assumptions are also valid for the BATS site. For instance, Gordon et al (1973) measure the total pigment concentration of the Sargasso Sea to be about 0.08 mg m^{-3} in a transect from Bermuda toward Cape Cod in June. This is lower than the value of 0.3 mg m^{-3} measured by Vodacek et al (1994) for station off the Georgia coast. No comparable estimates are available for suspended mineral matter but Dr. Neil Blough did suspect that its concentration would be lower at the BATS site than near the Georgia coast. The absorption of chlorophyll and suspended mineral matter is thus lower than the absorption due to pure water over all wavelengths and may be neglected for this investigation.

The e-folding depth of light penetration (the reciprocal of mean attenuation coefficient) used for the model is plotted with the corresponding e-folding depths calculated from the LICOR data in Figure 4-6. The modelled e-folding depth falls within the envelope of the measured e-folding depths except in the range 370–490 nm, where the modelled values predict the water to be more transparent than what is actually observed. This result can be explained by the absence of terms parameterizing the absorbance of light by chlorophyll and suspended mineral matter. However, it is not important for the purpose of penetration of CO production because most CO is produced at wavelengths shorter than 370 nm.

The low measured transparency in the range 370–490 nm of the Sargasso Sea water relative to the simple model construction may also be due to inappropriate

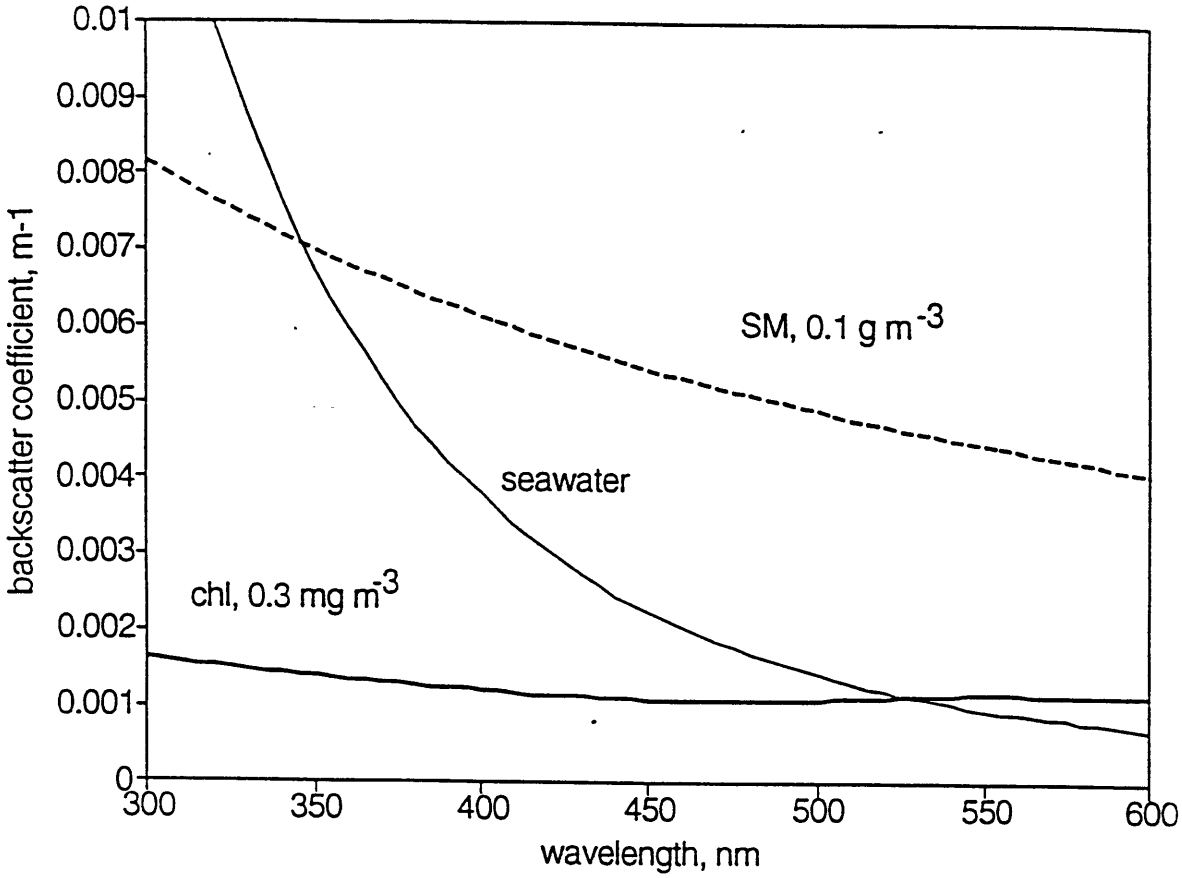

Figure 4-4: Spectral backscattering coefficients for suspended mineral matter (SM), seawater, and chlorophyll *a* (chl). The curves for suspended mineral matter and chlorophyll *a* are derived from specific backscattering curves that have been multiplied by concentrations given in the figure (Vodacek et al (1994))

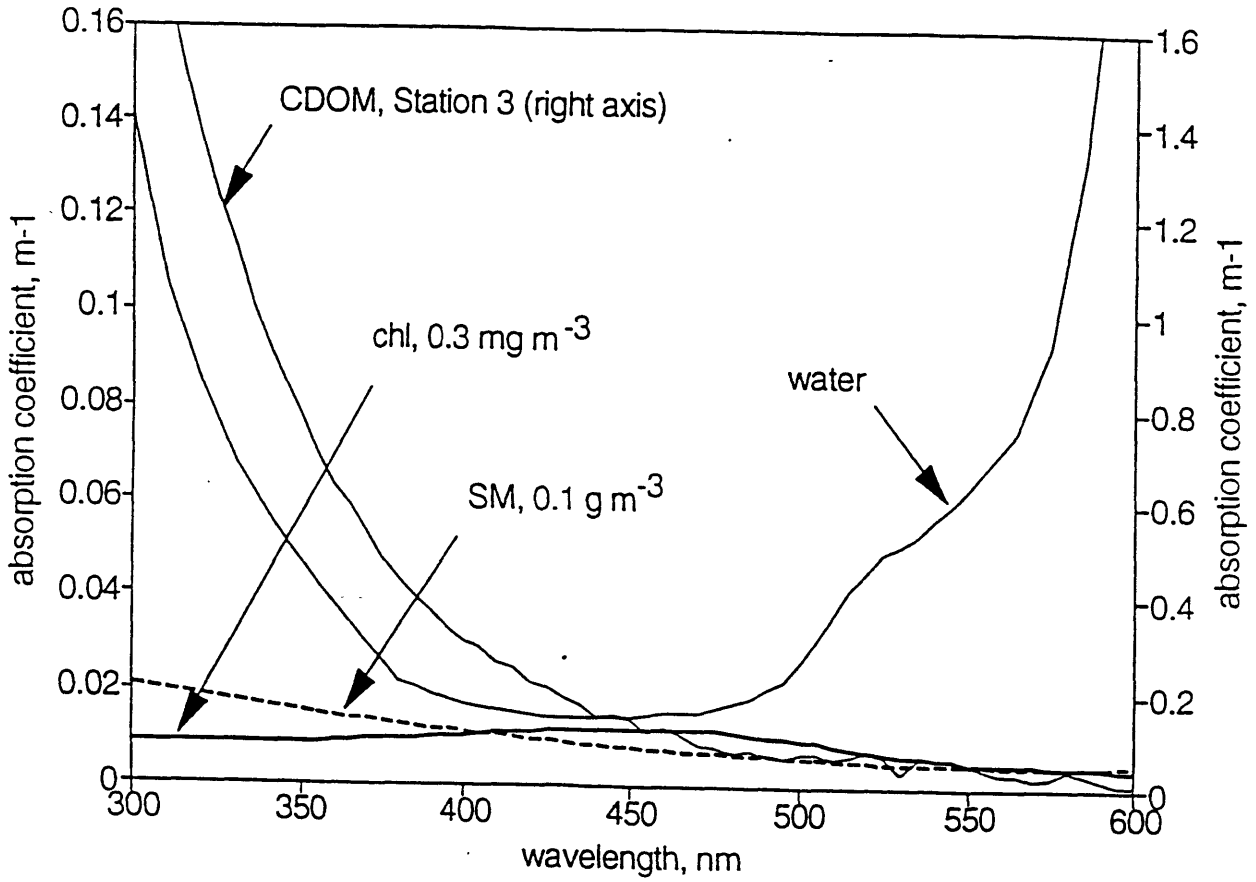

Figure 4-5: Spectral absorption coefficients for suspended mineral matter (SM), seawater, and chlorophyll *a* (chl). The curves for suspended mineral matter and chlorophyll *a* are derived from specific backscattering curves that have been multiplied by concentrations given in the figure (Vodacek et al (1994)). The absorption coefficient for CDOM has been measured from a sample taken at Station 3 in Vodacek's study 25 km from the coast of Georgia. The CDOM absorption is larger at this site than it was at BATS. On the other, it may be seen in this diagram that the water absorption dominates that of suspended mineral matter and chlorophyll. CDOM absorption is dominant at short wavelengths, so that the penetration of light in the water column is determined mostly by the water absorption alone or by water and CDOM absorptions at short wavelengths. This would be true both for this site and for the BATS site where absorption due to CDOM, suspended mineral matter, and chlorophyll would all be smaller; water would still be the dominant light attenuator at most wavelengths.

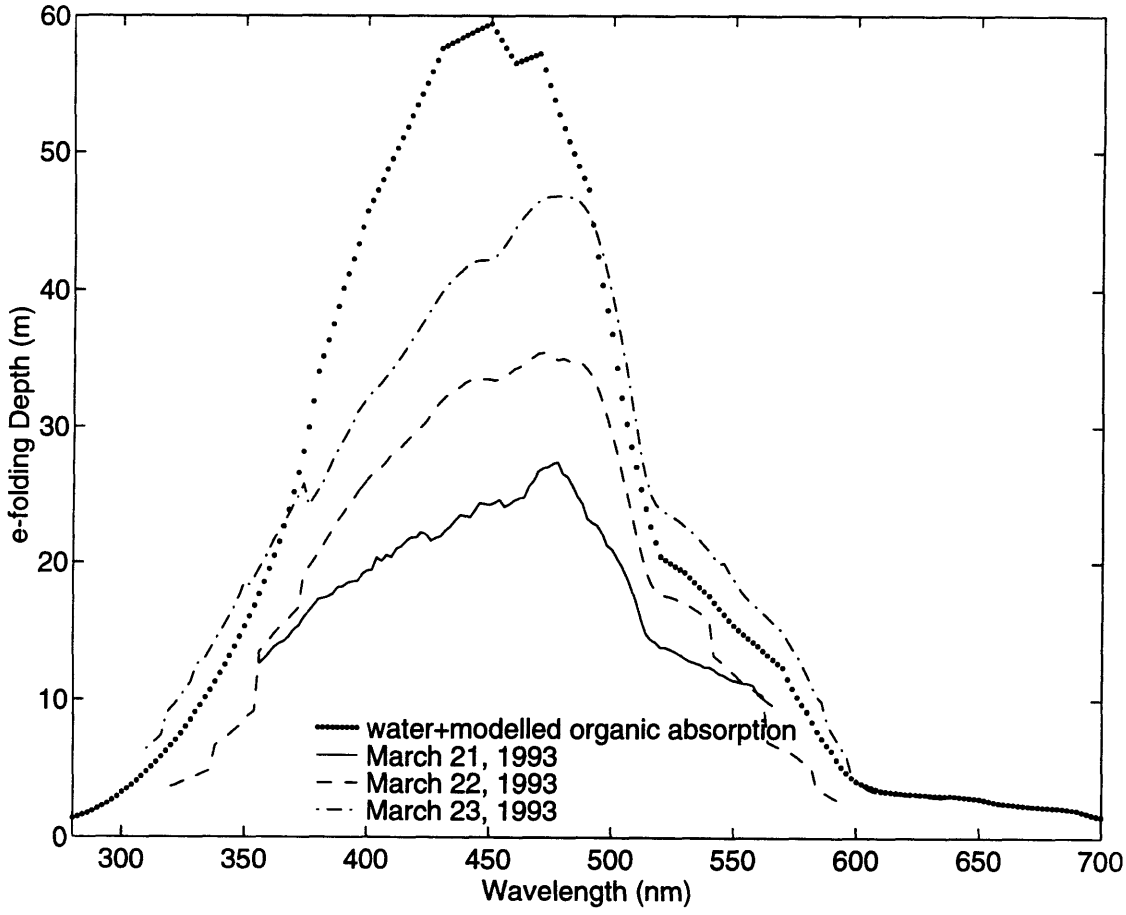

Figure 4-6: Measured and modelled e-folding depth of light penetration at BATS. The measured e-folding depth was calculated from spectral measurements of downwelling irradiance recorded on March 21–23, 1993. The modelled value was calculated from the sum of the attenuation and back-scattering coefficients of water (Smith and Baker (1981)) and the measured CDOM absorption versus distilled water. This modelled value was used in subsequent numerical experiments.

measurements of a_{CDOM}. In this respect, a_{CDOM} fluctuates during the course of a year and reaches a maximum during bloom conditions about April when the nutrient content of the upper ocean is high after deep winter mixing and solar energy input is also increasing. The concentration of DOC remains high through March (the period of the CO investigation) when secondary pigments are released into the water. The transparency of Sargasso Sea water should consequently have been low in March (Smith et al (1989)). By contrast, in early autumn the upper ocean is depleted in nutrients and DOC after being isolated during the summer months within the seasonal thermocline. In September (when the water sample was drawn from the Sargasso Sea for irradiation experiments) a_{CDOM} should have been a low value. The magnitude of the fluctuation in a_{CDOM} is not known for certain. However, it should be comparable to the range of diffuse attenuation coefficients for Sargasso Sea water presented by Siegel and Dickey (1987) for the wavelengths 410, 441, 465, 488, 520, 540, 560, and 589 nm at different seasons and times of day (Figure 4-7). The range of diffuse attenuation coefficients is significant, and it suggests that a_{CDOM} may have been higher in March than the measurement made of the water sample collected in September. This possibility was not explored in the model simulation described in Section 5 whose CO production is based on the a_{CDOM} measured for the seawater sample collected in September, 1993.

The spectral distribution of diffuse attenuation coefficient chosen for this model is thus roughly in agreement with corresponding values published in the literature. There is, however, some uncertainty associated with the diffuse attenuation coefficient and perhaps even some day to day variability as the LICOR data would suggest. If the scatter of the LICOR data indicates the uncertainty in the actual diffuse attenuation coefficient, then the actual value of K_d can only be known to within approximately 20% of its true value. The implications for this are small for the CO inventory but could be significant for sea surface [CO] if the mean e-folding depth of CO production exceeds the depth of the mixed layer. This is because the inventory represents the depth integrated amount of CO and does not depend on where the CO is produced in the water column. It thus depends on the amount of CDOM absorption (which

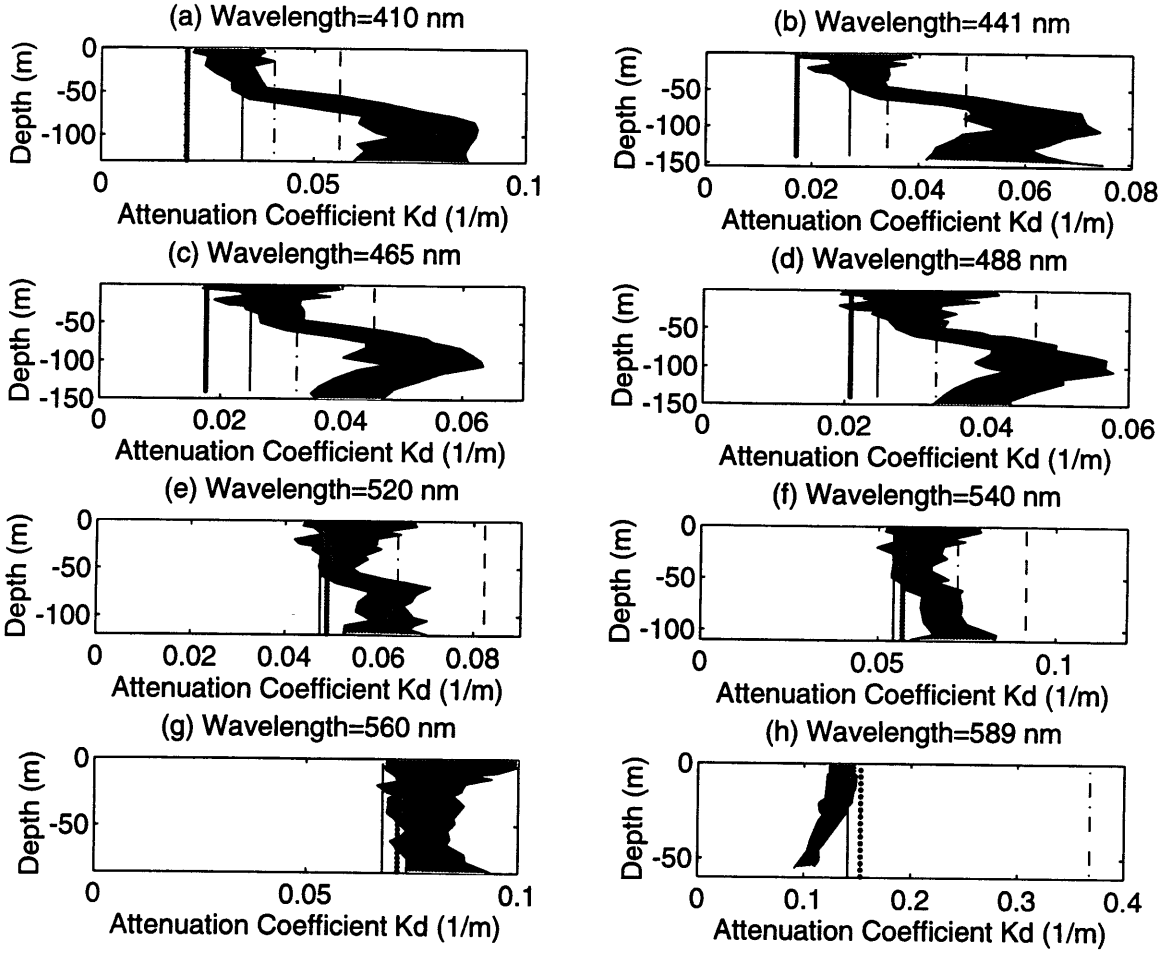

Figure 4-7: Comparison of diffuse attenuation coefficients of Siegel and Dickey (1987) (shaded envelope bounded by two solid lines with depth dependence) with the a_w values from Smith and Baker (1981) (dotted vertical line), the K_d values calculated from the LICOR data (dashed line, March 21; dot-dashed line, March 22; solid vertical line, March 23), and the c values used for the model in this investigation (vertical dotted line). The Smith and Baker (1981) and the model c coefficients agree with each other except at the shortest wavelengths where the CDOM absorption grows exponentially and becomes comparable with the water attenuation.

determines total CO production) but not diffuse attenuation coefficient (which determines the e-folding depth at which CO is produced). By contrast, mixed layer (and sea surface) [CO] depends on the amount of CO production within the mixed layer. If the e-folding depth of CO production exceeds the depth of the mixed layer, then a significant amount of CO is being produced at depths where it is not influencing mixed layer [CO]. In this case, the diffuse attenuation coefficient would important for determining sea surface [CO].

4.6 CO Production in the Water Column

The last step in the development of the production model is to apply the apparent quantum yield to the calculated underwater light field. In addition to presenting the procedure by which CO production was calculated from the light field, an attempt is made to deduce production trends as a function of time, depth, and wavelength. Qualitatively, it has already been seen how the maximum CO production occurs at a wavelength of about 320 nm at solar noon at the surface (Figure 3-6). However, the peak production might be expected to shift to longer wavelengths as the sun moves closer to the horizon because of increasing attenuation of ultraviolet light as direct sunlight passes through a thicker layer of ozone. In terms of penetration depth, it has already been seen that e-folding depth of light penetration at 320 nm is approximately 8 m. One would therefore expect CO production should be strongly surface trapped.

Because quantum yield refers to the relative efficiency with which CDOM produces CO per photon absorbed by CDOM, the first step in the modelling of CO production is to calculate the amount of energy absorbed by CDOM as a function of depth. However, there is a problem in that light is attenuated in the water column with an attenuation coefficient of $c(\lambda)$ made up of the sum of absorbance of CDOM and other materials. To isolate the amount of light absorbed by CDOM alone, the water column was divided up into a series of slabs of water $\Delta z = 0.5$ m thick, the day was divided up into time steps of $\Delta t = 1$ h, and the insolation spectrum was divided into steps of $\Delta\lambda = 2$ nm. Next, the amount of energy absorbed by the organic matter in

each slab of water was calculated by finite difference according to equations 4.13 and 4.14:

$$\Delta E_{w+CDOM}(\lambda, z_i) = E_d(\lambda, 0\mathrm{m})(\exp(K_\mathrm{d}(z_i - \frac{\Delta z}{2})) - \exp(K_\mathrm{d}(z_i + \frac{\Delta z}{2}))) \quad (4.13)$$

$$\Delta E_{CDOM}(\lambda, z_i) \approx \left(\frac{a_{CDOM}(\lambda)}{c(\lambda)}\right) \Delta E_{w+CDOM}(\lambda, z_i) \quad (4.14)$$

where $E_d(\lambda, 0\mathrm{m})$ denotes the downwelling irradiance just below the surface of the water, $E(\lambda, z_i)$ denotes the irradiance at depth z, w denotes absorption and backscattering due to water, and $CDOM$ denotes absorption due to coloured dissolved organic matter. The approximation indicated by the second equation is valid as long as $K_d \Delta z << 1$. This leads to a worst-case (300 nm) overestimate of 8% or 15% in CO production depending on whether a depth discretization of 0.5 or 1 m is used.

The actual CO production was calculated from the rate of energy absorption by CDOM according to the following equation:

$$J_{CO_{prod}}(\lambda, z_i) = \Phi(\lambda) \Delta E_{CDOM}(\lambda, z_i) \quad (4.15)$$

where $J_{CO_{prod}}(\lambda, z_i)$ is the rate of CO production in a volume $1\mathrm{m}^2$ by Δz (0.5 m for this section only) and $\Phi(\lambda)$ is apparent quantum yield. The apparent quantum yield used in the numerical model was that based on the experimental determination of quantum yield of BATS seawater using the modelled CDOM absorption (quantum yield parameterization 5 in Table 3.4 and Figure 3-6) which represents an approximately median value of surface and depth-integrated production for all the quantum yield parameterizations investigated.

This model gives useful insight into the trends of CO production expected as a function of time, wavelength, and depth. For instance, Figure 4-8 shows production rate versus wavelength for different times of day at 31°N on March 21. Interestingly, the wavelength of maximum production starts off at 315 nm at solar noon and then

migrates to longer wavelengths in the course of the day until it reaches 330 nm just before sunset. As has been mentioned above, the reason for this is increased ozone attenuation of ultraviolet light close to sunrise and sunset when the direct component of sunlight passes obliquely through a thicker layer of ozone.

The penetration of CO production into the water column as a function of wavelength is shown in Figure 4-9 at solar noon on Julian day 79 (March 21). The e-folding depth of [CO] is about 5 m for the wavelengths of peak surface CO production and is much smaller that the 23 m e-folding depth of penetration of the short-wave component of insolation used by Price et al (1987). The e-folding depth increases with increasing wavelengths due to the increasing transparency of the water to light.

Figure 4-10 shows a plot of the wavelength integrated production as a function of depth and time of day for Julian day 79 (March 21). The figure serves to reinforce the idea that the mean wavelength-integrated e-folding depth of production is in the range of 5–10 m.

Several important results concerning CO production have been obtained from this advanced model of light in the water column. First, the wavelength of peak CO production is about 320 nm. Also, production is strongly surface trapped, and the depth of the mixed layer is generally deeper than the mean e-folding depth of production (Figure 5-3).

Finally, it is appropriate to review the uncertainty associated with each of the models in turn. In estimating the surface irradiance from the extraterrestrial light field, Green et al (1980) assess their model at 5% accuracy. In correcting the theoretical surface with the measured insolation an ad hoc treatment was used and quantititative assessment of its error is difficult. However, the uncertainty was not in the intensity of irradiance but only in the spectral distribution so that a 10% estimated uncertainty is not unreasonable. The uncertainty in albedo varies from less 1% for small zenith angle to up to 50% near sunrise and sunset. However, because most of the CO production is near midday, the uncertainty in albedo near sunrise and sunset should not be very important. The diffuse attenuation coefficient has approximately a 20% error based on the discrepancy between the LICOR measurements, but again this should

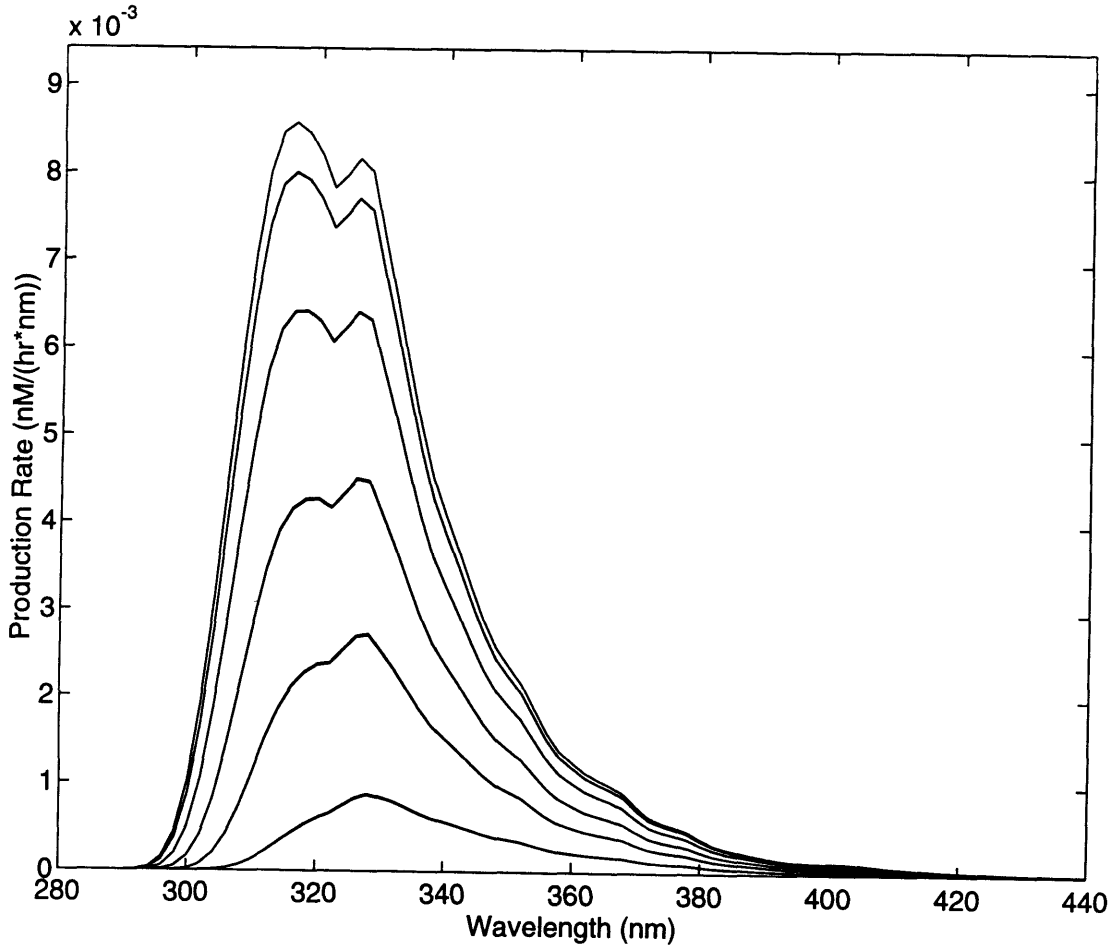

Figure 4-8: Wavelength and time dependence of surface CO production for quantum yield parameterization 5. The uppermost trace represents the spectral distribution of CO production at solar noon, 31°N, on March 21 (no clouds) (this corresponds to the trace labelled as "BATS; modelled absorption" given in Figure 4-8). The next lower traces are the production at 1–5 hours past solar noon. In addition to decreasing in amplitude, the wavelength of peak CO production moves from 315 to 330 nm just before sunset as the direct solar part of the spectrum passes obliquely through the ozone layer. The units have been converted to nM $h^{-1}nm^{-1}$ to make the plot easier to compare with literature values.

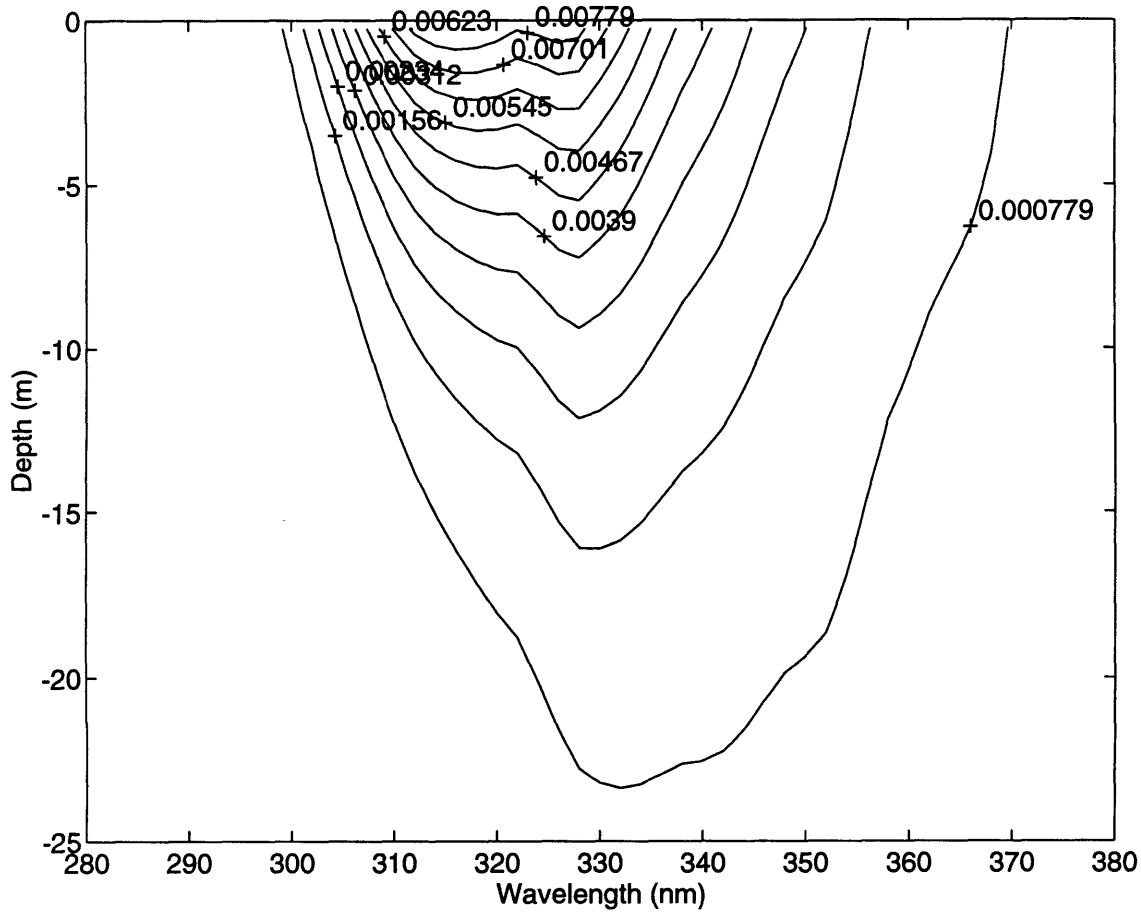

Figure 4-9: Depth and wavelength dependence of CO production at solar noon on March 21 (no clouds). The contours are given in units of nM CO $nm^{-1}h^{-1}$ The e-folding depth of CO production at the wavelength of peak production is about 5 m. The e-folding depth of CO production increases with increasing wavelength. The water attenuation for this calculation is given by the modelled value shown in Figure 4-6

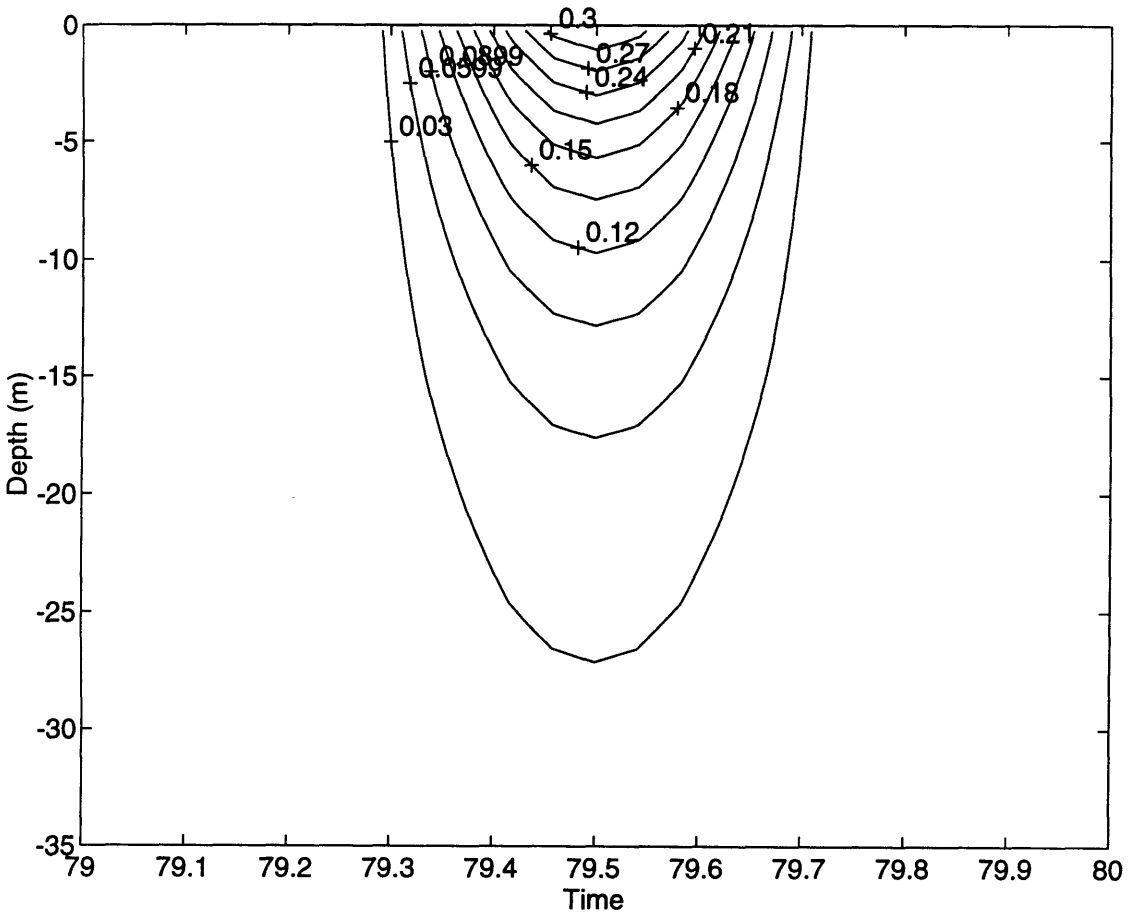

Figure 4-10: Depth and wavelength integrated production versus time of day and depth for quantum yield parameterization 5. The time is Julian day 79 (corresponding to March 21) with fraction denoting time of day in local solar time. The contours are given in units of nM hr^{-1}

not the very important because mean e-folding depth of CO production is much shallower than the mean mixed layer depth. This leaves the quantum yields with a high uncertainty based on the large error bars in the quantum yield measurements given in Appendix C. Quantum yield thus has the highest and most significant uncertainty. In this regard, a numerical simulation could serve to determine this quantity to a higher level of precision than has been achieved by laboratory experiments alone.

Chapter 5

Numerical Model Experiments and Sensitivity Studies

A numerical modelling study has been performed to simulate the diurnal cycle of [CO]. The model is a computer representation of the equation given in the first chapter describing the [CO] in the mixed layer as a function of time. This model incorporates production, destruction, mixing, and degassing terms to simulate the processes controlling the time dependence of [CO]. Each of these processes has been described in previous sections except for the mixing term which is described below.

There are several reasons for performing the numerical modelling study. At the most fundamental level, a numerical experiment may be run with the best measurements of the experimentally determined parameters to see how well the modelled and measured values agree. If the model and experimental results match, then it suggests that the assumptions made for the production, destruction, and mixing processes are consistent with the measured quantities of sea surface [CO] and CO inventory. If the model underpredicts the measured [CO], for example, then it is an indication that the experimentally determined apparent quantum yields may be too low, that there is too little CDOM, or that there is too little light. If (for example) the modelled sea surface [CO] overpredicts the measured values over certain periods and underpredicts the measured values over other periods, then it suggests that an important independent variable may have been overlooked in the parameterization. In this case, the ocean

may be temporally and spatially patchy with respect to its productive and consumptive elements, and modelling the [CO] fluctuation at the BATS site with a constant consumption e-folding time and production coefficient might result in discrepancies.

The numerical model also allows explicit calculation of the total production, destruction, degassing, and dilution as a function of time. This permits an assessment of the relative importance of these terms in controlling the [CO], at least for the conditions encountered during this investigation. It is also a qualitative indication of which variables are most important in controlling [CO].

This information is useful for inverse modelling studies which attempt to optimize estimates of independent variables. This essentially involves iterating the numerical model many times, while systematically altering some independent parameter important in controlling [CO]. At the end of the run, a mean absolute deviation between the model and measured results is calculated, and the minimum deviation corresponds to an estimate of the optimized parameter. The sensitivity of the optimized independent variables to small perturbations in the sea surface [CO] or CO inventory forms the basis of the sensitivity analysis.

The basis of this inverse study, however, is an accurate parameterization of the physics of the mixed layer. This is described below.

5.1 Physical Model

The CO production and destruction mechanisms were coupled with a mixed layer model of the upper ocean to understand the influence of physical mixing in modifying the [CO] signal at the surface and at depth. In this respect, several mixed layer models exist that predict the depth of the mixed layer in response to wind mixing and solar insolation through the course of a day. However, the model which is used in this study is that developed by Price et al (1986) and is known as the PWP model. It is described as a one-dimensional critical parameter model and attempts to simulate the time evolution of the mixed layer and transition layer.

This model was used without modification except for the constants describing the

short and long-wave components of insolation and their respective e-folding penetration depths in the water column. In this regard, the insolation parameters used by Price et al (1987) were used instead. These assume that 58% of the insolation is made up of a long wavelength component which has an e-folding penetration depth of 3.5 m. The remainder is made up of shorter wavelength insolation with a penetration depth of 23 m. (The same light model developed above for CO production was not used here because the narrow wavelength range for which it is applicable (280–380 nm according to Green et al (1980)) corresponds to a small fraction of the total insolation.)

The PWP model is identified as a one-dimensional model because it divides the upper water column into a series of boxes $\Delta z = 1$ m in thickness, each with an associated temperature, salinity, density, velocity, and [CO] (for this investigation). It is forced by meteorological parameters imposed at the surface of the water column at time steps of $\Delta t = 0.25$ h. For example, net heat loss at the surface of the water in one time step is translated into a decrease in the temperature of the uppermost box and a corresponding increase in density. Similarly, high wind stress increases the water velocity in the uppermost box, and a precipitation event serves to decrease salinity.

High temperature or salinity signals in the uppermost box are propagated through the water column based on several mixing criteria. First, the static stability criterion states that:

$$\frac{\partial \rho}{\partial z} \geq 0 \tag{5.1}$$

where ρ is density. This condition might be violated, for instance, at night when there is no insolation and only net heat loss. This would tend to cool the uppermost box to the point where it becomes denser than the boxes below it, and spontaneous mixing occurs.

Mixing also occurs during high wind events when the difference in horizontal velocities between the mixed layer and the layer immediately beneath it becomes too

great. This interplay between the destabilizing influence of velocity shear and the stabilizing influence of density stratification is parameterized in the bulk Richardson number, R_b. Mixing occurs when the bulk Richardson number exceeds a critical value given by the following condition:

$$R_b = \frac{g\Delta\rho h}{\rho_o(\Delta\mathbf{V})^2} \geq 0.65 \tag{5.2}$$

where g is the acceleration due to gravity, h is the depth of the mixed layer, and Δ takes the difference between the mixed layer and the layer just below it.

These two mixing criteria create a mixed layer with a sharp jump in temperature, density, etc., at the base and a minimalized transition layer. This is not consistent with physical observations of the mixed layer, and Price et al (1986) include the gradient Richardson layer criterion (assuming that sharp jumps in momentum would be sites of shear flow instability) in order to more effectively simulate transition layer characteristics and smooth out property profiles. This gradient Richardson number criterion is given by the following equation:

$$R_g = \frac{g\partial\rho/\partial z}{\rho_o(\partial\mathbf{V}/\partial z)^2} \geq 0.25 \tag{5.3}$$

Qualitatively, the PWP model is successful in predicting the profiles of salinity, temperature, velocity, and density in response to various atmospheric forcings on those days when there are no advection effects. For example, this means that the mixed layer will tend to deepen during a low insolation, high wind event (i.e. during a windy night) and shoal during days of high insolation and low wind.

5.2 Initial Conditions and Boundary Conditions

The physical PWP requires starting reference profiles of temperature, salinity, current velocity. Temperature, salinity, and current velocity profiles at subsequent times are determined by application of the meteorological parameters (surface heat loss, insolation, wind stress, and evaporation minus precipitation) which form the boundary

conditions.

The 10 minute averaged meteorological file described in the methods and data set section was used here. The east and north components of wind stress for the investigation period are given in Figure 2-7. The components of insolation and surface heat flux for the investigation period have already been given in Figure 2-9. The record of evaporation minus precipitation is given in Figure 2-11 and shows a single rain event on the night of March 19–20.

There was difficulty starting the physical model simulation at the start of the observational study on the morning of March 15 because the initial CTD profile (which forms the basis of the initial conditions) records only temperature and salinity. There is no information about the current velocity profile, and consequently this has to be initialized to zero. However, the initial current is important for determining the shear flow instabilities and the depth of mixing.

In starting the current velocity profiles at zero, time must be allotted at the beginning of the model to allow a spin-up of the current to steady-state conditions. In this regard, Gnanadesikan (1990) allows stabilization to steady-state conditions over a 10 day period. In this investigation, the spin-up period is limited by the length of the meteorological record before the start of the CO measurement program. The ship arrived on station in the evening of March 14, 1993, and the meteorology record collected on the ship during latter part of March 13 and March 14 (local solar time) is thought to be representative of the weather conditions at the BATS site. Thus, the spin-up period of the model for this investigation is about 1.5 days, and the model was initialized on 19:43 (local solar time) on March 13, 1993 with the temperature and salinity profiles collected by CTD measurement at 6:37 local solar time on March 15, 1993. The short spin-up of this model compared to Gnanadesikan (1990) does not have a significant effect on the modelled sea surface values of temperature and salinity for the March 15-25 period.

Additional problems were posed by the passage of temperature fronts apparent in the sea surface temperature record. The model was not stopped and reinitialized with new temperature and salinity profiles after the passage of successive fronts. This

resulted in a modelled sea surface temperature record which did not have the discontinuities present in the observed record. However, this did not affect the physics of the model because the sensible heat flux (proportional to the difference in temperature between the air at 10 m and the sea surface) was based on the measured temperature record and would not have been biased by the inaccurate modelled sea surface temperatures. As well, the passage of the temperature fronts did not have an effect on the depth of the mixed layer except on March 17. Thus, the modelled sea surface [CO] should not have been affected by the passage of thermal fronts except where these thermal fronts changed the production and consumption properties of the water.

Because the chemical model had a complete set of initial conditions in the form of a starting [CO] profile, no spinup time had to be allotted for [CO] to reach a steady state. Instead, the [CO] profile was initialized with CO measurements of water collected in a CTD rosette at 6:37 local solar time on March 15, 1993. (The measured [CO] of the sample collected at 120 m was not used because it was badly contaminated.)

5.3 Baseline Model Simulation

The baseline simulation provides a means of obtaining an initial assessment of the model and of the experimentally determined independent variables. In this respect, the meteorological forcings outlined in Chapter 1 were used here without modification. The apparent quantum yield used here was that which was obtained by measurement of BATS water using the modelled CDOM absorption (model 5 in the intercomparison study of the laboratory section above). The CO consumption e-folding time used for this first model run was the 52 h value determined by shipboard incubation experiment. The piston velocity was that of Liss and Merlivat (1986).

5.3.1 Output of Physical Parameters

With respect to the physical parameters, the baseline model simulation provides a means of making a qualitative assessment of the accuracy of the output. It provides

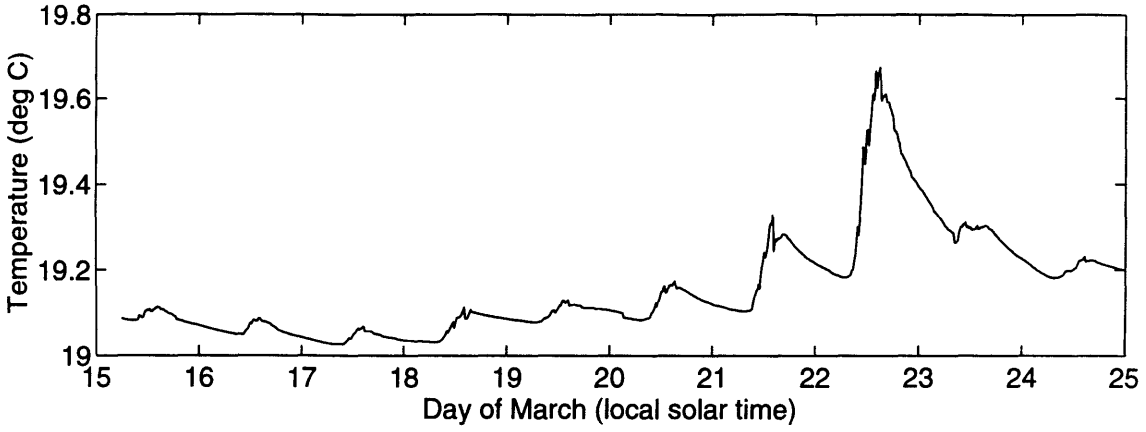

Figure 5-1: Sea surface temperature generated by the PWP model for the period March 15–25, 1993

an estimation of the theoretical amplitude of the diurnal temperature cycle in the absence of advection effects. This may be compared with the measured sea surface temperature to find those days where a diurnal mixing cycle was in progress. The model also provides an estimation of the depth of the mixed layer, and this has implications for the chemical model in assessing the depth of mixing of CO into the water column.

The sea surface temperature record generated by the baseline model (Figure 5-1) predicts a diurnal cycle in the sea surface temperature record every day. For most days, the magnitude of the temperature increase amounts is less than 0.05°C, but on March 21 and 22 there are diurnal temperature peaks of about 0.2°C and 0.4°C, respectively. Given the approximately equivalent heating conditions for all days, the greatest contributor to this phenomenon is probably the four-fold decrease in wind stress on March 21–22. The actual measured of sea surface temperature also indicates a pronounced diurnal sea surface temperature signal on these days and no clear signal on other days.

The sea surface salinity time series record generated by the PWP model is shown in Figure 5-2. The sea surface salinity does not exhibit a diurnal signal, but does show a downward step of about 0.004 ppt on the night of March 19–20, 1993, corresponding

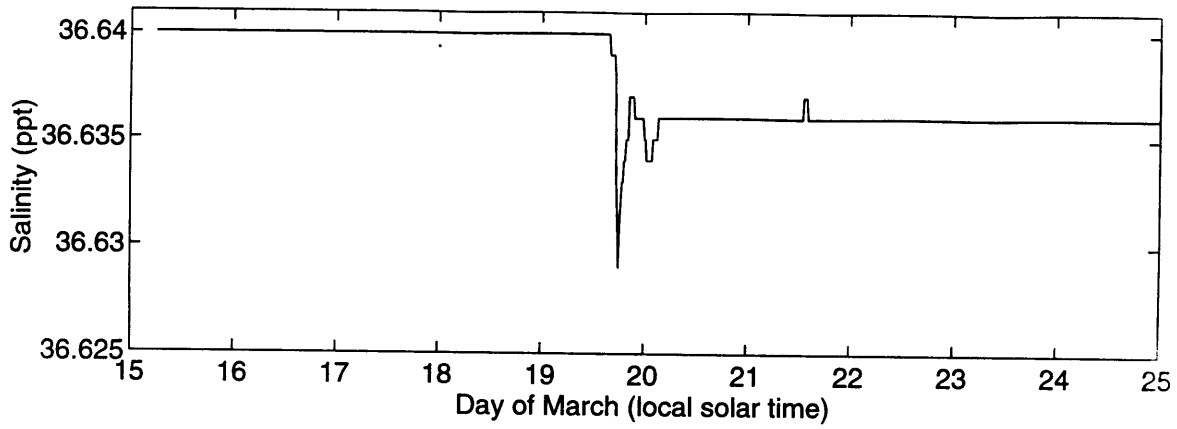

Figure 5-2: Sea surface salinity generated by the PWP model for the period March 15–25, 1993

to the rain event. This would have served to make the surface waters more buoyant and might have contributed to a shoaling in the mean depth of the mixed layer (shown below) in the latter part of the investigation period (in combination with the low winds of this period). In this respect, both the model and the observations show an increasing trend in the sea surface [CO] after the rain event consistent with increased surface trapping and suppression of deep mixing.

The depths of the mixed layer in the model and measured temperature profiles are presented in Figure 5-3. For the model the depth of the mixed layer is defined as the first depth below the surface at which density difference between adjacent density steps exceeds 0.0001kg m^{-3} (an arbitrarily chosen number). This may be regarded as the depth over which mixing occurs to homogenize density. For the measured temperature profiles the depth of the mixed layer is defined as the depth where the temperature difference with the sea surface first exceeds 0.02°C (Price (1986)). This different convention had to be chosen for the measured temperature profiles because no salinity data were collected during the XBT measurements and hence density profiles could not be calculated. The measured and modelled mixed layer depths show good agreement during periods when a diurnal thermocline is in place but only moderate agreement at times of deep mixing during the first half of the investigation

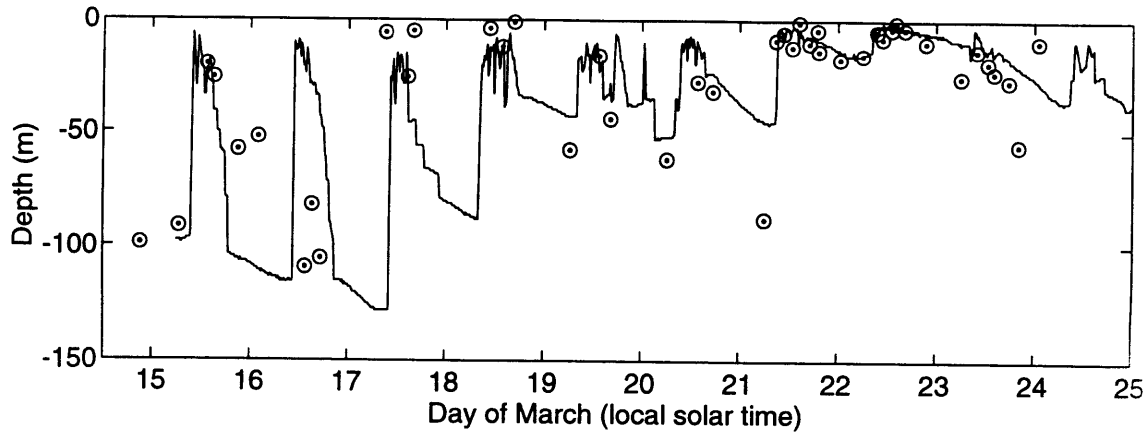

Figure 5-3: Depths of the mixed layer generated by the PWP model (solid line) and measured from the CTD and XBT temperature profiles (centered circles). The criteria used to define the mixed layer depths are described in the text. The plot shows good agreement between the modelled and measured mixed layer depths at times when a diurnal thermocline was in place but only moderate agreement at other times.

period.

The significance of knowing the depth of the mixed layer was suggested in the previous paragraph. Because of dilution effects, the magnitude of the sea surface [CO] should be inversely proportional to the depth of the mixed layer with all other variables kept constant. Qualitatively, the model predicts the deepest mixed layers during the windiest days at the beginning of the investigation, and this corresponds to the lowest amplitudes in both sea surface [CO] and sea surface temperature. As well the shallowest mixed layer depths occur on March 21 and 22 during the calmest days, also corresponding to the highest amplitudes of modelled sea surface temperature and sea surface [CO].

The physical model thus seems consistent with the observed meteorological and sea surface parameters.

5.3.2 Output of Chemical Parameters

The results of the baseline simulation indicate that there was good agreement in the trends between the various CO observations that were made in the period March 15–24 and the model output. The mean average absolute deviation between the model and measured values of [CO] was 0.06 nM; about the same as the estimated 5% measurement error associated with individual measurements (or 0.05 nM error for the mean measurement of 1.0 nM). The production and destruction parameterizations seem to be effective although the specific values for the constants may be inaccurate.

A comparison between the measured and modelled sea surface [CO] is presented in Figure 5-4. The baseline model predicts a diurnal variation in sea surface [CO] similar to that observed. However, the model overpredicts the measured [CO] on March 22 and 23.

Figure 5-5 shows three graphs comparing the depth-integrated CO inventories between the measured data set and the model simulation. The first graph shows the CO inventory between 0–50m, the second between 50–120 m, and the third between 0–120m. In all cases, the modelled inventories tend to underpredict the measured values. For the 50–120 m CO inventory there is an additional concern that the modelled inventory exponentially decays to zero over the ten day period whereas the observed inventory is approximately constant. The CO at this depth is being consumed by bacteria according to the 52 h consumption e-folding time but is not being replenished by surface mixing nor by light-induced production below 50 m. A model experiment where CO diffusion effects were allowed similarly could not move enough CO into the 50-120 m region. (In this particular experiment, CO but not temperature or salinity was allowed to diffuse at every time step with an eddy diffusion coefficient of $1.0 \times 10^{-4} m^2 s^{-1}$). These results would suggest that the current model is not adequate to produce a [CO] of about 0.25 nM below the euphotic zone, even with the inclusion of a diffusion term. This might have been due to a blank correction of the [CO] measurements, to the absence of CO consuming bacteria at depth, to some subtlety of CO metabolism of the bacteria, or to a dark production mechanism of CO.

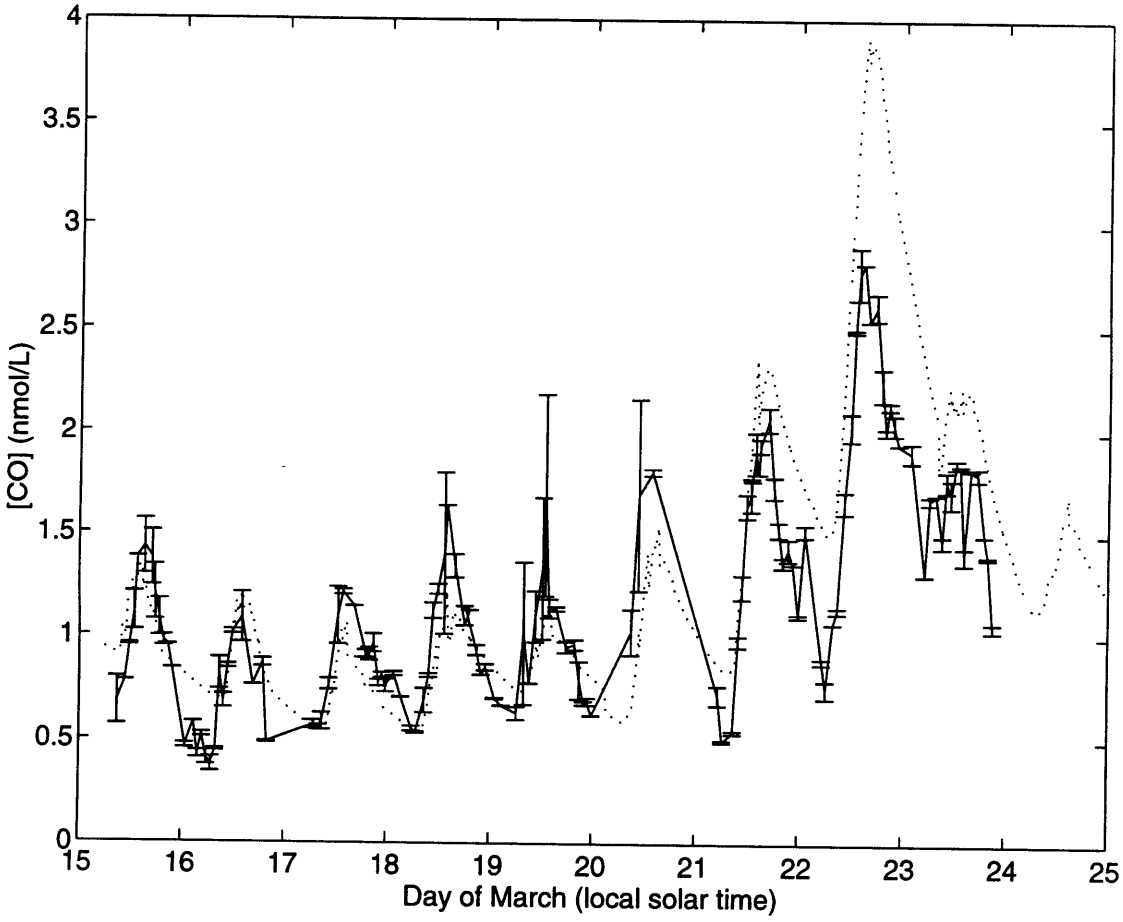

Figure 5-4: Comparison of measured sea surface [CO] and that generated by the PWP model with baseline CO generation parameters. The baseline model and measured sea surface [CO] show very good agreement.

The inventories show a 75% increase in CO content in the upper 120 m between 0620 and 1444 local solar time on March 21 corresponding to the passage of a surface temperature front at about 0900. At the same time, the daily insolation energy input into the mixed layer for March 21 and 22 was only about 20% higher than what it was for the first part of the investigation period and can not explain the increased CO inventory starting on March 21. This suggests that the the passage of the thermal front may have been associated with a change in the production or consumption capacities of the seawater, although this can not be confirmed by measurements of consumption rate which ended on March 20. It is not possible that the discontinuities in temperature and CO inventory could have arisen from a different short insolation history. First, the ocean could not have absorbed enough solar energy in the three hours after dawn to increase the sea surface temperature in a 0.5°C jump. Secondly, to account for the 75% increase in CO inventory on March 21 from the previous day, the insolation would have had to substantially exceed its theoretical maximum clear-sky amplitude for that latitude and time of year.

Figure 5-6 presents time series of the modelled production, consumption, dilution, degassing rates averaged over the the depth of the mixed layer (the depth of the mixed layer being that defined in the model and shown in Figure 5-3). This diagram illustrates the relative contribution of each of the production or loss mechanisms serving to change the [CO] in the mixed layer. The mean consumption and degassing rates averaged over the mixed layer appeared to experience a diurnal cycle similar to the light-induced production rate. The changes in mixed layer [CO] due to dilution were more episodic in nature and followed periods of mixed layer deepening.

To better understand the relative importance of these parameters, an explicit calculation was made of the time average (between 6:37 local solar time on March 15 and 24:00 local solar time on March 25) of each of the terms in the mass balance equation given in the Introduction (i.e. a mean rate of change of the mixed layer [CO] ascribed to production, microbial consumption, degassing, and dilution due to mixed layer deepening). The mean CO production rate was 0.0391 nM h^{-1}, the mean consumption rate was 0.0246 nM h^{-1}, the mean dilution effect due to mixed

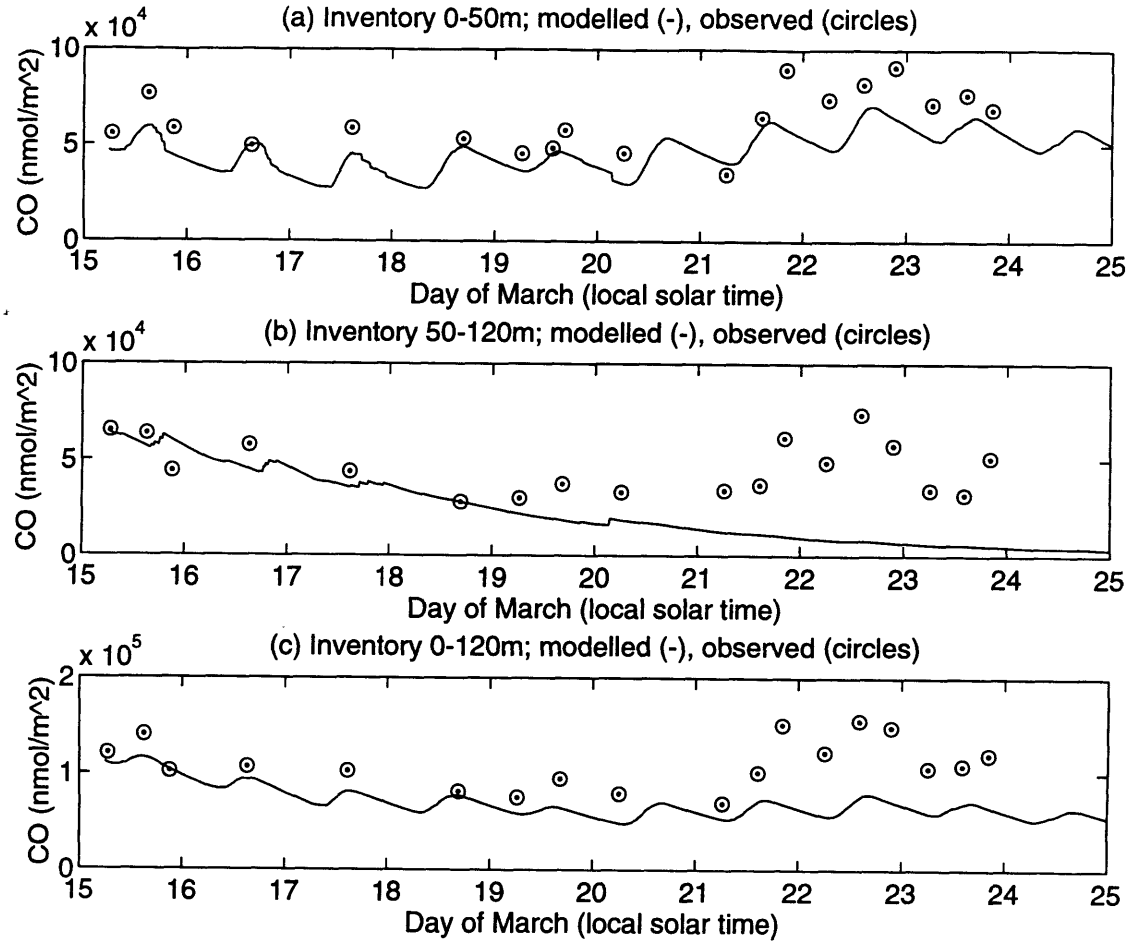

Figure 5-5: Depth-integrated CO inventories produced from observations (centered circles) and the physical/chemical model (solid line). The uppermost graph gives the CO inventory integrated from 0–50 m, the middle graph gives the inventory for 50–120 m, and the lowermost graph gives the inventory from 0–120 m. The model predicts that the deepest inventory (50–120 m) should vanish over the period of the ten day run. This is consistent with the fact that little CO was generated below 50 m by penetrating light fields or moved there by deep mixing or diffusion. With the absence of such sources, the existing pool of CO was consumed by bacteria according to the exponential decay model for the microbial consumption.

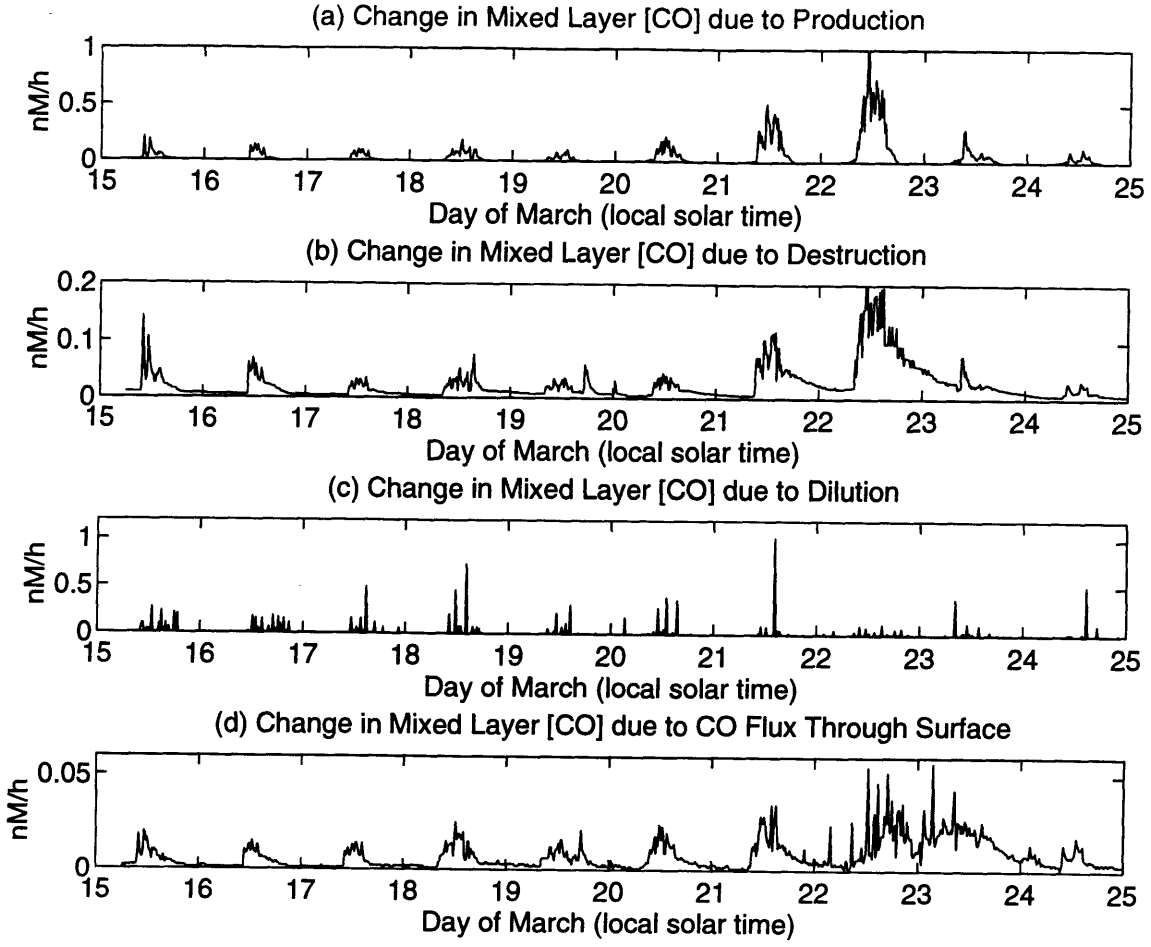

Figure 5-6: Time series of production, consumption, dilution, and degassing rates averaged over the depth of the mixed layer (the depth of the mixed layer being that defined in the model and shown in Figure 5-3). Light-induced production has the greatest effect in the rate of change of [CO], microbial consumption is second, dilution due to mixed layer deepening is third, and degassing through the surface is last. Like the production, the rate of microbial consumption and degassing are observed to experience a diurnal variation. Dilution due to mixed layer deepening tends to be more episodic and linked to periods of mixed layer deepening.

layer deepening was 0.0131 nM h^{-1}, and the mean effect that degassing had on the mixed layer was 0.0075 nM h^{-1}. In terms of the mean [CO] of the entire mixed layer, degassing was about 0.2 times the production term and about 0.3 times the consumption term. The mean dilution effect due to mixed layer deepening was about 0.3 of what was attributed to light-induced production.

Conceptually, the rate change of mixed layer [CO] must balance the rate of change of [CO] ascribed production, consumption, degassing, and dilution averaged over the depth of the mixed layer at every time step. In this regard, the effect of the production, consumption, and degassing terms may be explained in terms of net amount of CO entering or leaving the mixed layer at each time step divided by the depth of the mixed layer to find a change in concentration. Entrainment of CO-depleted water into the base of the mixed layer can also result in a decrease in [CO] through dilution. Here, the dilution effect is calculated by finding the amount of CO in the mixed layer at one time step and spreading this out over depth of a deeper mixed layer in the next time step (adjusted for the existing [CO] of the entrained layers). If the mixed layer does not deepen or if a new mixed layer forms on top of the old, then no dilution takes place. For the case of the formation of a new mixed layer on top of the old, the model restarts the CO accounting system for the new mixed layer, and the CO in the old mixed layer is sequestered at depth and decays by microbial consumption. If the new mixed layer cuts downs to this depth, then the sequestered CO will be mixed to the surface. However, such deep mixing events occur about once per day so that by the time the new layer reaches the depth of the old layer, the CO has mostly been depleted by bacterial consumption.

5.4 Optimizing Baseline Parameters

With this information, it is possible to attempt to get more accurate determinations of the parameters controlling sea surface [CO] and CO inventory by using the physical/chemical model. This requires using an inverse approach in which the model is run a number of times to find the values of the independent parameters that minimize

the mean absolute deviation between modelled and measured dependent quantities. From the results of the above analysis, the production and destruction rates are the most important quantities controlling the mixed layer [CO], but variables controlling the depth of the mixed layer are also significant.

5.4.1 Inverse Study Description

A series of model runs were made to perform sensitivity tests of a number of independent variables controlling the sea surface [CO] and CO inventory. The eight variables that were chosen for this analysis were production rate, destruction rate, degassing rate, wind stress, surface heat flux, diffuse attenuation coefficient (or the water and CDOM absorption together), latitude, and insolation. Inverse models were conducted with these variables so as to minimize mean absolute deviations between measured and modelled values of selected dependent variables. These dependent variables were sea surface [CO], CO inventory, and times of maximum afternoon sea surface [CO].

All of the independent parameters were relevant in controlling [CO] in the mixed layer. Production rate and destruction rate were obvious choices for the inverse study because they are the most important terms in the CO budget and also because they were subject to the largest uncertainty. The degassing rate is suspected to have a smaller influence, but published studies have shown that it may be subject to large uncertainty. It has been included in this inverse study to attempt to find an optimized value with error limits. Wind stress, surface heat flux, and diffuse attenuation coefficient were all subject to uncertainties of up to 10%. Because the influence of these parameters on [CO] is somewhat indirect, it is difficult for an inverse study relying on [CO] to find an optimum value of these parameters better than could be obtained by direct measurement. They are nevertheless included in the sensitivity analysis. Likewise, both insolation and latitude can be determined experimentally with great precision and accuracy. The inverse model for CO would not be effective in optimizing these parameters to a higher degree of refinement, and they are included here only for the sensitivity analysis.

Many of these variables are not independent of each other and variations in them

tend to produce similar effects. For instance, if there were no dynamics to consider, then increasing the light field (or insolation) by 50% percent would have the same effect as increasing the quantum yield by 50% both in sea surface [CO] and in CO inventory. Changing the latitude would have an equivalent effect as changing the zenith angle and hence the light field. Increasing the diffuse attenuation (i.e. water and CDOM absorption) coefficient by 50% would causes light (and CO production) to be trapped near the surface. If the mean e-folding depth of CO production is deeper than the mixed layer depth, then sea surface [CO] would tend to be increased because a greater proportion of a given production is within the mixed layer. The depth-integrated CO inventory would not be increased because CO production depends on the number of short-wave photons absorbed by CDOM relative to water, and in this scenario the proportion is constant for any diffuse attenuation coefficient value.

The degassing and microbial consumption rates are both proportional to [CO]. Hence, if there were no dynamics effects to consider, then increasing production by 50% would lead to 50% increases in degassing and CO consumption rates, and [CO] would reach a new equilibrium at a new level.

If dynamic effects are included, then the situation becomes more complicated. For instance, increasing insolation by 50% not only causes an increase in CO production but increases heat input to the sea surface. This promotes the formation of a diurnal mixed layer, which results in a further trapping of heat and CO and ultimately leads to diurnal maxima in temperature and [CO] at the sea surface. Changing latitude may lead to alteration in the insolation levels with the same effects described above. It has the additional effect of changing Coriolis parameter which determines the tendency of geophysical fluid flows to veer to the right in the northern hemisphere. Increasing latitude tends to increase the Coriolis parameter and to decrease the mixed layer depth with its attendant increase in sea surface [CO] and temperature.

Wind stress is another variable with multiple effects on the CO budget. For example, the degassing rate from the uppermost layer of the model ocean is dependent upon wind speed, and in the absence of dynamics effects would tend to cause a decrease in sea surface [CO]. With respect to its dynamical effects, wind stress also

acts to impart kinetic energy to the mixed layer, and increased wind stress causes the mixed layer to deepen and sea surface [CO] to decrease. The sensible heat flux from the surface of the ocean is also proportional to wind speed, and increasing wind speed can lead either to enhanced heat input or heat loss depending on the direction of the temperature gradient. In general, heat loss tends to create cooler denser water at the surface which enhances mixing associated with static instability. This causes a deepening of the mixed layer and an associated decrease in sea surface [CO].

The dependent variables were chosen on the basis of available measurements and of effectiveness in characterizing the independent variables. Measurements of sea surface [CO] were made at 126 different times during the investigation period and seemed to the most effective at optimizing estimates of independent variables. They were subject to a possible unknown error associated with the bucket sampling procedure or with the possible existence of vertical gradient of [CO] very near the surface. (This has been explored to a small extent in Chapter 2.) CO profiles were measured at 18 times during the investigation period to depths of 120 m or more. Inventories were calculated by integrating [CO] over depth and linearly interpolating [CO] between data points. The optimized values for the independent variables obtained by inventory tended to be slightly larger than those obtained by sea surface [CO]. In principle, using the times of maximum sea surface [CO] is a method which could accurately and uniquely determine the e-folding CO consumption time. It is based on the notion that the time of the maximum could shift up to six hours based on the value of the e-folding CO consumption time. Unfortunately, it requires a higher density of data than was available in this study, which yields only 8 daily maximum times, and this was not a practical method of finding optimum values.

The inverse study thus concentrated on finding the values of the independent variables that minimized deviations in the dependent variables given by:

$$\Sigma|x_i(\text{model}) - x_i(\text{measured})|$$

where x_i is sea surface [CO], CO inventory, or time of maximum afternoon sea surface

[CO]. The inverse models were structured in such a way as to consist of 100 forward or ordinary model runs where 2 of the 8 independent variables mentioned above were varied systematically over a range of 10 values. For production rate, degassing rate, wind stress, surface heat flux, diffuse attenuation coefficient, and insolation this involved multiplying these parameters by multiplication factors that ranged from 0.2 to 2; 1 being the baseline value.

The results of these 100 models runs were mean absolute deviations between the modelled and measured sea surface [CO], CO inventory, and times of afternoon [CO] maxima. These data were contoured and plotted against the two independent variables that were systematically varied for the study. In the ideal case, the contour plot would show a minimum corresponding to optimized values for both of the independent variables. In a less idealized but more typical case, the contour plot would show a valley indicating optimization of one independent variable and an insensitivity in the other variable to controlling the CO budget.

A total of 21 inverse model runs were made, and the values of the independent variables for each run are given in Table 5.1. The first inverse model run was that for the quantum yield coefficient/microbial consumption time constant parameter pair. These were subject to the largest uncertainties and the results of this optimization were introduced into subsequent inverse models; the quantum yield coefficient and microbial time constant consumption rate taken as 2.2 and 45 hours, respectively.

For each inverse model run, the optimized value of one independent variable of the pair under investigation was determined by first finding its value corresponding to minimum mean absolute sea surface [CO] discrepancy or mean absolute CO inventory discrepancy in the series of 10 model runs where the second independent variable was altered. This gave 10 estimates of the optimized value of one independent variable obtained from the 10 forward model runs where the second independent variable was varied. For a given inverse model run, the optimized value of one variable was taken as the median value of these 10 optimized estimates. The optimized value of its uncertainty was taken as the median value of the 10 uncertainties associated with the 10 optimized values.

The method of finding the optimized estimate of a variable is thus similar to the Monte Carlo method where an estimate is made of the variable by finding the median of a set of 10 calculated estimates representing small perturbations from the true (though unknown) value. The perturbed values in this case are generated by systematically varying a second independent variable and calculating the effect of the variation on the estimate of the first. The value of a given independent variable (given at the top of Tables 5.2 to 5.9) is determined several times by varying several other independent variables (listed in the left-hand column of the same tables).

The location of the minimum was refined by fitting a parabola to the point of minimum mean absolute deviation and the two adjacent points. In addition, the curvature of the parabola gave measure of the uncertainty of the independent variable. If the parabola was almost flat, then a wide range of values for the independent variable could satisfy the minima, and the variable would be said to have a high uncertainty. If the parabola were very steep, then the independent variable would be tightly constrained and be said to have a low uncertainty. The uncertainty given in the tables below represents an amount of deviation of the independent variable away from its optimized value corresponding to a 10% increase of the quantity $\Sigma|x_i(\text{model}) - x_i(\text{measured})|$ above its minimum value.

Additionally, a sensitivity parameter was defined as the ratio of the optimized value to its uncertainty. A parameter with a low relative uncertainty would thus has a high sensitivity and vice versa. This convention is appropriate for all the variables except latitude, and here the sensitivity parameter is defined as 180° divided by the uncertainty in latitude.

5.4.2 Inverse Study Results

The inverse study was successful in assessing the relative sensitivity of each of the 8 independent variables investigated, but was only partially successful in finding the optimized values of these independent variables.

Only the apparent quantum yield coefficient and the e-folding time for CO destruction could be determined with a level of accuracy that is comparable to the

Table 5.1: Description of inverse models with summary of parameters. i is an integer which is varied from 1–10 in the inverse model runs

Model No.	Parameter							
	Φ	τ_c (hours)	I	L	$\lvert\tau\rvert$	ϕ	V_P	K_d
1	0.4i	10+30(i-1)	1.0	1.0	1.0	$31^o\ 50'$	1.0	1.0
2	1.3	45.0	1.0	$\frac{i}{5}$	$\frac{i}{5}$	$31^o\ 51'$	1.0	1.0
3	1.3	45.0	$\frac{i}{5}$	1.0	1.0	9i	1.0	1.0
4	1.3	15i	1.0	1.0	1.0	$31^o\ 50'$	$\frac{i}{5}$	1.0
5	1.3	45.0	$\frac{i}{5}$	1.0	1.0	$31^o\ 50'$	1.0	$\frac{i}{5}$
6	1.3	45.0	$\frac{i}{5}$	$\frac{i}{5}$	1.0	$31^o\ 50'$	1.0	1.0
7	1.3	45.0	1.0	1.0	1.0	9i	1.0	$\frac{i}{5}$
8	1.3	45.0	1.0	1.0	$\frac{i}{5}$	$31^o\ 50'$	1.0	$\frac{i}{5}$
9	1.3	45.0	1.0	$\frac{i}{5}$	1.0	$31^o\ 50'$	1.0	$\frac{i}{5}$
10	1.3	45.0	1.0	1.0	1.0	9i	$\frac{i}{5}$	1.0
11	0.4i	45.0	1.0	1.0	1.0	$31^o\ 50'$	$\frac{i}{5}$	1.0
12	1.3	10+30(i-1)	1.0	1.0	1.0	$31^o\ 50'$	$\frac{i}{5}$	1.0
13	1.3	10+30(i-1)	$\frac{i}{5}$	1.0	1.0	$31^o\ 50'$	1.0	1.0
14	0.4i	45.0	1.0	1.0	$\frac{i}{5}$	$31^o\ 50'$	1.0	1.0
15	0.4i	45.0	$\frac{i}{5}$	1.0	1.0	$31^o\ 50'$	1.0	1.0
16	1.3	45.0	1.0	1.0	1.0	$31^o\ 50'$	$\frac{i}{5}$	$\frac{i}{5}$
17	0.4i	10i	1.0	1.0	1.0	$31^o\ 50'$	1.0	1.0
18	0.4i	45.0	1.0	1.0	1.0	9i	1.0	1.0
19	0.4i	45.0	1.0	1.0	1.0	$31^o\ 50'$	$\frac{i}{5}$	1.0
20	1.3	45.0	1.0	$\frac{i}{5}$	1.0	$31^o\ 50'$	$\frac{i}{5}$	1.0
21	1.3	45.0	1.0	1.0	$\frac{i}{5}$	$31^o\ 50'$	$\frac{i}{5}$	1.0

laboratory investigations. (The laboratory investigation determined values for the apparent quantum yield and the consumption e-folding time with an uncertainty of about 50%; the corresponding optimized values determined from the inverse study have uncertainties of about the same size). The results of this particular inverse study are shown in Figure 5-7 with respect to the absolute value of CO inventory deviation and in Figure 5-8 with respect to the absolute value of sea surface [CO]. Interestingly, both contour plots have valleys indicating that a range of parameter pairs will produce equivalent agreement with the measurements. For the case of CO inventory, the valley extends past an e-folding consumption time of 250 h for a quantum yield factor of 0.5 and past a yield factor of 2.5 for a consumption e-folding time of about 250 h. For sea surface [CO] the range is somewhat more restricted, extending from a quantum yield factor/consumption e-folding time pair of 1.8/45 h to 0.7/120 h. The two sets of values obtained from optimizing these variables with respect to CO inventory and sea surface [CO] are in general agreement, although the inventory study tends predict slightly higher optimized values for the independent variables than the sea surface [CO] study. The results of the minimization of the absolute deviation of modelled and measured times of maximum afternoon sea surface [CO] suggest that e-folding consumption time is optimized at about 45 h.

The inverse study gave a parameter range for the optimal e-folding consumption times and the quantum yield factors. In running the models with these optimized parameters, however, is is apparent that one optimized parameter pair gives better qualitative agreement with the data set than another extreme optimized parameter pair. An example of this is given Figures 5-9 and 5-10 which show a comparison of measured and modelled sea surface [CO] for models run with the quantum yield factor/e-folding consumption time parameter pairs of 1.5/43 h and 0.70/120 h, respectively. While both combinations predict the same mean absolute deviation in sea surface [CO] between modelled and measured values, the trial with the longer e-folding consumption time is not effective at capturing the diurnal range in variation of sea surface [CO]. The best values for the quantum yield factor and the consumption e-folding time would thus appear to be 1.5 and 43 h, respectively.

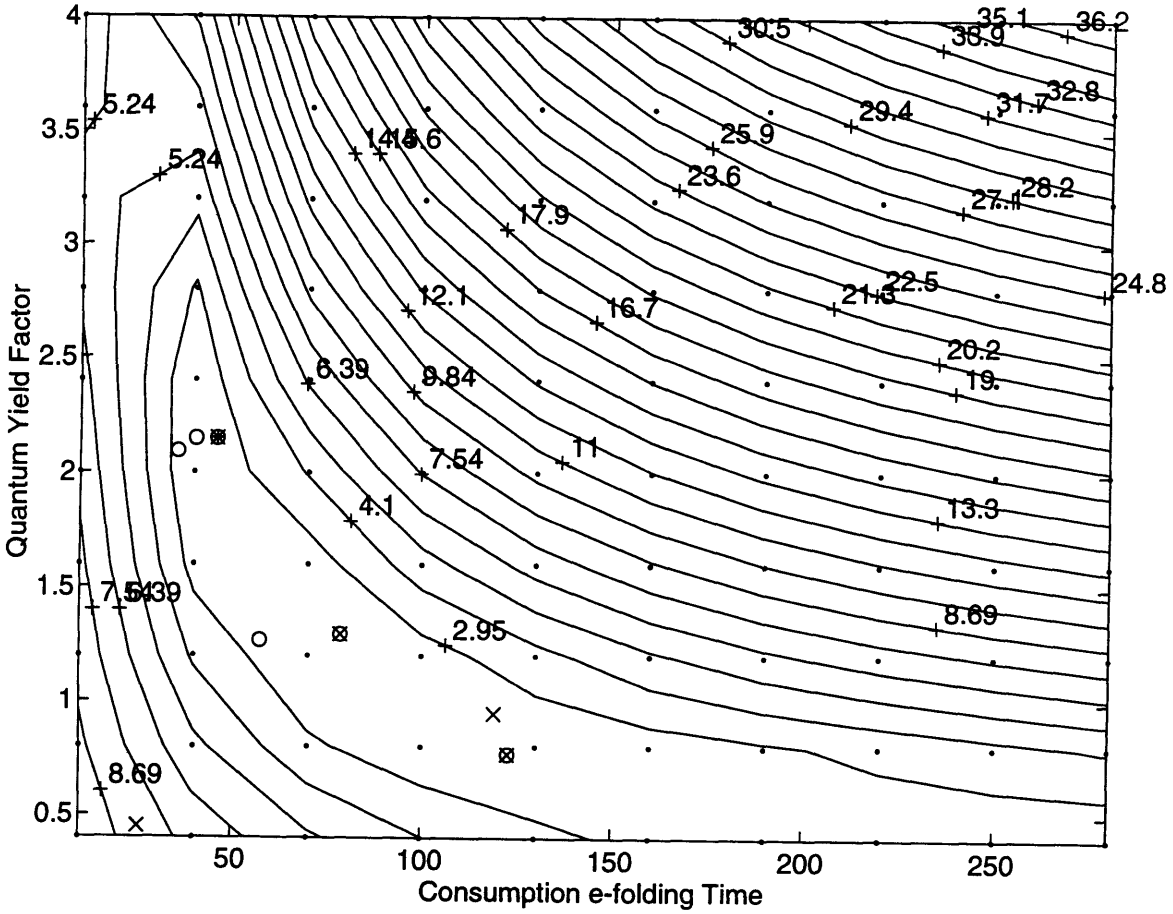

Figure 5-7: Results of inverse model investigation of quantum yield factor versus CO consumption e-folding time with respect to the mean absolute value of deviation between the modelled and measured results for CO inventory (contour units are 10^4nmolm^{-2}). The circles indicate minimum values of the ten rows of model data. The crosses indicate minimum values in the ten columns of data. The star-circle indicates the minimum mean absolute deviation for the plot at a quantum yield factor of 2.2 and a consumption e-folding time of 45.9 h.

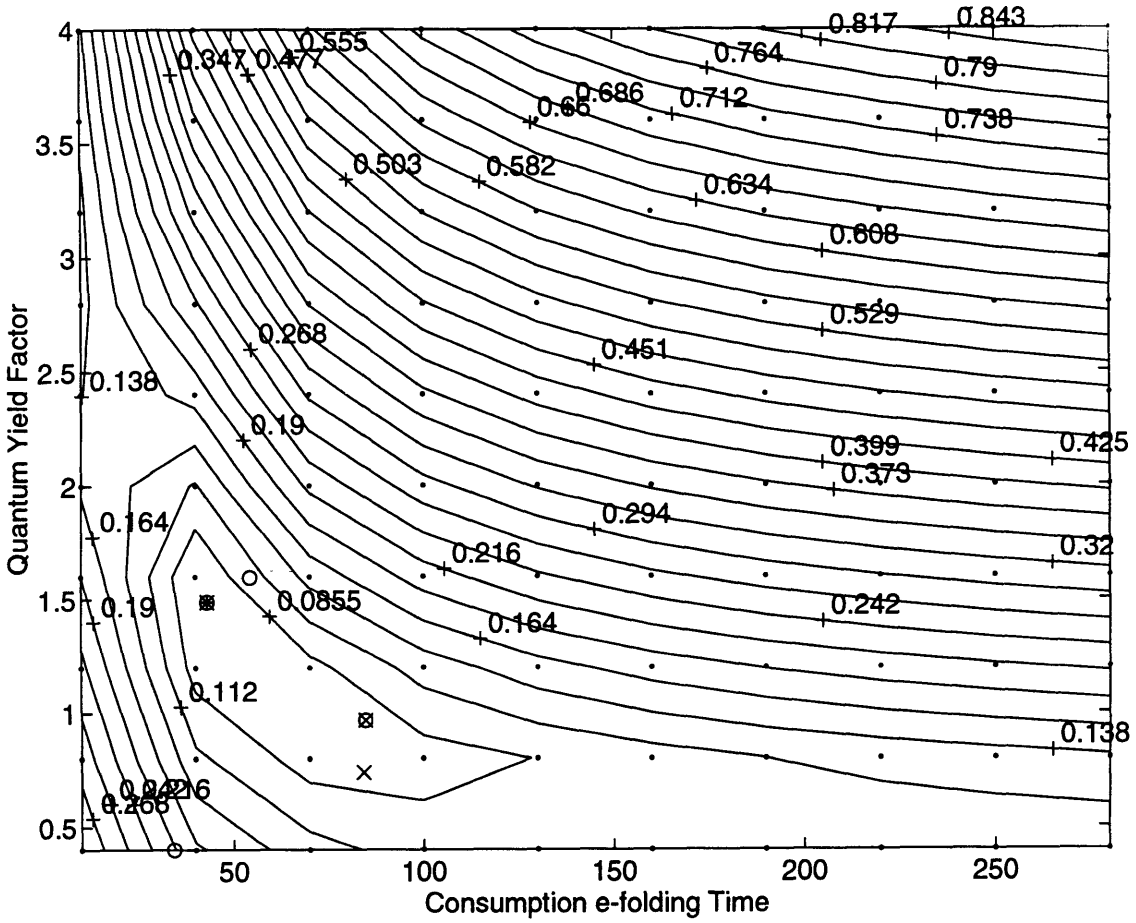

Figure 5-8: Results of inverse model investigation of quantum yield factor versus CO consumption e-folding time with respect to the mean absolute value of deviation between the modelled and measured results for sea surface [CO] (contour units are nM). The circles indicate minimum values of the ten rows of model data. The crosses indicate minimum values in the ten columns of data. The star-circle indicates the minimum mean absolute deviation for the plot at a quantum yield factor of 1.5 and a consumption e-folding time of 43.0 h.

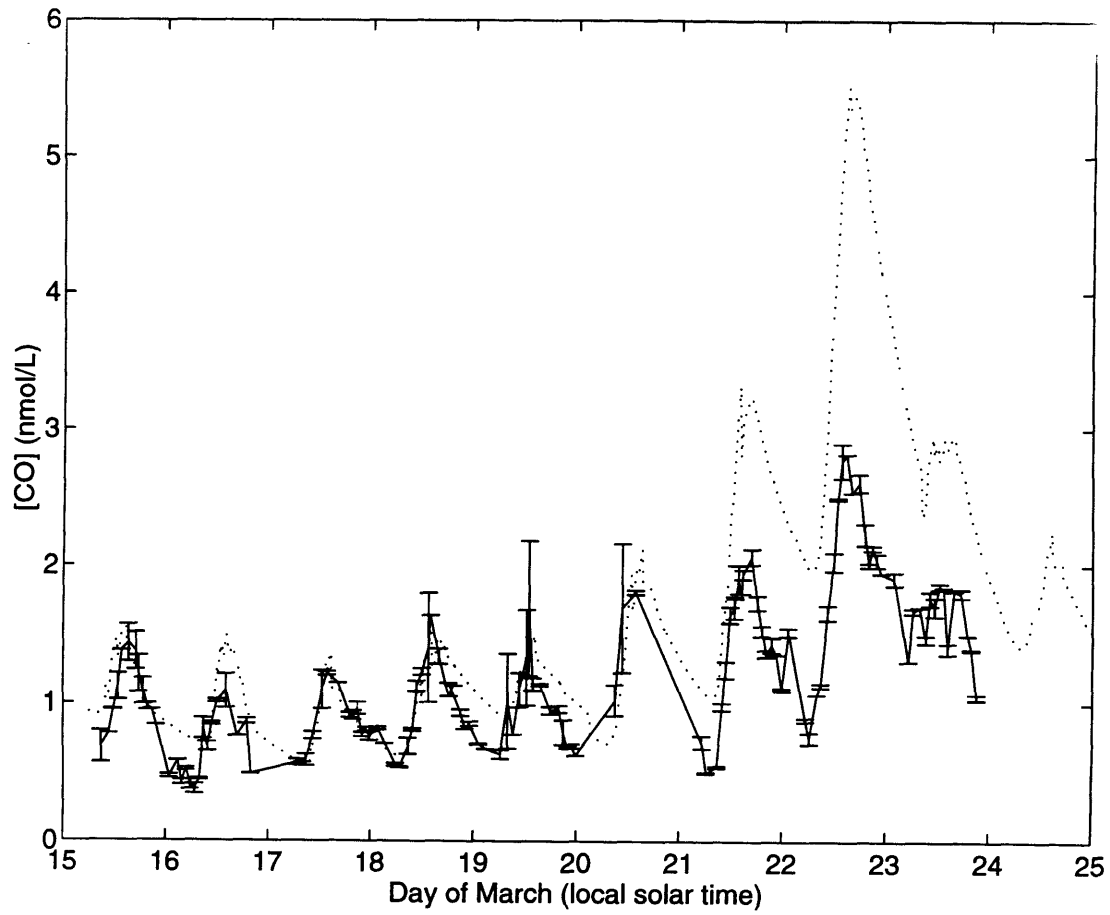

Figure 5-9: Comparison of measured sea surface concentration with those modelled with a quantum yield factor of 1.49 and an e-folding CO consumption time of 43 h. This combination of values results in good agreement between the modelled and measured surface [CO] values for the first part of the investigation. On March 21-23 the model tends to overpredict the actual measured sea surface [CO], suggesting that the surface waters may have experienced some sort of photobleaching effect or else that a property front may have passed through the BATS site on March 21. The results suggest that this water mass might have had a lower CO production capacity or a faster microbial consumption ability.

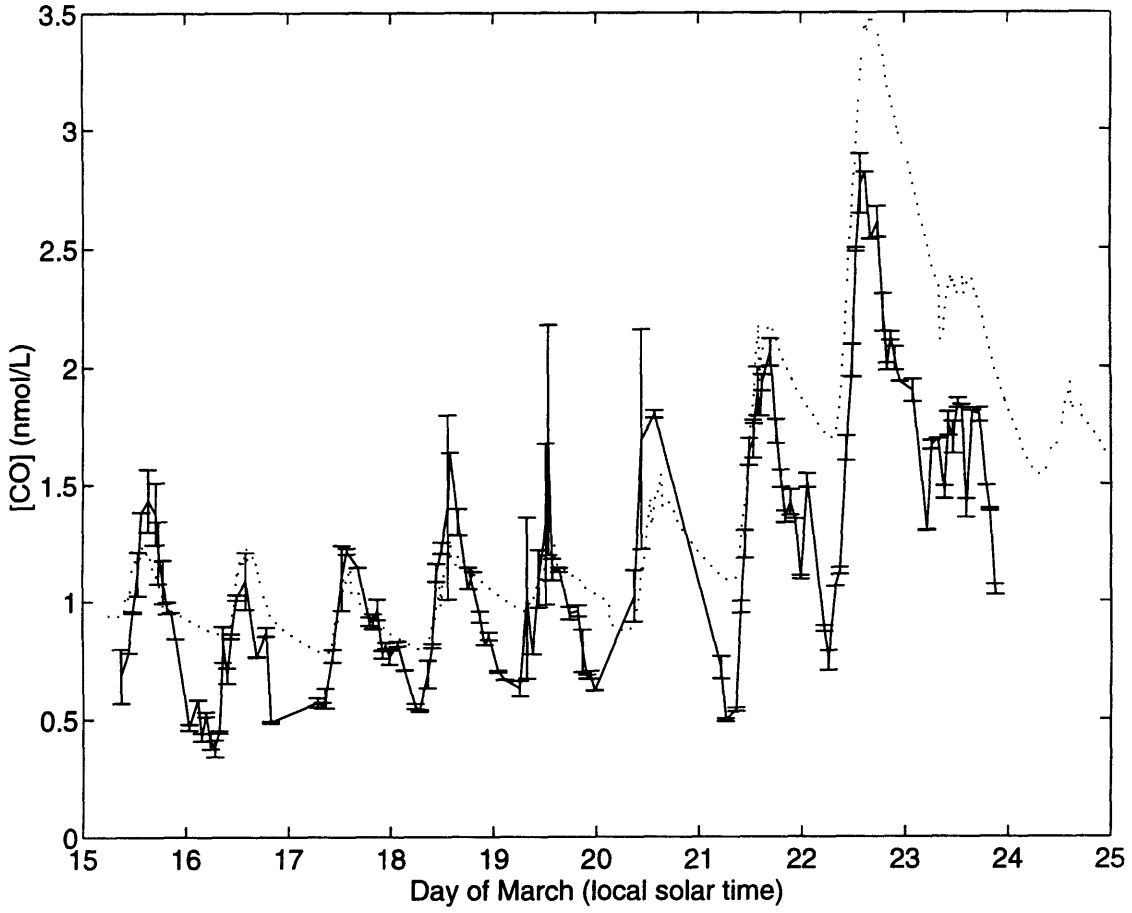

Figure 5-10: Comparison of measured sea surface concentration with those modelled with a quantum yield factor of 0.70 and an e-folding CO consumption time of 120 h. These results have the same mean absolute deviation between the modelled and measured sea surface [CO] as the result given in Figure 5-9. However, the microbial e-folding consumption time in this plot is too long and not adequate to reset sea surface [CO] to its measured values just before dawn.

The trial with the shorter e-folding consumption time produces model results with very good agreement with measurements between March 15–20, inclusive. For March 21–24 this parameter combination produces model results which overpredict the measurement results. These were days of low winds, high insolation, and shallow mixed layer depth. Several combination of factors could have served to decrease the measured sea surface [CO] from its expected modelled value. For instance, the waters may have been photobleached with respect to CDOM by insolation without replenishment by deep mixing. There were thermal fronts passing through the region during the investigation period, and these may have had different production and consumption factors associated with them. This has already been explored with respect to the front which passed through the site on March 21.

The values of the other independent variables could not be optimized using the CO data to levels of accuracy comparable to their direct measurement. This was not surprising as most of the other independent variables were important in determining the depth of the mixed layer and had only an indirect effect in modifying [CO]. Estimates of optimized values of each of the independent parameters have been determined from the 21 inverse model runs and are given in Tables 5.2 to 5.9. It is reassuring that most of these optimized estimates give values which are close to measured values. Piston velocity seems to be the only exception here, and the inverse study tended to return estimates that differed from the Liss and Merlivat (1986) by factors ranging from 0.6 to 11. This is examined below.

In general, the sea surface [CO] studies give optimized values which are closer to the measured values than the CO inventory studies. The one exception to this is the diffuse attenuation coefficient estimate, which appears to be better determined by the CO inventory study.

The results of the sensitivity analysis are also given in these tables. With the exception of latitude, the sensitivity parameters in these tables are all directly comparable on the same scale. The mean absolute deviation for sea surface [CO] and CO inventory (denoted by $\Sigma|x_i(\text{model}) - x_i(\text{measured})|$, where x is sea surface [CO] or CO inventory) exhibited the highest sensitivity to perturbations in the quantum yield

factor and the insolation factor away from their optimized values. The reason for the high sensitivity is because the light-induced production has the greatest influence in the rate of change of [CO] averaged over time compared to microbial consumption, dilution due to mixed layer deepening, and degassing through the surface (which all share in removing CO from the mixed layer). Since quantum yield and insolation both directly determine production rate, these variables should be very sensitive with respect to perturbations in [CO]. It is possible that insolation may have an even greater sensitivity than quantum yield because of its dual role in CO production and diurnal mixed layer formation.

The mean absolute deviation for sea surface [CO] and CO inventory had a slightly lower sensitivity to perturbations in the CO consumption e-folding time away from its optimized value. This is expected because the microbial consumption has the second most important effect in controlling the rate of change of [CO] in the mixed layer.

The sensitivity for piston velocity varied widely from 0.4 to 19 and the values for the parameter also varied widely by a factor of 0.6 to 11 times the Liss and Merlivat (1986) estimate. The large sensitivity and wide range of optimized values associated with the piston velocity seems strange for a variable which is suspected to form a minor sink for CO in the mixed layer. However, the sensitivity result makes sense if one considers the degassing rate is parameterized like the microbial consumption rate in depending on [CO]. It is therefore expected that the piston velocity and the e-folding consumption time should have very similar sensitivity values. If piston velocity was proportional to some fractional power of [CO] then its sensitivity value would be lower than that of microbial consumption. It is also realized that the microbial consumption is a more important factor than degassing in controlling the CO content of the mixed layer. This means that in this inverse study, the e-folding consumption time was more likely to converge to its true value, which minimized the mean absolute deviation for sea surface [CO] and CO inventory. Piston velocity was equally likely to converge to the value which minimized the mean absolute deviation for sea surface [CO] and CO inventory (because of its equivalent sensitivity value), but in this case the optimized value was not necessarily the physically realistic answer. This result

indicates that the optimization routine for piston velocity could easily diverge unless the production and microbial consumption terms are carefully optimized first.

The mean absolute deviation for sea surface [CO] and CO inventory was next most sensitive to perturbations in wind stress and surface heat flux. These two independent variables had approximately equivalent sensitivity effects. These variables are both important in controlling the depth of the mixed layer and hence in determining the rate of change of [CO] due to dilution. Dilution is third in importance in controlling the rate of change of mixed layer [CO], and hence its associated sensitivity value is lower than that for insolation, quantum yield, and microbial consumption rate.

The mean absolute deviation for sea surface [CO] and CO inventory exhibited low sensitivity to perturations in latitude and CDOM absorption. The result for piston velocity was not surprising given that it was fourth in controlling the CO budget in the mixed layer after microbial consumption, light production, and dilution associated with mixed layer deepening.

The result for CDOM absorption (with its attendant influence on diffuse attenuation coefficient) was interesting because it indicated that for most of the investigation ultraviolet (or CO-producing) light attenuation was absorbed at a depth shallower than the mean depth of the mixed layer. Perturbations in the diffuse attenuation coefficient would not have had a major effect because at the end of every time step all the new production would have been spread over the depth of the mixed layer to produce the same mixed layer [CO]. Thus, if the depth of the mixed layer is 50 m, then it does not matter if the mean e-folding depth of production is 5, 10, or even 20 m because at the end of the time step, all the new production will be spread over the 50 m mixing depth. If the mean e-folding depth of CO production was deeper than the depth of the mixed layer, however, then the average amount of CO being produced in the mixed layer would depend critically on its depth. The model results indicate that this was not the case during the investigation period but could have been the case if the water were twice as transparent (a hypothetical, unphysical example). Subsequent studies of the model might include an additional variable where CDOM absorption is fixed and the water absorption is varied or where an additional fixed

absorption is added to simulate the effects of particles and chlorophyll absorption.

The current study was an effective method to estimate the optimized values of the various independent variables based on perturbations of the other independent variables (listed in the left hand column of Tables 5.2 to 5.9). If more computing resources were available, then a more efficient and systematic method of finding a set of optimized values for some of the independent variables could have been used. For a given independent variable, this would have entailed first finding the value that minimized the mean absolute deviation in sea surface [CO] or CO inventory where all the other independent variables were fixed at their best estimates. This procedure would have been repeated for slight perturbations of the other independent variables away from their best estimates (the magnitude of the perturbations falling on a Gaussian of the uncertainty estimate of these other independent variables). After enough iterations, the independent variable of interest could be calculated as the mean of its optimized estimates. This estimate of the optimized value obtained by numerical simulation could be combined with the previously-determined best estimates for the other independent variables to find an optimized estimate for another independent variable by repeating the numerical procedure outlined above. This may be done for each of the remaining variables and then repeated until each of the independent variables settles on a stable value with respect to all the others.

This kind of approach would not be useful for variables that have already been determined very precisely, and hence insolation and latitude would probably be excluded from the analysis to save computational effort. It would also not be useful for variables with a low sensitivity (i.e. diffuse attenuation coefficient) to be included in the analysis because the algorithm would not converge fast enough to be useful or might not even converge on the appropriate value. This elimination leads to 5 independent variables that might be appropriate to optimize: e-folding consumption time, quantum yield, wind stress, net heat flux, and piston velocity. Of these, piston velocity should be optimized at the end of the sequence for the reasons noted above.

Table 5.2: Median of minimum values obtained for apparent quantum yield coefficients in inverse model study with selected other variables. The calculation of the sensitivity parameter is described in the text. The high sensitivity value calculated for the inverse modelling studies using both inventories and sea surface [CO] indicates that model results are sensitive to changes in apparent quantum yield. Also, the apparent quantum yield coefficient is well constrained to a value of about 1.6 or 1.2 according to the inventory of sea surface [CO] studies, respectively.

Other Variable of Inverse Model	Model No.	Φ Coef					
		Inventory			Sea Surface[CO]		
		Value	Uncertainty	Sensitivity	Value	Uncertainty	Sensitivity
τ_c	18	1.56	0.21	7.8	1.14	0.15	7.4
I Coef	16	1.44	0.18	8.1	1.12	0.13	8.6
$\|\tau\|$ Coef	15	1.87	0.25	7.5	1.39	0.17	8.4
ϕ	19	2.15	0.30	7.3	1.43	0.18	8.1
V_P Coef	20	1.87	0.26	7.2	1.33	0.15	9.0

Table 5.3: Median of minimum values obtained for the e-folding CO consumption time in inverse model study with selected other variables. The calculation of the sensitivity parameter is described in the text. The model indicates that the median value for e-folding consumption time is about 70 h for inventory considerations and 50 h for sea surface [CO] considerations. The high relative value of the sensitivity parameter indicates that both inventory and sea surface [CO] are sensitive to changes in e-folding CO consumption time.

Other Variable of Inverse Model	Model No.	τ_c (h)					
		Inventory			Sea Surface[CO]		
		Value	Uncertainty	Sensitivity	Value	Uncertainty	Sensitivity
Φ Coef	18	66	18	3.7	47	32	1.5
$\|\tau\|$ Coef	13	73	10	7.3	51.4	8.9	5.8
V_P Coef	12	73	10	7.3	49.4	7.8	6.3

Table 5.4: Median of minimum values obtained for the insolation coefficient in the inverse model study with selected other variables. The calculation of the sensitivity parameter is described in the text. The model indicates that the median value for the insolation coefficient is about 1.5 for inventory considerations and 1.0 for sea surface [CO] considerations. The high relative value of the sensitivity parameter indicates that both inventory and sea surface [CO] are sensitive to changes in insolation.

Other Variable of Inverse Model	Model No.	I Coef					
		Inventory			Sea Surface[CO]		
		Value	Uncer-tainty	Sensi-tivity	Value	Uncer-tainty	Sensi-tivity
Φ Coef	16	1.46	0.65	2.2	0.99	0.29	3.4
L Coef	6	1.48	0.22	6.7	1.027	0.077	13
ϕ	3	1.74	0.24	7.3	1.026	0.079	13
K_d Coef	5	1.47	0.24	6.1	0.978	0.067	15

Table 5.5: Median of minimum values obtained for the heat loss coefficient in the inverse model study with selected other variables. The calculation of the sensitivity parameter is described in the text. The model indicates that the median value for the heat loss coefficient is about 0.85 for inventory considerations and 1.0 for sea surface [CO] considerations. The moderate relative value of the sensitivity parameter indicates that both inventory and sea surface [CO] are not as sensitive to changes in heat flux as to changes in quantum yield factor.

Other Variable of Inverse Model	Model No.	L Coef					
		Inventory			Sea Surface[CO]		
		Value	Uncer-tainty	Sensi-tivity	Value	Uncer-tainty	Sensi-tivity
I Coef	6	0.91	3.19	0.29	1.6	1.5	1.1
$\lvert\tau\rvert$ Coef	2	0.79	0.42	1.9	0.93	0.86	1.1
V_P Coef	21	0.81	0.45	1.8	0.99	0.13	7.6
K_d Coef	9	0.80	0.44	1.8	1.00	0.12	8.3

Table 5.6: Median of the minimum values obtained for the magnitude of wind stress coefficient in the inverse model study with selected other variables. The calculation of the sensitivity parameter is described in the text. The model indicates that the median value for the wind stress coefficient is about 1.0 for inventory considerations and 1.0 for sea surface [CO] considerations. The moderate relative value of the sensitivity parameter indicates that both inventory and sea surface [CO] are not as sensitive to changes in wind stress as to changes in quantum yield factor.

Other Variable of Inverse Model	Model No.	$\lvert\tau\rvert$ Coef					
		Inventory			Sea Surface[CO]		
		Value	Uncertainty	Sensitivity	Value	Uncertainty	Sensitivity
Φ Coef	15	1.1	4.1	0.27	0.99	0.95	1.0
τ_c	13	2.1	1.7	1.2	2.1	1.1	1.9
L Coef	2	0.86	0.15	5.7	0.86	0.23	3.7
V_P Coef	22	1.05	0.15	7.0	1.01	0.18	5.6
K_d Coef	8	1.06	0.16	6.6	1.03	0.17	6.1

Table 5.7: Median of the minimum values obtained for the latitude in the inverse model study with selected other variables. The calculation of the sensitivity parameter is described in the text. The model indicates that the median value for the latitude is about 25°N for inventory considerations and 37°N for sea surface [CO] considerations. The moderate relative values of the sensitivity parameter indicates that inventory and sea surface [CO] are not as sensitive to changes in latitude compared to quantum yield factor.

Other Variable of Inverse Model	Model No.	$\phi(^o)$					
		Inventory			Sea Surface[CO]		
		Value	Uncertainty	Sensitivity	Value	Uncertainty	Sensitivity
Φ Coef	19	20	48	3.8	36	28	6.4
I Coef	3	26	75	2.4	50	53	3.4
V_P Coef	7	18.8	9.3	19	37	14	13
K_d Coef	10	18.8	7.9	23	37	10	18

Table 5.8: Median of the minimum values obtained for the piston velocity coefficient in the inverse model study with selected other variables. The calculation of the sensitivity parameter is described in the text. The model indicates that the median value for the piston velocity coefficient is about 6 for inventory considerations and very approximately 1 for sea surface [CO] considerations. The variable values of the sensitivity parameter and of the optimized value of piston velocity indicate that sea surface CO and CO inventory are potentially as sensitive to changes in piston velocity as they are to consumption e-folding time. However, piston velocity is a less important parameter than consumption e-folding time in controlling CO inventory and sea surface [CO] and has a greater tendency to diverge unless production and microbial consumption terms are first optimized.

Other Variable of Inverse Model	Model No.	V_P Coef					
		Inventory			Sea Surface[CO]		
		Value	Uncer-tainty	Sensi-tivity	Value	Uncer-tainty	Sensi-tivity
Φ Coef	11	4.68	0.54	8.7	10.1	1.4	7.2
τ_c	4	6.7	5.8	1.2	10.8	6.4	1.7
L Coef	21	8.2	6.4	1.3	1.5	3.7	0.40
$\|\tau\|$ Coef	22	7.1	2.1	3.4	7.4	11.4	0.65
ϕ	7	6.7	0.37	18	0.61	1.10	0.55
K_d Coef	17	7.21	0.37	19	0.73	1.11	0.66

Table 5.9: Median of the minimum values obtained for the diffuse attenuation coefficient factor in the inverse model study with selected other variables. The calculation of the sensitivity parameter is described in the text. The model indicates that the median value for the diffuse attenuation coefficient factor is about 0.95 for inventory considerations and 1.1 for sea surface [CO] considerations. The very low relative values of the sensitivity parameter indicates that both inventory and sea surface [CO] are comparatively insensitive to changes in diffuse attenuation coefficient.

Other Variable of Inverse Model	Model No.	K_d Coef					
		Inventory			Sea Surface[CO]		
		Value	Uncer-tainty	Sensi-tivity	Value	Uncer-tainty	Sensi-tivity
I Coef	5	0.9	11.0	0.082	0.87	8.2	0.11
L Coef	9	1.0	5.9	0.17	1.7	11.6	0.15
$\|\tau\|$ Coef	8	0.99	2.06	0.48	1.2	8.5	0.14
ϕ	10	0.89	2.52	0.35	1.7	7.7	0.22

5.5 Discussion

The modelling study raised some interesting questions that could not be resolved with respect to the experimental results or the published observations. A summary is made of these observations below.

1. There was good agreement between the modelled (baseline model) and measured sea surface [CO] for the period March 15-20 but not between March 21-23 where the modelled values overpredicted the measured ones. The overprediction of sea surface [CO] by the model on March 21, 1993 suggests the possibility that the water in the shallow mixed layer of this period may have been photobleached leading to a lower production coefficient. This possibility has been addressed by Kieber et al (1990) in a laboratory investigation of formaldehyde production in seawater, but has been ignored in the current study where CDOM is assumed constant.

2. There was good agreement between the modelled and measured CO inventory for the period March 15–20, after which measured inventories overpredict modelled values by an amount which can not be reconciled with an increase in insolation between March 21–23. This discrepancy between modelled and measured CO inventories is an interesting problem because it also coincides with a passage of a thermal front through the region. It seems likely that the ocean may be patchy with respect to production and consumption elements and that the thermal front may have also had a different consumption e-folding time or production coefficient.

3. The model taken for the destruction of CO was not optimal in terms of its predictions for [CO] in the deep ocean. On the basis of the laboratory investigation, the data was modelled according to quasi-first order reaction kinetics. While this model was effective for simulations shorter than the e-folding time of microbial consumption, it predicted that CO below the euphotic zone and mixed layer should vanish on longer time scales. This was observed not to be true, and the [CO] in the deep ocean is constant at about 0.25 nM. This may be explained in terms of a blank correction, an absence of CO-consuming bacteria in the deep sea, a small dark production, or a subtlety of microbial metabolism which is not modelled by quasi-first order reac-

tion kinetics or even Michaelis-Menton kinetics. With respect to this last possibility, bacteria may stop consuming CO below a certain threshold [CO].

4. The experimentally determined values for microbial destruction could not be well constrained by the dark incubation studies. The consumption e-folding times were subject to a lot of scatter and the best estimate that could be made for the consumption e-folding time was 52 ± 25 h. The microbes responsible for CO consumption may be destroyed by ultraviolet light near the surface of the water column. However, the precision of the measurement technique was not sufficient to determine the resultant depth dependence of the consumption e-folding time.

5. Published studies by Mopper et al (1991) show a surface CO production (based on irradiation studies in sunlight) which is about two orders of magnitude higher than what has been calculated in this study. The discrepancy has not been resolved, although the light model has been corroborated with LICOR data, and the production values for this study do generate sea surface [CO] which are consistent with measured values.

6. At certain times of day (mostly in the morning and evening) the data shows that the [CO] determined from the surface bucket samples is lower than that of the shallowest Niskin bottle (when the Niskin bottle is within the mixed layer). The result suggests that either degassing is taking place to result in a vertical gradient in [CO] within the mixed layer or else that some systematic bias is being introduced into surface bucket sampling procedure. Future studies might try to resolve which of these possibilities is correct.

Chapter 6

Summary

This investigation considered the production and consumption of CO in the upper ocean. It presents the results of an observational study and a series of laboratory and numerical experiments designed to simulate the chemical processes taking place in the Sargasso Sea during March 15-24, 1993. The results of this investigation and of published studies suggest that the CO budget in the upper ocean is controlled by a light-induced production mechanism, microbial consumption, and outgassing through the sea surface. In addition, wind-induced mixing effects in the upper ocean dilute the [CO] signal by entrainment of CO-depleted water into the base of the mixed layer. The values of these source and sink terms were determined by laboratory experiment and were successfully applied to a numerical simulation of [CO].

With respect to the consumption rate of CO by bacteria, this laboratory investigation centered around a series of dark incubation studies in which unfiltered seawater samples were held in darkness for periods approaching 30 h. Many of the trials were subject to contamination, but once these were identified and eliminated, [CO] depletion in the bottles seemed to follow quasi-first order reaction kinetics and were treated in this fashion for the numerical study. The calculated e-folding consumption times determined by incubation of water from all depths showed considerable scatter. The mean e-folding consumption time for water collected at depths shallower than 75 m was calculated to be 52 ± 25 h.

The production rate coefficient was determined by a series of seawater irradiation

experiments whose aim was to find the apparent quantum yield of the CDOM component of seawater. Water samples from BATS and from near Cape Henlopen were irradiated to find the relative efficiency of CO production at different wavelengths. The determination of quantum yield for the Sargasso Sea sample was complicated considerably by the fact that the CDOM absorption fell below the detection limits of the laboratory spectrophotometer. Nevertheless, the apparent quantum yields that were obtained from the BATS and Cape Henlopen samples are similar to published values.

A numerical model was developed to simulate the [CO] at the sea surface and at depth. This model incorporated production, destruction, and degassing mechanisms with a mixed layer model of the upper ocean to find the time evolution of CO in response to various external forcing factors. The base of the simulation is a model developed by Price et al (1986) with an advanced light model to account for the wavelength dependence of irradiance and CO production. By itself, the light model predicts that the wavelength of maximum surface CO production is approximately 320 nm and that there is virtually no surface production above 400 nm. Also, it predicts that the production is strongly surface trapped with an e-folding depth on the order of about 5 m. Given that the depth of the mixed layer is on the order of tens of metres, this result suggests that the diffuse attenuation coefficient of the water may not be an important factor in the CO budget.

The combined dynamical/chemical model of this investigation showed that the dominant factors controlling sea surface [CO] were the production, microbial consumption, and dilution due to mixed layer deepening. Surface outgassing played a smaller role in the overall budget and amounted to about 20% of the mean production. The model assumed constant values for consumption e-folding time and production coefficient. Using mean values for the last two quantities determined by laboratory experiment, the simulated sea surface [CO] was found to agree closely with measured values of [CO] up to March 21 after which modelled sea surface [CO] tended to overpredict values. The opposite trend was found for CO inventories. Good agreement was found between modelled and measured values up to March 21, and then mod-

elled inventories tended to underpredict measured values by an amount that was not consistent with the calculated increase in insolation on March 21–23, 1993. The underlying cause of this discrepancy is explored in Chapter 5, but seems to be associated with the presence of property fronts in the ocean.

An inverse study was conducted to optimize the independent variables associated with these budget terms by minimizing the mean absolute deviation between modelled and measured sea surface [CO] and CO inventory. These results could constrain the apparent quantum yield and CO consumption e-folding time to values comparable to what was obtained by laboratory experiment. However, the physical variables associated with mixing could not be constrained in the inverse model more accurately than what was obtained by direct measurement. A sensitivity analysis performed in conjunction with the inverse study showed that the quantity $\Sigma|x_i(\text{model}) - x_i(\text{measured})|$ (x is sea surface [CO] or CO inventory) is most sensitive to perturbations in the apparent quantum yield and CO consumption e-folding time away from their optimized values. The mean absolute deviation values were the least sensitive to perturbations in diffuse attenuation coefficient and piston velocity.

Future studies should attempt to address the discrepancies which arose from the modelling study summarized in the Discussion section of Chapter 5. For instance, it is important to know if water that is sequestered in the mixed layer can be photobleached because this would alter its production coefficient. This might give rise to patchiness with respect to production coefficient which was suspected to be responsible for the increased CO inventory starting on March 21. Measurements of the temporal and spatial scales of this patchiness could be accomplished by making a survey of apparent quantum yields over large parts of the ocean at different times. However, fluorescence and absorbance measurements provide a proxy for quantum yield which is much easier and faster to measure with a smaller uncertainty.

The microbial consumption rate might also measured with a lower uncertainty. Current measurements have been fit to quasi-first order decay model whose e-folding decay constant has a high uncertainty with an uncertain depth dependence. It is unclear if the quasi-first order decay model is applicable at high [CO] where bacteria

might be poisoned or at low [CO] where a threshold [CO] may be required to initiate CO consumption. This is important because the current model for CO consumption assumes that all the CO below the euphotic zone should vanish on time scales of about a week. Measurements of [CO] in the deep ocean show that it maintains a constant value of about 0.25 nM, which may be due to a blank correction, to dark production, or to some subtlety in the microbial consumption metabolism. Future studies might try to solve this problem and also assess the effects of exposure of bacteria to ultraviolet light.

The apparent presence of negative vertical gradients in [CO] within the mixed layer indicates either that the assumption of the dynamical model developed by Price et al (1986) that the mixed layer can completely homogenize on a time scale of 15 minutes may be wrong or that there may be a systematic bias in the bucket sampling procedure. The current experimental results do not resolve this question. If they exist, the mixed layer gradients are near the surface where the degassing effects are strongest in morning and evening. Gradients of the opposite sign are present near the surface near midday indicating a strong surface production effect, but these [CO] gradients tend to occur with temperature gradients which indicate shoaling of the mixed layer. Future work should focus on resolving this uncertainty.

The ultimate goal of the project of which this investigation is a part is to be able to estimate the flux of CO from the oceans remotely. Future experimental studies should continue with measurements of CO destruction rate and production coefficient but should also attempt correlate findings with measurements of biological parameters, nutrients, and specifically phytoplankton concentration which can be remotely sensed. If a correlation between these variables exists and if they can be tied to satellite measurements, then it should be possible to estimate the spatial and temporal variability of the CO consumption and production factor over vast tracts of ocean. Estimates of mixed layer depth can already be inferred from remote measurements, and knowing these biogeochemical parameters might enable estimates of CO flux to be made for the world ocean.

Appendix A

List of Variables Used in this Investigation

This appendix lists and defines the variables used in this report.

a	sum of $a_{CDOM}, a_{ph}, a_{SM}, a_w (\mathrm{m}^{-1})$
a_{CDOM}	absorption coefficient of coloured dissolved organic matter (m^{-1})
a_{ph}	absorption coefficient of phytoplankton (m^{-1})
a_{SM}	absorption coefficient of suspended mineral matter (m^{-1})
a_w	absorption coefficient of clearest natural waters (m^{-1})
$\mathrm{A_i}$	empirical constant for determining Bunsen solubility constant as a function of temperature and salinity
$\mathrm{A_{a1}}$	species fit parameter for Rayleigh scatter effects in Green et al (1980) model
$\mathrm{A_{a2}}$	species fit parameter for particulate scatter effects in Green et al (1980) model
$\mathrm{A_{a3}}$	species fit parameter for ozone absorption effects in Green et al (1980) model
$\mathrm{A_{o3}}$	species fit parameter for ozone absorption effects in Green et al (1980) model
$\mathrm{albedo_{diffuse}}$	sea surface albedo for the diffuse, skylight part of irradiance

$\text{albedo}_{\text{Fresnel}}$	sea surface albedo for the specular, solar part of irradiance
b_w	backscatter coefficient for water (m^{-1})
b_{ph}	backscatter coefficient for phytoplankton (m^{-1})
b_{SM}	backscatter coefficient for suspended mineral matter (m^{-1})
B	Bunsen solubility coefficient (mL CO/(atm mL H_2O))
B_i	empirical constant for determining Bunsen solubility constant as a function of temperature and salinity
c	beam attenuation coefficient
C	conductivity (S m^{-1})
C_D	drag coefficient of air
[CO]	concentration of carbon monoxide (mol L^{-1})
$[CO]_{eq.atm}$	concentration of carbon monoxide in water in equilibrium with the concentration of carbon monoxide in air (mol L^{-1})
C_P	heat capacity of seawater (J $kg^{-1}m^{-3}$)
d_1	e-folding depth for longwave component of insolation (m)
d_2	e-folding depth for shortwave component of insolation (m)
D	molecular diffusivity of CO
D	direct solar part spectrum at the earth's surface (W $m^{-2}nm^{-1}$)
$D(\theta, \lambda, o+)$	direct solar part of irradiance just above the sea surface after correction with measured insolation (W $m^{-2}nm^{-1}$)
$D(\theta, \lambda, o-)$	direct solar part of irradiance just below the sea surface after correction with measured insolation (W $m^{-2}nm^{-1}$)
EMP	evaporation minus precipitation (m)
$E(\theta, \lambda, o+)$	spectral irradiance just above the sea surface (W $m^{-2}nm^{-1}$)
$E(\theta, \lambda, o-)$	spectral irradiance just below the sea surface (W $m^{-2}nm^{-1}$)
E_d	downwelling spectral irradiance (W $m^{-2}nm^{-1}$)
E_u	upwelling spectral irradiance (W $m^{-2}nm^{-1}$)
f	coriolis parameter times vertical unit vector (s^{-1})
F	partitioning coefficient between absorption and scattering effects

	in the atmosphere
g	gravitational constant (ms^{-2})
g_0	alpha fit parameter for Green et al (1980) model
G	full solar spectral irradiance at the earth's surface ($Wm^{-2}nm^{-1}$)
h	depth of the mixed layer (m)
H	solar spectral irradiance outside of the earth's atmosphere (W $m^{-2}nm^{-1}$)
I	insolation irradiance (W m^{-2})
I_{space}	solar constant outside the atmosphere (W m^{-2})
I_{theor}	theoretical insolation at the sea surface under clear sky conditions (W m^{-2})
I_1	longwave component of insolation (W m^{-2})
I_2	shortwave component of insolation (W m^{-2})
J_{CO}	net production rate of CO (production minus consumption)
k_0	calibration constant for calculation of k_3 ($(atm\ cm)^{-1}$)
k_3	specific attenuation coefficient of ozone ($(atm\ cm)^{-1}$)
K_d	diffuse attenuation coefficient (m^{-1})
L	surface heat loss (W m^{-2})
m	mixing ratio of CO in air
M	ratio of diffuse skylight irradiance to direct solar irradiance at zero zenith angle
p_a	alpha fit parameter for Green et al (1980) model
P	atmospheric pressure (mbar)
q	mixing ratio of water vapour in air
q_0	alpha fit parameter for Green et al (1980) model
q_a	alpha fit parameter for Green et al (1980) model
Q	net heat flux into the ocean (W m^{-2})
Q	compound undergoing photochemical reaction
r	reference wavelength used in described the variation of CDOM absorbance with wavelength (nm)
R	diffuse reflectance

R_b	bulk Richardson number
R_g	gradient Richardson number
S	salinity (ppt)
S_o	reference salinity for ρ_o (ppt)
S	diffuse (skylight) part of solar spectral irradiance (W $m^{-2}nm^{-1}$)
$S(\theta, \lambda, o+)$	diffuse skylight part of irradiance just above the sea surface after correction with measured insolation (W $m^{-2}nm^{-1}$)
$S(\theta, \lambda, o-)$	diffuse skylight part of irradiance just below the sea surface after correction with measured insolation (W $m^{-2}nm^{-1}$)
S_{CDOM}	slope of the curve describing the linear derease of the natural logarithm of CDOM absorbance with increasing wavelength (nm^{-1})
Sc	ratio of the viscosity of water to the molecular diffusivity of CO
t	time (s)
t_0	alpha fit parameter for Green et al (1980) model
T	temperature ρ_o (°C)
T_o	reference temperature for ρ_o (°C)
U	magnitude of wind speed (m s^{-1})
U_{10}	magnitude of wind speed at 10 m height (m s^{-1})
V_P	piston velocity for CO (m s^{-1})
$\mathbf{V}$	vector velocity in mixed layer (m s^{-1})
w	vertical velocity (m s^{-1})
w_h	vertical velocity at the base of the mixed layer (m s^{-1})
z	depth (m)
α_e	thermal expansion coefficient of water (kg $m^{-3}K^{-1}$)
α_{sky}	transmittance of the atmosphere
β	calibration constant for k_3
β_e	salinity expansion coefficient of seawater (kg $m^{-3}ppt^{-1}$)
γ_1	species fit parameter for Rayleigh scatter effects
γ_2	species fit parameter for particulate scatter effects
γ_3	species fit parameter for ozone absorption effects

δ_3	calibration constant for k_3 (nm)
Δ [CO]	difference in [CO] between mixed layer and layer just below mixed layer (nM)
ΔE_{w+CDOM}	decrease in irradiance between depths z_i and z_{i+1} due to absorption by water and coloured dissolved organic matter (W $m^{-2}nm^{-1}$)
ΔE_{CDOM}	decrease in irradiance between depths z_i and z_{i+1} due to absorption by coloured dissolved organic matter (W $m^{-2}nm^{-1}$)
ϵ	amount of light absorbed by the compound
θ	zenith angle in the atmosphere
θ_w	mean zenith angle in seawater
κ_{CO}	coefficient of eddy diffusion for CO (m^2s^{-1})
λ	wavelength (nm)
λ_o	calibration constant for τ_1
μ	directional cosine of direct sunlight in the atmosphere
μ_1	directional cosine for Rayleigh scatter corrected for earth's curvature
μ_2	directional cosine for particulate scatter corrected for earth's curvature
μ_3	directional cosine for ozone absorption corrected for earth's curvature
μ_4	directional cosine for particulate absorption corrected for earth's curvature
$\bar{\mu}_d$	mean directional cosine for downwelling irradiance
$\bar{\mu}_u$	mean directional cosine for upwelling irradiance
nu	viscosity of water
ν_1	calibration constant for τ_1
ρ	density of seawater as a function of temperature and salinity (kgm^{-3})
ρ_a	density of air (kg m^{-3})
ρ_o	density of seawater at S_o, T_o (kg m^{-3})
$\|\tau\|$	magnitude of wind stress (Pa)
τ_1	optical depth for radiation loss due to Rayleigh scatter

τ_2	optical depth for radiation loss due to particulate scatter
τ_3	optical depth for radiation loss due to ozone absorption
τ_4	optical depth for radiation loss due to particulate absorption
τ_{10}	calibration constant for τ_1
τ_c	e-folding time for microbial destruction of CO (h)
τ_x	east wind stress (Pa)
τ_y	north wind stress (Pa)
ϕ	latitude
ϕ_d	inverse directional cosine funcction for the diffuse component of sunlight
Φ	apparent quantum yield
φ	ratio of diffuse sky irradiance at zenith angle θ to diffuse sky irradiance at zero zenith angle
ω_3	thickness of observed ozone over the equatorial ocean (atm cm)

Appendix B

Data from the Dark Incubation Experiments

The dark incubation experiments were carried out during the first half of the investigation on March 15, 16, 17, and 20. Water for the dark incubation studies was collected in a CTD rosette from different depths down to 200 m.

This appendix presents the processed data from the March 15–24 investigation in the form of plots of the natural logarithm of [CO] (in $nmolL^{-1}$) versus incubation period. The data used to create these plots was processed by Dr. W. Martin and is presented in Table B.1. A total of 23 dark incubation experiments were performed on the cruise; 2 were excluded because there was no initial [CO] measurement and 9 were excluded because of apparent contamination effects during certain incubations. The [CO] have presented in this table have not been corrected for an experimentally determined measurement blank of 0.064 $nmolL^{-1}$ which must be applied to each measurement.

In general, the [CO] for any given depth decreased monotonically with longer incubation periods. However, the data is characterized by a lot of scatter and in some cases the monotonic trend is broken. Where this occurs, it is most probably due to an error in the CO measurement procedure for the specific dark incubation bottle.

Table B.1: Results for the dark incubation experiments conducted during the cruise. Of the original 23 dark incubation experiments conducted, 2 were excluded because there was no initial [CO] value and 9 were excluded because of apparent contamination effects during certain incubations. The [CO] presented in this table have not been corrected for an experimentally determined measurement blank of 0.064 nmolL^{-1}

CTD Station	Day of March	Depth (m)	Data				
2	15	25	Time (min):	0	1380	1700	
			[CO] (nM):	1.09	0.43	0.34	
		150	Time (min):	0	1349	1724	
			[CO] (nM):	0.58	0.26	0.27	
7	16	25	Time (min):	0	872	1196	1811
			[CO] (nM):	1.21	0.79	0.72	0.66
		75	Time (min):	0	854	1203	1798
			[CO] (nM):	0.81	0.61	0.55	0.48
		100	Time (min):	0	848	1227	1806
			[CO] (nM):	0.81	0.51	0.29	0.36
		150	Time (min):	0	832	1240	1790
			[CO] (nM):	0.51	0.33	0.26	0.19
10	17	25	Time (min):	0	540	1045	1388
			[CO] (nM):	1.39	1.17	1.11	0.86
		50	Time (min):	0	566	1034	1500
			[CO] (nM):	0.62	0.53	0.58	0.47
		75	Time (min):	0	586	1028	1423
			[CO] (nM):	0.77	0.75	0.39	0.49
		100	Time (min):	0	583	997	1505
			[CO] (nM):	0.50	0.42	0.46	0.44
		200	Time (min):	0	568	991	1455
			[CO] (nM):	0.33	0.15	0.15	0.20
16	20	10	Time (min):	0	309	519	850
			[CO] (nM):	0.733	0.604	0.602	0.626
		20	Time (min):	0	265	520	810
			[CO] (nM):	0.99	0.887	0.764	0.702
		50	Time (min):	0	251	547	765
			[CO] (nM):	0.82	0.64	0.579	0.617

Appendix C

Data Summary for Irradiation Experiments

Laboratory radiation experiments were carried out ultimately to determine the production of CO in response to sunlight. The more immediate objective of the trials was to assess the apparent quantum yield of the CDOM component of two different seawater samples. The first of these was collected near Cape Henlopen on November 11, 1993 and had a high CO production capacity typical of coastal waters with a high CDOM content. The second was collected from the BATS site on September 24, 1993 and had a low CO production capacity in keeping with its low CDOM absorbance.

The irradiation experiments were divided into two parts. The first of these sought to determine the power output of the Hg-Xe lamp at 12 wavelengths with ferrioxalate actinometry. This technique was based on the photoreduction of $Fe^{3+}_{(aq)}$ on exposure of the solution to a certain amount of photons of a particular wavelength. Longer exposures produce more $Fe^{2+}_{(aq)}$ ions which are measured with a spectrophotometer after complexation with phenanthroline. The amount of Fe^{2+} can be related to the total light energy absorbed by the solution, and the slope of a graph of $[Fe^{2+}]$ versus irradiation period gives a measure of the power entering a solution. In this regard, Figure C-1 presents the actinometry calibration graphs used in this investigation. The power spectrum of the lamp determined by actinometry is given in Figure C-2.

The second part of the experiment involved the actual exposure of seawater solutions to ultraviolet irradiation. This produced CO which was measured using a gas chromatograph. Figure C shows the results for the irradiation of Cape Henlopen water at 12 wavelengths. Figure C-4 shows the results for the irradiation of the BATS seawater sample at 7 wavelengths. In general, the lowest relative uncertainties were associated with the irradiation of the Cape Henlopen water at the shortest wavelengths. This produced a high [CO] which was easily measured. Because of the low CDOM content of BATS water, irradiation of BATS water at longer wavelengths (even for long periods) gave a very small signal which was comparable with the detection limit of the technique. These results have a level of uncertainty which is indicated by the size of the error bars on the plots.

The results of the irradiation data are processed to give apparent quantum yields for BATS and Cape Henlopen water. These are shown in the body of the text but are repeated here in Figure C-5 with error bars along with the data from Valentine and Zepp (1993). The results show fairly good agreement between the two different water samples. They also show that the quantum yields found in this investigation slightly underpredict the published results of Valentine and Zepp (1993) by a factor of 2–3.

Table C.1: Results of actinometry experiments. This table shows the amount of energy absorbed by the actinometry solution in the irradiation tube for various exposure periods and wavelengths.

Wavelength (nm)	Data					
285	Time (min):	3.00	6.00	9.00		
	Energy (J):	0.507	0.884	1.23		
	Δ Energy (J):	0.061	0.084	0.17		
297	Time (min):	2.00	6.00	8.50		
	Energy (J):	0.445	0.82	1.13		
	Δ Energy (J):	0.096	0.33	0.19		
302	Time (min):	2.00	2.00	6.00	9.00	
	Energy (J):	1.031	0.77	1.91	2.78	
	Δ Energy (J):	0.099	0.10	0.19	0.26	
313	Time (min):	2.00	2.00	4.00	6.00	
	Energy (J):	0.708	0.553	1.00	1.47	
	Δ Energy (J):	0.077	0.074	0.12	0.16	
325	Time (min):	3.00	4.00	6.00	9.00	
	Energy (J):	0.250	0.362	0.368	0.498	
	Δ Energy (J):	0.069	0.035	0.064	0.079	
326	Time (min):	3.00	6.00	9.00		
	Energy (J):	0.241	0.385	0.545		
	Δ Energy (J):	0.058	0.032	0.067		
340	Time (min):	3.00	6.00	9.00		
	Energy (J):	0.330	0.546	0.828		
	Δ Energy (J):	0.058	0.096	0.084		
345	Time (min):	3.00	6.00	9.00		
	Energy (J):	0.145	0.223	0.343		
	Δ Energy (J):	0.048	0.050	0.061		
355	Time (min):	3.00	6.00	9.00		
	Energy (J):	0.197	0.318	0.396		
	Δ Energy (J):	0.066	0.093	0.096		
365	Time (min):	0.50	1.00	2.00	4.00	4.00
	Energy (J):	0.334	0.450	0.626	1.186	0.981
	Δ Energy (J):	0.030	0.045	0.042	0.087	0.076
380	Time (min):	3.00	6.00	9.00		
	Energy (J):	0.247	0.411	0.548		
	Δ Energy (J):	0.033	0.052	0.053		
405	Time (min):	2.00	4.00	6.00		
	Energy (J):	0.176	0.303	0.432		
	Δ Energy (J):	0.038	0.056	0.091		

Figure C-1: Data for the ferrioxalate actinometry trials

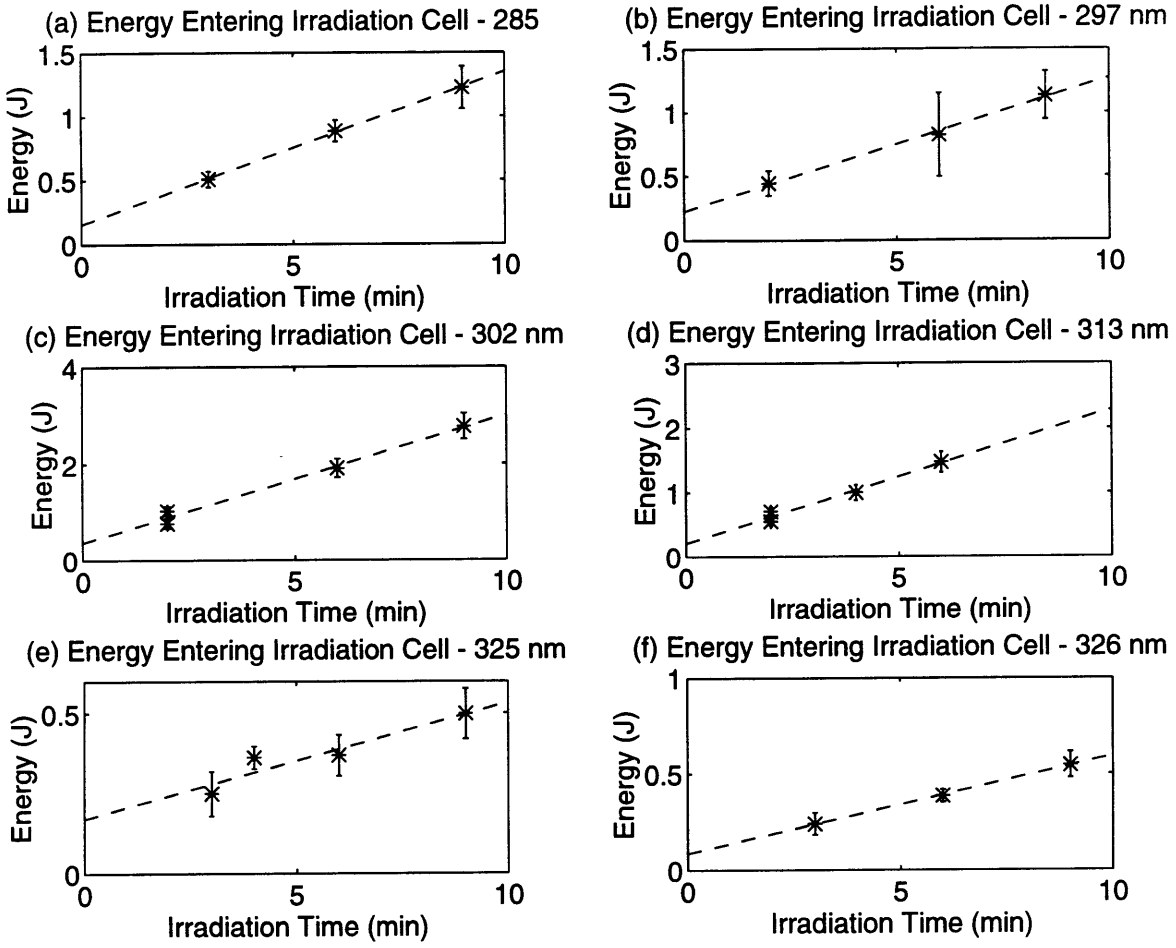

(g) Energy Entering Irradiation Cell - 340 nm

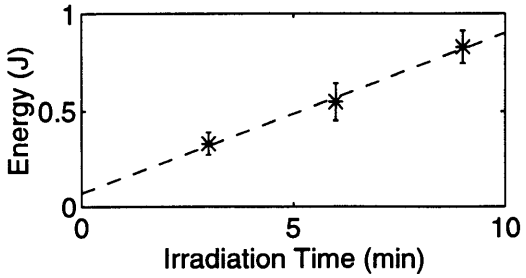

(h) Energy Entering Irradiation Cell - 345 nm

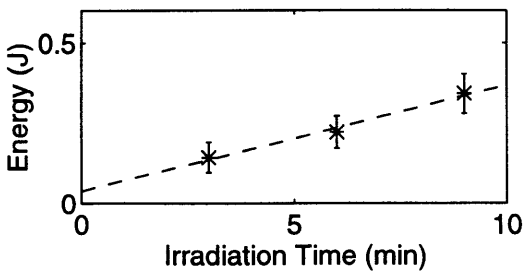

(i) Energy Entering Irradiation Cell - 355 nm

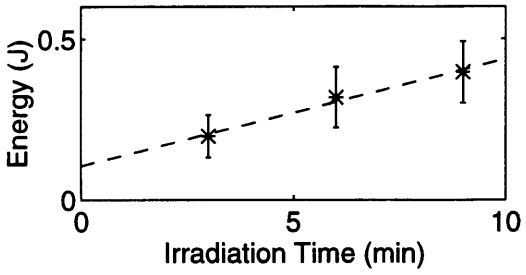

(j) Energy Entering Irradiation Cell - 365 nm

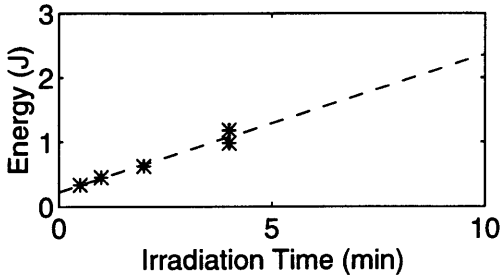

(k) Energy Entering Irradiation Cell - 380 nm

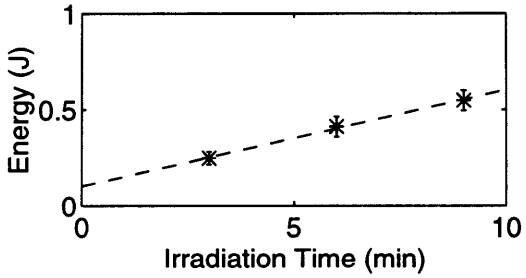

(l) Energy Entering Irradiation Cell - 405 nm

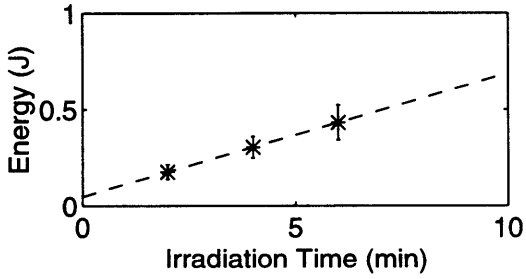

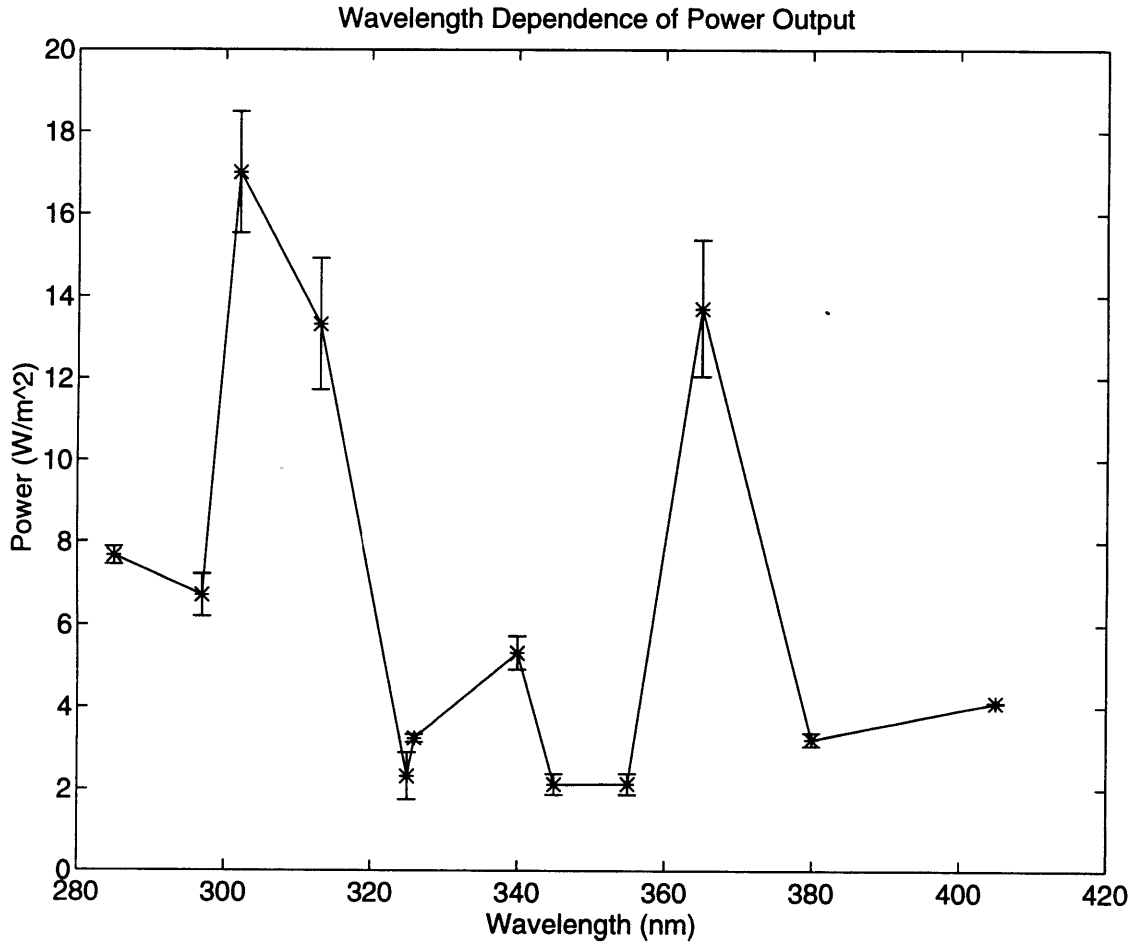

Figure C-2: Power output of the Hg-Xe lamp as determined by actinometry at 12 wavelengths

Table C.2: CO generation data for irradiation experiments of Cape Henlopen water

Wave-length (nm)	Data						
285	Time (min):	2.00	4.00	6.00			
	[CO] (nM):	1.58	2.09	3.17			
	Δ [CO] (nM):	0.35	0.40	0.94			
297	Time (min):	1.00	3.00	5.25			
	[CO] (nM):	0.68	1.84	2.74			
	Δ [CO] (nM):	0.19	0.46	0.67			
302	Time (min):	3.00	6.00	9.00			
	[CO] (nM):	2.21	3.61	5.28			
	Δ [CO] (nM):	0.49	0.73	1.02			
313	Time (min):	1.00	2.00				
	[CO] (nM):	0.45	0.77				
	Δ [CO] (nM):	0.10	0.16				
325	Time (min):	3.00	6.00	9.00			
	[CO] (nM):	0.46	0.55	0.54			
	Δ [CO] (nM):	0.10	0.12	0.12			
326	Time (min):	20.00	40.00	60.00			
	[CO] (nM):	0.65	1.15	2.32			
	Δ [CO] (nM):	0.16	0.24	0.60			
340	Time (min):	3.00	6.00	9.00			
	[CO] (nM):	0.298	0.330	0.44			
	Δ [CO] (nM):	0.078	0.083	0.10			
345	Time (min):	20.00	54.00	85.00			
	[CO] (nM):	0.306	0.52	0.75			
	Δ [CO] (nM):	0.078	0.11	0.15			
355	Time (min):	10.00	30.00	60.00			
	[CO] (nM):	0.44	0.69	0.93			
	Δ [CO] (nM):	0.13	0.17	0.21			
365	Time (min):	1.00	3.00	5.00	10.00	63.58	109.00
	[CO] (nM):	0.246	0.307	0.392	0.293	1.68	2.40
	Δ [CO] (nM):	0.088	0.0.085	0.099	0.078	0.31	0.43
380	Time (min):	60.00	126.00	180.00			
	[CO] (nM):	0.59	0.77	0.89			
	Δ [CO] (nM):	0.18	0.17	0.22			
405	Time (min):	30.00	60.00	120.83			
	[CO] (nM):	0.44	0.56	1.09			
	Δ [CO] (nM):	0.11	0.19	0.23			

Figure C-3: Data for the irradiation of Cape Henlopen water at 12 wavelengths

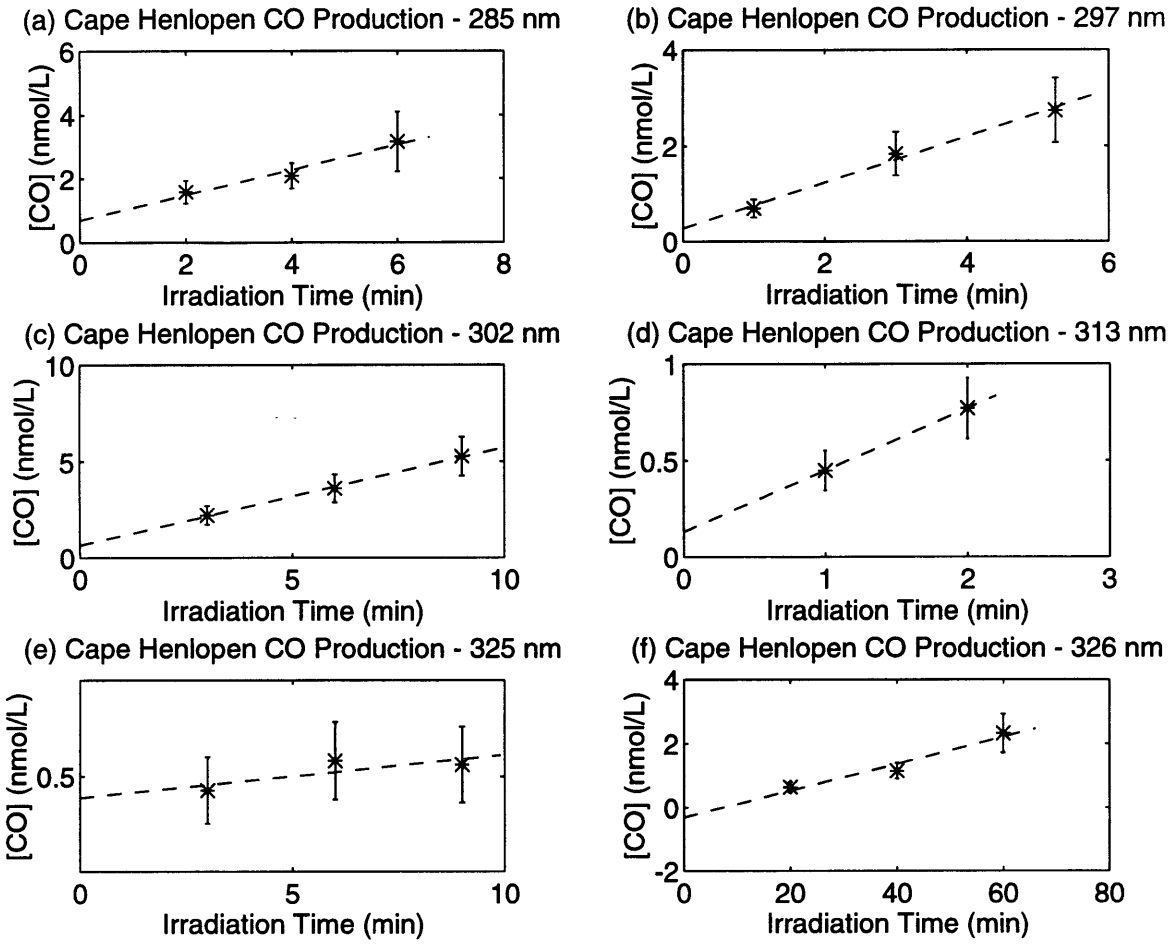

(g) Cape Henlopen CO Production - 340 nm

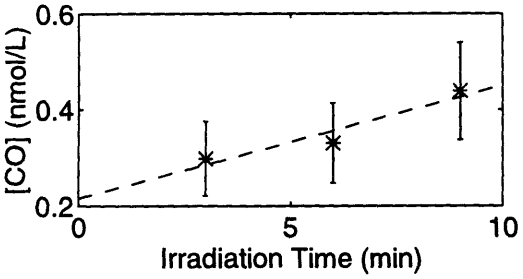

(h) Cape Henlopen CO Production - 345 nm

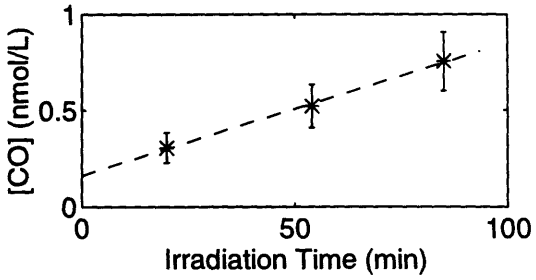

(i) Cape Henlopen CO Production - 355 nm

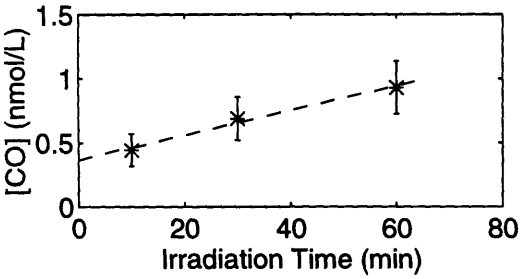

(j) Cape Henlopen CO Production - 365 nm

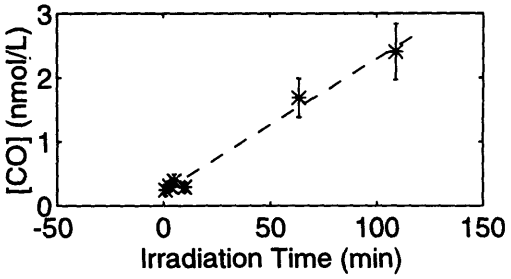

(k) Cape Henlopen CO Production - 380 nm

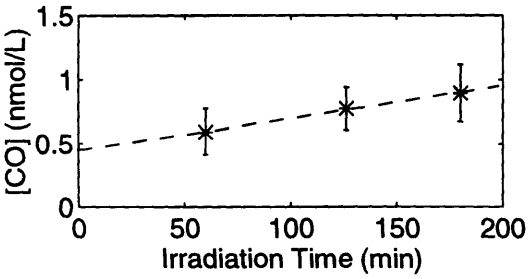

(l) Cape Henlopen CO Production - 405 nm

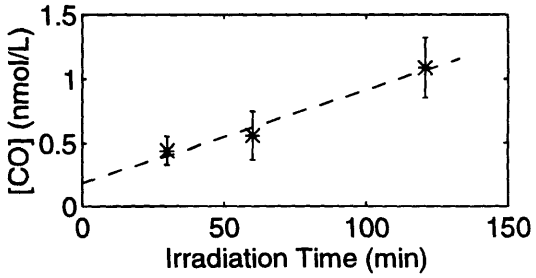

Table C.3: CO generation data for irradiation experiments of Sargasso Sea water

Wavelength (nm)	Data				
297	Time (min):	3.00	5.08	10.00	15.00
	[CO] (nM):	0.30	0.44	0.53	0.83
	Δ [CO] (nM):	0.12	0.13	0.14	0.27
302	Time (min):	5.00	11.00	20.00	
	[CO] (nM):	0.60	0.92	2.05	
	Δ [CO] (nM):	0.16	0.23	0.45	
313	Time (min):	12.00	28.00		
	[CO] (nM):	0.282	1.42		
	Δ [CO] (nM):	0.088	0.30		
326	Time (min):	45.00	125.00	150.00	
	[CO] (nM):	0.29	0.47	0.50	
	Δ [CO] (nM):	0.12	0.12	0.20	
340	Time (min):	84.00	120.00	193.00	
	[CO] (nM):	0.47	0.54	0.60	
	Δ [CO] (nM):	0.17	0.17	0.22	
355	Time (min):	134.00	375.00	499.00	
	[CO] (nM):	0.39	0.34	0.53	
	Δ [CO] (nM):	0.10	0.13	0.13	
365	Time (min):	6.00	10.00	51.00	120.02
	[CO] (nM):	0.145	0.208	2.92	0.323
	Δ [CO] (nM):	0.053	0.064	0.51	0.096

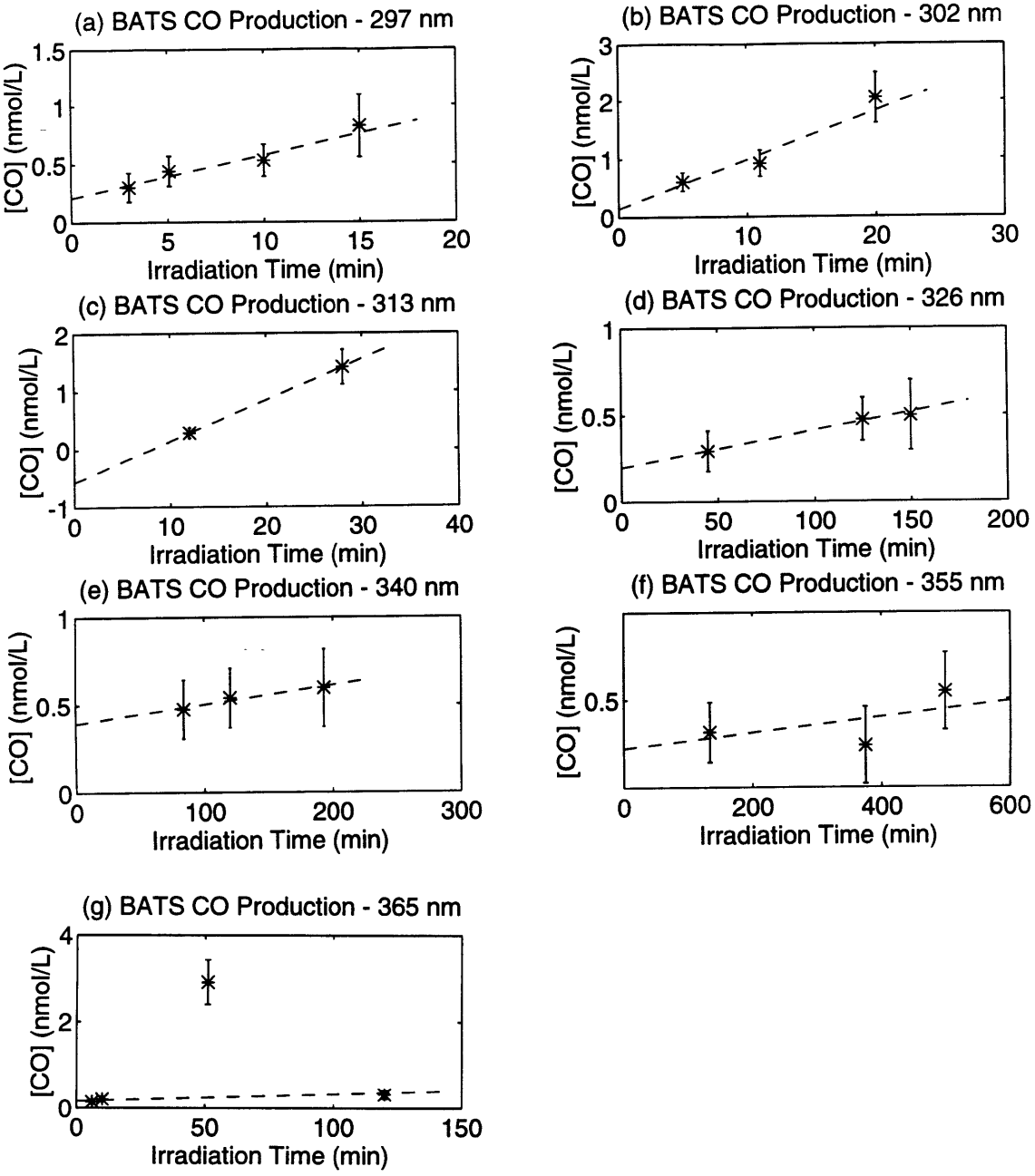

Figure C-4: Data for the irradiation of BATS water at 7 wavelengths

Table C.4: Apparent quantum yield data from the BATS and Cape Henlopen irradiation experiments

Seawater Sample	Wavelength (nm)	Apparent Quantum Yield (mol CO/Einst) ($\times 10^{-5}$)	Error Apparent Quantum Yield (mol CO/Einst) ($\times 10^{-5}$)
Cape Henlopen	285	4.2	1.5
	297	6.3	1.8
	302	2.73	0.68
	313	2.41	0.56
	325	0.67	0.73
	326	1.49	0.55
	340	0.61	0.30
	345	0.48	0.13
	355	0.76	0.26
	365	0.0290	0.0083
	380	0.0187	0.0042
	405	0.061	0.017
BATS seawater; CDOM absorption extrapolated from line of best fit to actual absorption, 280-326 nm	297	5.8	4.0
	302	6.6	3.4
	313	11.7	5.5
	326	2.6	2.8
	340	1.6	4.3
	355	1.9	3.5
	365	2.9	2.2
BATS seawater; calculated using measured CDOM absorption	297	5.6	3.8
	302	6.4	3.3
	313	11.1	5.3
	326	2.2	2.3
	340	1.1	3.0
	355	0.98	1.76
	365	1.12	0.86

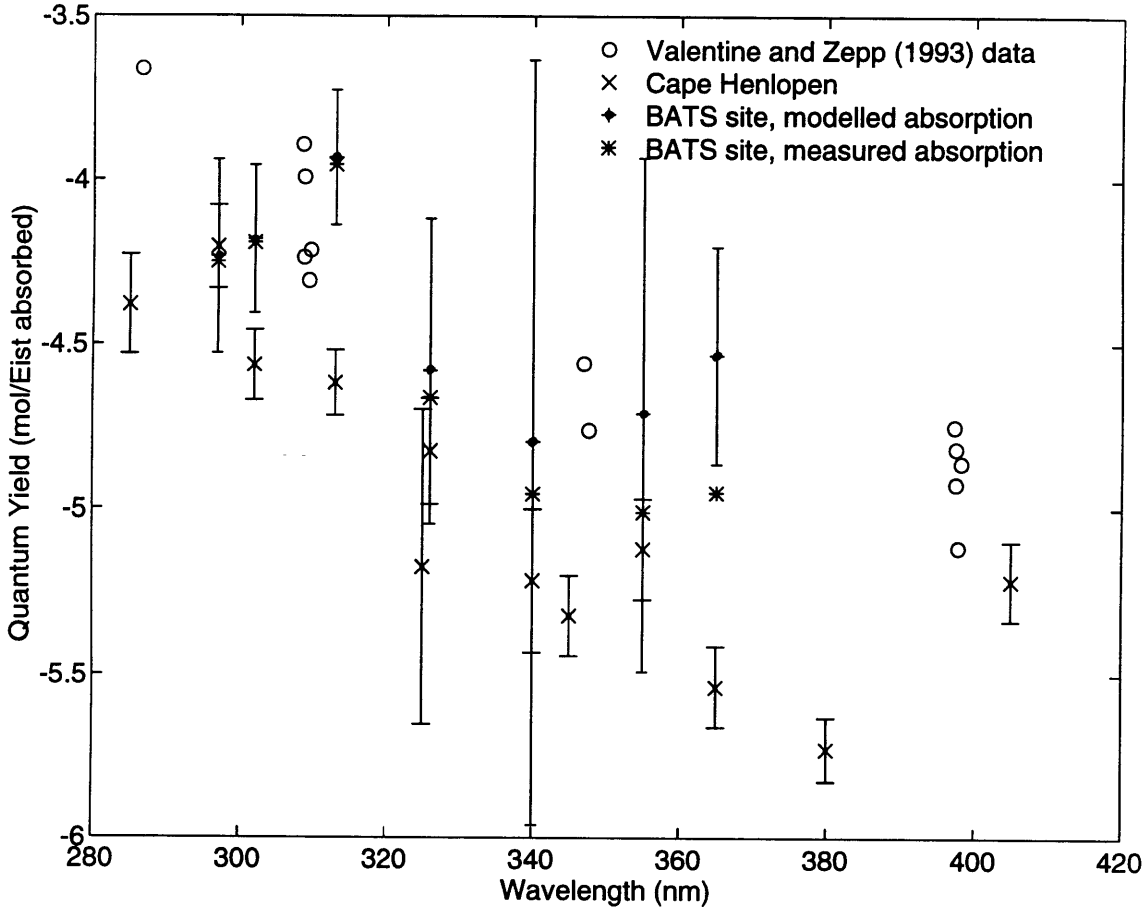

Figure C-5: Apparent quantum yield data with errorbars for BATS and Cape Henlopen water. Valentine and Zepp (1993) data are included for comparison.

Appendix D

Summary of Light Model

This appendix serves to present details of the light model of Green et al (1980) used to deduce sea surface irradiance from from the extraterrestrial light field. The variables are all defined in Appendix A.

Table D.1: Model equations reproduced from Green et al (1980)

$$G(\lambda,\theta) = D(\lambda,\theta) + S(\lambda,\theta)$$
$$D(\lambda,\theta) = \mu H(\lambda) \exp[-\Sigma_j(\tau_j/\mu_j)]$$
$$S(\lambda,\theta) = \varphi(\lambda,\theta) M(\lambda) H(\lambda) \exp[-\Sigma_j(\tau_j)]$$
$$\tau_1 = \tau_{10}(300/\lambda)^{\nu_1}$$
$$\tau_3 = \omega_3 k_3$$
$$k_3 = k_o \frac{(\beta+1)}{(\beta+\exp((\lambda-300)/\delta_3))}$$
$$\tau_4 \approx 0.15\tau_2$$
$$\mu_i = [(\mu^2 + t_i)/(1 + t_i)]^{0.5}$$
$$\mu = \cos(\theta)$$
$$\varphi(\lambda,\theta) = (F + (1-F)\exp[-\gamma_3(\tau_3+\tau_4)\phi])\exp[-(\gamma_1\tau_1 + \gamma_2\tau_2)\phi]$$
$$M(\lambda) = (A_{a1}\tau_1 + A_{a2}\tau_2^{p_a})/[1 + A_{a3}\omega_3(\tau_3+\tau_4)^{q_a}]$$
$$F = [1 + A_{03}(\tau_3 + \tau_4 + g_0 k_3)^{q_0}]^{-1}$$
$$\phi = [(1-t_0)/(\mu^2 + t_0)]^{0.5} - 1$$

Table D.2: GCS fixed parameters

Rayleigh (air) i=1	Particulate i=2	Ozone i=3
$t_1 = 1.8 \times 10^{-3}$	$t_2 = 3.0 \times 10^{-4}$	$t_3 = 7.4 \times 10^{-3}$
$\tau_{10} = 1.22$	$t_4 = t_2$	$K_o = 9.517(\text{atmcm})^{-1}$
$\nu_1 = 4.27$	$\tau_2 = 0.1$	$\beta = 0.0445$
		$\gamma_3 = 7.294\text{nm}$
		$\omega_3 = 0.27$

Table D.3: GCS species fit parameters

Species parameters	Rayleigh i=1	Particulate i=2	Ozone i=3
γ_i	0.5777	0.427	0.977
A_{ai}	0.7879	12.8	0.1978
A_{oi}			3.285

Table D.4: GCS alpha fit parameters

Alpha parameters	α=0	α=a
q_α	1.104	1.079
p_α	-	1.523
g_α	1.433	-
t_α	0.020	

Bibliography

[1] Karen S. Baker, Raymond C. Smith, and A. E. S. Green. Middle ultraviolet radiation reaching the ocean surface. *Photochemistry and Photobiology*, 32:367–374, 1980.

[2] Paula G. Coble, Sarah A. Green, Neil V. Blough, and Robert B. Gagosian. Characterization of dissolved organic matter in the Black Sea by fluorescence spectroscopy. *Nature*, 348:432–435, 1990.

[3] J. B. Colton, D. E. Smith, and J. W. Jossi. Further observations on a thermal front in the Sargasso Sea. *Deep-Sea Research*, 22:433–439, 1975.

[4] R. Conrad, W. Seiler, G. Bunse, and H. Giehl. Carbon monoxide in seawater. *Journal of Geophysical Research*, 87:8839–8852, 1982.

[5] Ralf Conrad and Wolfgang Seiler. Exchange of CO and H_2 between ocean and atmosphere. In P. Buat-Menard, editor, *The Role of Air-Sea Exchange in Geochemical Cycling*, pages 269–282. D. Reidel Publishing Company, 1986.

[6] Peter Cornillon, David Evans, and William Large. Warm outbreaks of the Gulf Stream into the Sargasso Sea. *Journal of Geophysical Research*, 91:6583–6596, 1986.

[7] Dominic M. Di Toro. Optics of turbid estuarine waters; approximations and applications. *Water Research*, 12:1059–1068, 1978.

[8] David J. Erickson III. Ocean to atmosphere carbon monoxide flux: global inventory and climate implications. *Global Biogeochemical Cycles*, 3:305–314, 1989.

[9] Anand Gnanadesikan. Mixed-layer dynamics and the diurnal cycle of carbon monoxide. *unpublished manuscript*, 1990.

[10] Howard R. Gordon, Dennis K. Clark, James W. Brown, Otis B. Brown, Robert H. Evans, and William W. Broenkow. Phytoplankton pigment concentrations in the middle Atlantic Bight: comparison of ship determinations and CZCS estimates. *Applied Optics*, 22:20–36, 1983.

[11] A. E. S. Green, K. R. Cross, and L. A. Smith. Improved analytical characterization of ultraviolet skylight. *Photochemistry and Photobiology*, 31:59–65, 1980.

[12] Sarah A. Green and Neil V. Blough. Optical absorption and fluorescence properties of chromophoric dissolved organic matter in natural waters. *Unpublished manuscript*, 1994.

[13] C. G. Hatchard and C. A. Parker. A sensitive new actinometer. ii. Potassium ferrioxalate as a standard chemical actinometer. *Proceedings of the Royal Society*, 25:518–536, 1956.

[14] Hans-Jorg Isemer and Lutz Hasse. *The Bunker Climate Atlas of the North Atlantic Ocean, volume 1: observations.* Springer-Verlag: Berlin, 1985.

[15] R. D. Jones, R. J. Morita, and R. P. Griffiths. Method for estimating chemolithotrophic ammonium oxidation carbon monoxide oxidation. *Marine Ecology Progress Series*, 17:259–69, 1984.

[16] Ronald D Jones. Carbon monoxide and methane distribution and consumption in the photic zone of the Sargasso Sea. *Deep-Sea Research*, 38:625–635, 1991.

[17] Ronald D. Jones and Jose A. Amador. Methane and carbon monoxide production, oxidation, and turnover times in the Caribbean Sea as influenced by the Orinoco River. *Journal of Geophysical Research*, 98:2353–2359, 1993.

[18] Robert J. Kieber, Xianliang Zhou, and Kenneth Mopper. Formation of carbonyl compounds from UV-induced photodegradation of humic substances if natural

waters: fate of riverine carbon in the sea. *Limnology and Oceanography*, 35:1503–1515, 1990.

[19] K. Ya. Kondratyev. *Radiation in the Atmosphere.* Academic Press: New York, 1969.

[20] R. A. Lamontagne, J. W. Swinnerton, and V. J. Linnenbom. Nonequilibrium of carbon monoxide and methane at the air-sea interface. *Journal of Geophysical Research*, 76:5117–5121, 1971.

[21] W. G. Large and S. Pond. Open ocean momentum flux measurements in moderate and strong winds. *Journal of Physical Oceanography*, 11:324–336, 1981.

[22] W. G. Large and S. Pond. Sensible and latent heat flux measurements over the ocean. *Journal of Physical Oceanography*, 12:464–482, 1982.

[23] Peter S. Liss and Liliane Merlivat. Air-sea gas exchange rates: Introduction and synthesis. In P. Buat-Menard, editor, *The Role of Air-Sea Exchange in Geochemical Cycling*, pages 113–127. D. Reidel Publishing Company: Berlin, 1986.

[24] Robert J. List. *Smithsonian Meteorological Tables.* Smithsonian Institution Press: Washington, D. C., 1984.

[25] Kenneth Mopper, Xianliang Zhou, Robert J. Kieber, David J. Kieber, Richard J. Sikorski, and Ronald D. Jones. Photochemical degradation of dissolved organic carbon and its impact on the oceanic carbon cycle. *Nature*, 353:60–62, 1991.

[26] David L. Musgrave, James Chou, and William J. Jenkins. Application of a model of upper-ocean physics for studying seasonal cycles of oxygen. *Journal of Geophysical Research*, 93:15679–15700, 1988.

[27] P. P. Niiler and E. B. Kraus. One-dimensional models. In E. B. Kraus, editor, *Modeling and prediction of the upper layers of the ocean*, pages 143–172. Pergammon: New York, 1977.

[28] Rudolf W. Preisendorfer and Curtis D. Mobley. Albedos and glitter patterns of a wind-roughened sea surface. *Journal of Physical Oceanography*, 16:1293–1316, 1986.

[29] J. F. Price, C. N. K. Mooers, and J. C. Van Leer. Observations and simulation of storm-induced mixed-layer deepening. *Journal of Physical Oceanography*, 8:582–599, 1978.

[30] J. F. Price, R. A. Weller, and R. Pinkel. Diurnal cycling: observations and models of the upper ocean response to diurnal heating, cooling, and wind mixing. *Journal of Geophysical Research*, 91:8411–8427, 1986.

[31] James F. Price, Robert A. Weller, Clarke M. Bowers, and Melbourne G. Briscoe. Diurnal reponse of sea surface temperature observed at the Long-Term Upper Ocean Study (34°N, 70°W) in the Sargasso Sea. *Journal of Geophysical Research*, 92:14480–14490, 1987.

[32] L. Prieur and S. Sathyendranath. An optical classification of coastal and oceanic waters based on the specific spectral absorption curves of phytoplankton pigments, dissolved organic matter, and other particulate materials. *Limnology and Oceanography*, 26:671–689, 1981.

[33] Ulrich Schmidt. The solubility of carbon monoxide and hydrogen in water and sea-water at partial pressures of about 10^{-5} atmospheres. *Tellus*, 31:68–74, 1979.

[34] Wolfgang Seiler. The cycle of atmospheric CO. *Tellus*, 26:116–135, 1974.

[35] D. A. Siegel and T. D. Dickey. Observations of the vertical structure of diffuse attenuation coefficient spectrum. *Deep-Sea Research*, 34:547–563, 1987.

[36] Richard J. Sikorski and R. G. Zika. Modeling mixed-layer photochemistry of H_2O_2: optical and chemical modeling of production. *Journal of Geophysical Research*, 98:2315–2328, 1993.

[37] Richard J. Sikorski and R. G. Zika. Modelling mixed-layer photochemistry of H_2O_2: physical and chemical modelling of distribution. *Journal of Geophysical Research*, 98:2329–2340, 1993.

[38] R. C. Smith and K. S. Baker. Optical properties of the clearest natural waters. *Applied Optics*, 20:177–184, 1981.

[39] R. C. Smith, J. Marra, M. J. Perry, K. S. Baker, E. Swift, E. Buskey, and D. A. Kiefer. Estimation of a photon budget for the upper ocean in the Sargasso Sea. *Limnology and Oceanography*, 34:1673–1693, 1989.

[40] M. P. Thekaekara. *Solar Electromagnetic Radiation.* NASA SP-8005, 1971.

[41] Richard L. Valentine and Richard G. Zepp. Formation of carbon monoxide from the photodegradation of terrestrial dissolved organic carbon in natural waters. *Environmental Science and Technology*, 27:409–412, 1993.

[42] Anthony Vodacek, Sarah A. Green, and Neil V. Blough. An experimental model of the solar stimulated fluorescence of chromospheric dissolved organic matter. *Limnology and Oceanography, in press*, 1994.

[43] Denis A. Weisenburg and Norman L. Guinasso. Equilibrium solubilities of methane, carbon monoxide, and hydrogen in water and sea water. *Journal of Chemical and Engineering Data*, 24:356–360, 1979.

[44] Robert A. Weller and David S. Hosom. Imet status report. *Unpublished manuscript*, 1992.

[45] Oliver C. Zafiriou, Jacques Joussot-Dubien, Richard G. Zepp Zepp, and Rod G. Zika. Photochemistry of natural waters. *Environmental Science and Technology*, 18:358a–371a, 1984.

[46] Rod G. Zika. Marine organic photochemistry. In E. K. Duursma and R. Dawson, editors, *Marine Organic Chemistry*, pages 299–326. Elsevier: Amsterdam, The Netherlands, 1981.